Electronic Supplementary Information

Polycyclic Aromatic Hydrocarbon Chromophores Tune Photophysical Properties in Bichromophoric Cu(I) Photosensitizers

Oliver Lange[a,†], Florian Doettinger[a,b,†], Johannes P. Zurwellen[a], Lars E. Burmeister[a], Toni M. Maier[c], Christian Kleeberg[d], Christoph R. Jacob[c,*], Michael Karnahl[a], Stefanie Tschierlei[a,*]

[a] TU Braunschweig, Institute of Physical and Theoretical Chemistry, Department of Energy Conversion, Rebenring 31, 38106 Braunschweig, Germany
[b] University of Basel, Department of Chemistry, St. Johanns-Ring 19, CH-4056 Basel, Switzerland
[c] TU Braunschweig, Institute of Physical and Theoretical Chemistry, Gaußstraße 17, 38106 Braunschweig, Germany
[d] TU Braunschweig, Institute of Inorganic and Analytical, Hagenring 30, 38106 Braunschweig, Germany

[†] These authors have contributed equally to this work and share first authorship.

*Correspondence: Prof. Dr. Stefanie Tschierlei: s.tschierlei@tu-bs.de
Prof. Dr. Christoph R. Jacob: c.jacob@tu-braunschweig.de

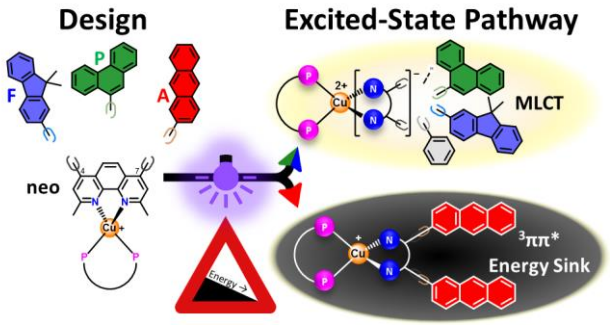

Electronic Supplementary Information - Table of Contents

1 Experimental and Computational Details

1.1 Experimental Details

NMR spectroscopy. Nuclear magnetic resonance (NMR) was conducted by the analytical service of the Institute of Inorganic Chemistry at the Technische Universität Braunschweig using a Bruker Avance IIIHD 500 spectrometer operating at frequencies of 500 MHz (^{1}H), 126 MHz (^{13}C) and 203 MHz (^{31}P) at 298 K. The spectra were processed using the software TopSpin (version 4.2.0). The solvent used for each respective measurement is indicated. All spectra were referenced against the deuterated solvent signal as internal standard. The chemical shifts δ are denoted in ppm relative to the residual solvent signal of the deuterated solvent. NMR multiplicities are noted as: *s* (singlet), *d* (doublet), *t* (triplet), *q* (quartet), *m* (multiplet), *b* (broad). Coupling constants *J* are given in Hz.

Mass spectrometry. Mass spectrometric (MS) measurements were performed by the analytical service of the Institute of Inorganic Chemistry at the Technische Universität Braunschweig. High resolution mass spectra were acquired using electrospray ionization (ESI) on a LTQ-Orbitrap Velos orbitrap mass spectrometer from ThermoFisher Scientific. Samples were dissolved in methanol spiked with 0.1 mg/mL tetradecyltrimethylammonium bromide. Respective ion masses are given as m/z.

X-ray analysis. A single crystal of suitable quality for X-ray crystallography was mounted on a Hampton loop and placed in a cold stream of nitrogen gas on the diffractometer (T = 100 K).[1] The diffraction intensities were collected on a *Rigaku Oxford Diffraction Synergy-S* instrument using mirror-focused CuKα radiation (*Rigaku PhotonJet* microfocus source). The reflections were indexed, integrated and absorption corrections were applied as implemented in the CrysAlisPro software package.[2] The structures were solved employing the program SHELXT and refined anisotropically for all non-hydrogen atoms by full-matrix least squares on all F^2 using SHELXL software.[3] During refinement and analysis of the crystallographic data the programs Mercury, PLATON, DIAMOND and OLEX^2 were used.[4]

Electrochemistry. Cyclic voltammetry was measured in degassed dimethylformamide with 0.1 M Bu_4NPF_6 as the supporting electrolyte. Degassing of dimethylformamide was performed prior to the measurement by sparging with argon for 5 minutes. Measurements were performed on an Autolab potentiostat PGSTAT204 from Metrohm using a three-electrode configuration with a glassy carbon disc with 3 mm diameter stick working electrode, a platinum wire counter electrode, and a non-aqueous Ag/Ag^+ reference electrode (with 0.01 M $AgNO_3$ in acetonitrile). All data are referenced against the ferrocene/ferrocenium (Fc/Fc^+) couple, by adding ferrocene to the solution after each measurement. The scan rate was 100 mV/s unless stated otherwise.

Steady-state UV/vis absorption. Absorption spectra and attenuation coefficients were recorded with a JASCO V-770 spectrophotometer. Spectra were recorded in scan mode with a continuous scan speed of 400 nm/min with a UV/Vis bandwidth of 1 nm and a response time of 0.06 s. Compounds were dissolved in distilled dichloromethane inside a standard 10 mm fluorescence quartz glass cuvette. Attenuation coefficients were recorded under aerated conditions and baseline corrected.

Steady-state emission and emission quantum yield. Emission spectra were recorded with a HORIBA Scientific FluoroMax Plus spectrofluorometer and the software FluorEssence and baseline corrected. Samples were dissolved in dried and distilled spectroscopic grade dichloromethane. The solvent dichloromethane was purified by distillation over CaH_2 under argon atmosphere. The samples were loaded into 10 mm quartz cuvettes under a continuous

argon counterflow (Schlenk line technique). Emission and excitation monochromator bandwidths were set to 1.2 nm for ligand measurements and to 1.8 nm for complex measurements. Integration times were left at 0.1 s with an increment of 1 data point per nm. Optical densities (OD) of the samples were set to around 0.1 at the respective excitation wavelengths of 310 nm for the ligands and 390 nm for the complexes.

Emission quantum yields Φ_S were obtained through

$$\Phi_S = \Phi_{ref} \cdot \left(\frac{OD_{ref}}{OD_S}\right) \cdot \left(\frac{I_S}{I_{ref}}\right) \qquad \text{(eq. 1)}$$

with a known reference emission quantum yield Φ_{ref} (Ligands: pyrene Φ_{ref} = 0.38;[5] Complexes: Cubcp Φ_{ref} = 0.38[6]), the optical density of the sample and reference as well as the integrated luminescence intensity of sample and reference emission. Note that, because all measurements were conducted in dichloromethane, the factor attributed to the refractive index is assumed to cancel out to 1.

Photostability measurements. Photostability measurements were carried out by measuring the steady-state absorption with an AvaLight-DH-S-BAL (Halogen and D_2) light source and a StarLine AvaSpec-ULS2048CL-EVO spectrometer with a 25 µm replaceable slit. The transmission of the inert distilled dichloromethane solutions in 10 mm quartz cuvettes was captured with fiber optic cables (FC-UVIR200-1-ME) and collimating lenses. Solutions were stirred at 600 rotations/minute. Simultaneously, a 150 W Xe arc lamp (LOT-QuantumDesign GmbH) irradiated the sample cuvette with light >280 nm for 2 h and a full spectrum was recorded every 30 s (complexes) or 10 s (ligands). The radiative power arriving at the cuvette amounted to 0.8 W. Blank runs (1 spectrum every 30 s) were conducted at the same conditions without the Xe arc lamp for 1 h.

Time-resolved emission spectroscopy with picosecond resolution. The emission lifetime measurements with picosecond time resolution were carried out with a streak camera system (C10910-01, Hamamatsu Photonics). The samples were excited at 372 nm using a pulsed laser diode with an average pulse width of 42 ps. The repetition rate was set to 10 kHz with an average power of 100 nW. A spectrograph (Kymera 328i-A, Andor) with a holographic grating (50 grooves per mm, blaze 600) was used as a polychromator. The slits in front of the spectrograph and streak camera were opened to 500 µm and 20 µm respectively. All measurements were conducted at room temperature in dry distilled dichloromethane in 10 mm quartz glass cuvettes. The solvent dichloromethane was purified by distillation over CaH_2 under argon atmosphere. The samples were loaded into 10 mm quartz cuvettes under a continuous argon counterflow (Schlenk line technique). The optical density of the samples was set to approximately 0.1 at excitation wavelength and emission was recorded perpendicular to the excitation beam path. All measurements were done in the photon counting mode with an integration time of 30 ms and $1.2 \cdot 10^5$ counts. Time-resolved data was preprocessed with a baseline and time correction.

Transient absorption spectroscopy with nanosecond resolution. Transient absorption (tA) measurements with nanosecond time resolution were conducted using a Q-switched pulsed Nd:YAG laser from Quantel (Q-smart, 450 mJ) with pulse durations of approx. 6 ns at a repetition rate of 10 Hz. Excitation pulses were generated using the Nd:YAG output at 1064 nm. These were sum-frequency tripled to 355 nm using beta barium borate (β-BaB_2O_4, BBO). The excitation light was passed through a laser line filter (CWL = 355 ± 2 nm, FWHM = 10 ± 2 nm) to exclude light of longer wavelength remaining from harmonic generation. The power of the pump beam was about 4 mJ per pulse at the sample. Sample optical densities (OD) were adjusted to

approximately OD=0.3 at the excitation wavelength in inert dichloromethane. The solvent dichloromethane was purified by distillation over CaH_2 under argon atmosphere. The samples were loaded into 10 mm quartz cuvettes under a continuous argon counterflow (Schlenk line technique). Sample stability was tested by comparing the UV/vis absorption of the sample before and after the measurement.

For tA, pump and probe beam were overlapped at the sample site (cross-beam setup). The probe lamp (λ > 360 nm) was operated in flash mode (150 W ozone-free xenon arc lamp, 30 A). For decay kinetics and kinetic maps, the probe light was recorded using a photomultiplier tube from Hamamatsu R928P inside a LP980 spectrometer from Edinburgh Instruments. Transient spectra recorded in kinetic mode were taken with a bandwidth of 1 nm via scanning the transient absorption every 2 nm and taking three averages. Kinetic data was preprocessed with a baseline and time correction. Spectral measurements were conducted with an iCCD camera integrated into the LP980 spectrometer. The time zero was chosen 10 ns after the excitation pulse with a gate width of 3 µs.

1.2 Computational Details

Computational setup and settings. Quantum chemical computations were conducted with the density functional theory implementation in the ORCA suite (version 5.0.3).[7] All computations were performed using PBE0/def2-TZVP and the D3-BJ dispersion correction was included.[8] The convergence threshold of all SCF computations was set to "TightSCF" and the RIJCOSX approximation was used with the def2/J auxiliary basis set to speed up computational times.[9] All computations, unless denoted otherwise, were performed with the conductor-like polarizable continuum model (CPCM) utilizing dichloromethane to account for electrostatic solvent interactions.[10]

Ground-state calculations. Structure optimizations of the electronic ground state were carried out using the same computational setup and subsequent frequency calculations exhibited no imaginary values below -15 cm^{-1} in the molecular Hessian. This can be attributed to numerical noise and the usage of the CPCM model in the frequency computation. Molecular orbitals were computed in a single-point calculation on the ground-state structure.

Excited-state calculations. The first 150 singlet and triplet excitation energies were acquired with time-dependent DFT on the singlet ground state and the lowest triplet-excited state structure, respectively. The Tamm-Dancoff approximation was not applied.[11] The lowest triplet state was optimized with ground-state DFT (ΔSCF) while the lowest excited singlet state was optimized within TDDFT. For singlet optimization the root following feature was kept off (fast) and only turned on for **CunA** (slow). To ensure that the correct singlet state was optimized, the unrelaxed difference density of the chosen state was compared to the optimized state's relaxed difference density. The fluorescence wavelength $\lambda_{fl,calc}$ was defined as the vertical excitation energy from the respective relaxed excited singlet state structure on the electronic ground state. Triplet spin densities were calculated at the same level of theory as all calculations prior through single-point energy calculations on the triplet state with DFT and were used to verify the nature of the triplet state. The phosphorescence wavelength $\lambda_{ph,calc}$ was calculated by calculating the difference in energy of the relaxed triplet T_1 energy and the unrelaxed S_0 energy at the triplet structure. The S_1-T_1 energy gap $\Delta E_{S1\text{-}T1,calc.}$ was calculated by subtracting the final single point energies of the relaxed excited-state structures.

Calculation of Reduction potentials. Redox potentials were computed following the standard protocol.[12] The Born-Haber-cycle shown below (Figure S2.1) was used for the computations of the one-electron redox potentials. Structure optimizations were carried out in vacuum and confirmed to be minima on the potential energy surface by subsequent frequency calculations.

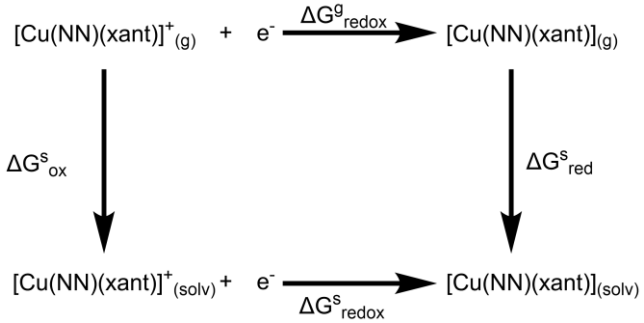

Figure S1.1. Born-Haber Cycle demonstrating the redox couple in vacuum (g) with the free energy difference ΔG^{g}_{redox} at the top and in a solvation model (solv) at the bottom with ΔG^{s}_{redox}. The free Gibbs solvation difference energies ΔG^{s}_{red} and ΔG^{s}_{ox} are a result of the difference of the solvated and vacuum structures.

The Gibbs free energy difference of the solvated redox reaction ΔG^{s}_{redox} can be acquired as

$$\Delta G^{s}_{redox} = \Delta G^{g}_{redox} + \Delta G^{s}_{red} - \Delta G^{s}_{ox} \quad \text{(eq. 2)}$$

The final Gibbs free energy at 298.15 K was used to compute the energy difference ΔG^{g}_{redox} between the oxidized and reduced species. The solvation energies were acquired by single-point energy calculations on the gas phase minimum structure using dimethylformamide in the linked SMD-CPCM implementation to account for non-electrostatic contributions. The solvation energy differences ΔG^{s}_{red} and ΔG^{s}_{ox} were computed as the difference of the final single point energies of the gas phase and solvated structures.

The absolute redox potentials $E°_{redox}(abs)$ of a one-electron process can then be obtained by

$$E°_{redox}(abs) = \Delta G^{s}_{redox} / F \quad \text{(eq. 3)}$$

with F being the Faraday constant. Absolute potentials were referenced against the Fc/Fc^{+} couple calculated at the same level. Moreover, the sign of eq. 3 has to be inverted for the oxidation.

$$E°_{redox}(ref) = E°_{redox}(abs) – E°_{redox,ref}(abs) \quad \text{(eq. 4)}$$

The calculations of doublet spin densities were performed as single-point energy calculations on the vacuum structures with the SMD-CPCM scheme using dimethylformamide as the solvent.

Visualization. Visualizations of the molecular orbitals, spin densities and difference densities were created in ChimeraX[13] with the SEQCROW plugin.[14] The resolution of molecular orbitals and difference density plots were chosen to be 0.15 Å (3.00 Å padding) and 150 (ngrid). Isosurface values were set to ±0.035 for molecular orbitals and ±0.001 for densities. TDDFT singlet excitation spectra were created with the orca_plot program with a FWHM of 3000 cm^{-1} and plotted with R. Triplet excitation spectra were created with a FWHM of 4500 cm^{-1} (except **CunA**: 1500 cm^{-1}).

2 Synthetic Details

Chemicals were acquired from commercial suppliers (*e.g.* Sigma-Aldrich, VWR, Acros Organics or ABCR) and were used as received, if not specified otherwise. Precursors, catalysts, ligands and complexes were synthesized according to the procedures described herein or in the literature cited. Solvents were purified and dried according to standard procedures. Dry dichloromethane, acetonitrile and dry *n*-hexane used for synthesis and spectroscopy were purified by distillation over CaH_2 under argon atmosphere. Oxygen free tetrahydrofuran (THF), *n*-hexane and water were prepared by sparging with argon (2 h for 50 mL while stirring – tetrahydrofuran and *n*-hexane were cooled to 0 °C to minimize evaporation).

Syntheses with oxygen- and/or water-sensitive compounds were carried out in dried glassware and under argon atmosphere. Glassware was vacuum dried while heated with a heat gun at 500 °C for several minutes and flushed with argon three times.

Pyrene used as reference standard for spectroscopy was purified by filtering a concentrated dichloromethane solution through a plug of celite at ambient conditions and evaporating the solvent subsequently. The purified compound was stored under argon.

Synthesis of the ligands nF, nP and nA

nF: 4,7-Bis(9,9-dimethyl-9H-fluoren-2-yl)-2,9-dimethyl-1,10-phenanthroline

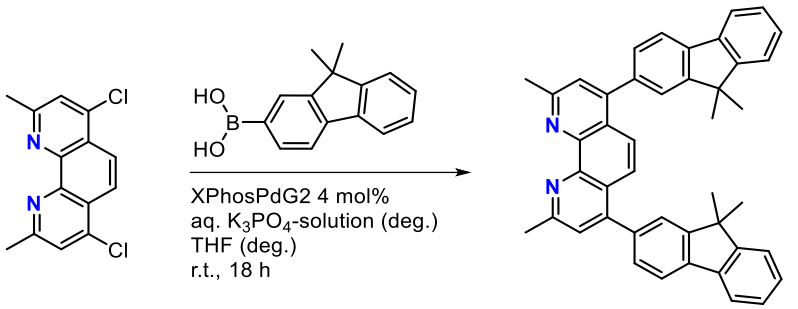

Chemical Formula: $C_{44}H_{36}N_2$
Molecular Weight: 592,79

A 100 ml round-bottom flask was equipped with a magnetic stir bar and charged with XPhos-Pd-G2 precatalyst (0.046 mmol, 35.5 mg, 0.04 eq.), 4,7-dichloro-neocuproine (1.155 mmol, 320 mg, 1 eq.) and 9,9-dimethyl-9*H*-fluoren-2-yl-2-boronic acid (3.464 mmol, 824 mg, 3 eq.). The vessel was attached to a reflux condenser and then evacuated and backfilled with argon three times. Then, degassed tetrahydrofuran (30 mL) was added *via* syringe. Degassed 0.5 M aqueous K_3PO_4 solution (30 mL, freshly prepared) was added *via* syringe and the reaction was stirred at room temperature for 18 hours.

Subsequently, the reaction mixture was diluted with tetrahydrofuran (ambient conditions) and the water phase could be separated. From the organic phase tetrahydrofuran was evaporated and the residue dissolved in chloroform. The organic phase was washed with 1 M NaOH solution, dried with $MgSO_4$ and the solvent removed. The remaining solid was taken up in dichloromethane and purified by column chromatography on basic aluminum oxide with a mixture of dichloromethane+methanol (1 %) as eluent.

The yielded dried crude product was dissolved in acetone, water was added and the mixture boiled for 5 minutes. After cooling to room temperature the mixture was centrifuged and the solution decanted. The remaining oil was taken up in acetone and the solvent evaporated to yield

621 mg (91 %) of the target ligand. The purified product slowly crystallizes to form solid at room temperature.

M = 592.79 g/mol. **^{1}H NMR** ($CDCl_3$, 500 MHz): δ [ppm] = 7.86 (*dd*, *J* = 7.8 Hz, *J* = 0.9 Hz, 2H, ArH), 7.86 (*s*, 2H, ArH), 7.79 (*m*, 2H, ArH), 7.59 (*m*, 2H, ArH), 7.53 (*s*, 2H, ArH), 7.51 (*dd*, *J* = 7.7 Hz, *J* = 1.7, 2H, ArH), 7.47 (*m*, 2H, ArH), 7.37 (*m*, 4H, ArH), 3.03 (*s*, 6H, CH_3), 1.54 (*s*, 12H, CH_3). **^{13}C NMR**: δ [ppm] = 158.78, 153.97, 148.99, 146.18, 139.44, 138.55, 137.19, 128.72, 127.70, 127.16, 124.83, 124.06, 124.00, 123.04, 122.71, 120.27, 119.99, 47.07, 27.16, 26.07. **DEPT NMR**: δ [ppm] = 128.72, 127.70, 127.15, 124.06, 124.00, 123.04, 122.71, 120.27, 119.99, 27.16, 26.07. **HRMS** (ESI) *m/z*: calcd. for $[M+H]^+$: 593.2951, found: 593.2952.

nP: 2,9-Dimethyl-4,7-di(phenanthren-9-yl)-1,10-phenanthroline

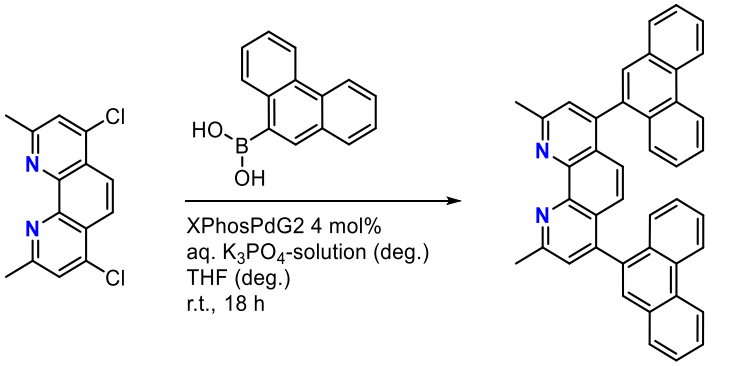

Chemical Formula: $C_{42}H_{28}N_2$
Molecular Weight: 560,70

A 250 ml round-bottom flask was equipped with a magnetic stir bar and charged with XPhos-Pd-G2 precatalyst (0.058 mmol, 44.4 mg, 0.04 eq.), 4,7-dichloro-neocuproine (1.443 mmol, 400 mg, 1 eq.) and 9-phenanthreneboronic acid (4.333 mmol, 961 mg, 3 eq.). The vessel was attached to a reflux condenser and then evacuated and backfilled with argon three times. Then, degassed tetrahydrofuran (40 mL) was added *via* syringe. Degassed 0.5 M aqueous K_3PO_4 solution (40 mL, freshly prepared) was added *via* syringe and the reaction was stirred at room temperature for 18 hours.

Subsequently, the reaction mixture was diluted with tetrahydrofuran (ambient conditions) and the water phase could be separated. From the organic phase tetrahydrofuran was evaporated and the residue dissolved in chloroform. The organic phase was washed with 1 M NaOH solution, dried with $MgSO_4$ and the solvent removed. The remaining solid was taken up in dichloromethane and purified by column chromatography on basic aluminum oxide with a mixture of dichloromethane+methanol(1 %) as eluent.

The yielded dried crude product was dissolved in acetone, water was added and the mixture boiled for 5 minutes. After cooling to room temperature the mixture was centrifuged and the solution decanted. The remaining oil was taken up in acetone and the solvent evaporated to yield 624 mg (77 %) of the target ligand. The purified product slowly crystallizes to form solid at room temperature.

M = 560.70 g/mol. **^{1}H NMR** ($CDCl_3$, 500 MHz): δ [ppm] = 8.74 (*m*, 4H, ArH), 7.86 (*m*, 2H, ArH), 7.76 (*s*, 1H, ArH), 7.73 (*s*, 1H, ArH), 7.69 (*m*, 2H, ArH), 7.62 (*m*, 6H, ArH), 7.39 (*m*, 4H, ArH), 7.18 (*s*, 1H, ArH), 7.15 (*s*, 1H, ArH), 3.08 (*s*, 6H, ArH). **^{13}C NMR**: δ [ppm] = 159.19, 159.07, 147.46, 147.43, 145.78, 145.70, 134.61, 134.55, 131.15, 131.13, 130.98, 130.96, 130.38, 130.37, 130.31, 130.26, 128.76, 128.29, 128.24, 127.17, 127.08, 126.90, 126.88, 126.85, 126.82, 126.35, 126.33, 125.10,

125.03, 123.65, 123.60, 122.93, 122.64, 26.08. **DEPT NMR**: δ [ppm] = 128.76, 128.29, 128.24, 127.17, 127.08, 126.90, 126.88, 126.85, 126.82, 125.10, 125.03, 123.65, 123.60, 122.92, 122.64, 26.08. **HRMS** (ESI) *m/z*: calcd. for $[M+H]^+$: 561.2325, found: 561.2325.

Note: The ^1H and ^{13}C NMR spectra analysis indicated a double set of signals for most of the peaks. Most prominently, two slightly shifted signals appeared for the two methyl groups at position 2 and 9 at the phenanthroline (^1H NMR at 3.08 ppm, *s*, CH_3). This strongly suggests that two different species exist. Details are discussed in the main article.

nA: 4,7-Di(anthracen-2-yl)-2,9-dimethyl-1,10-phenanthroline

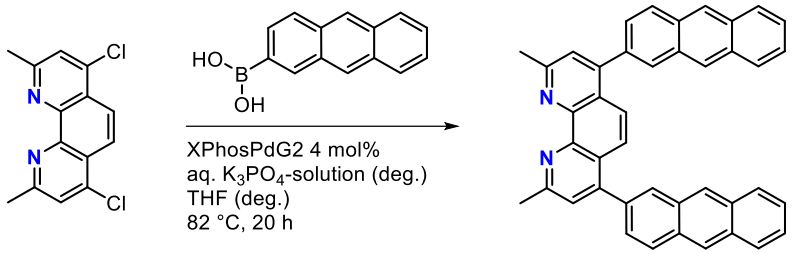

Chemical Formula: $C_{42}H_{28}N_2$
Molecular Weight: 560,70

A 50 ml round-bottom flask was equipped with a magnetic stir bar and charged with XPhos-Pd-G2 precatalyst (0.026 mmol, 20.0 mg, 0.04 eq.), 4,7-dichloro-neocuproine (0.649 mmol, 180.0 mg, 1 eq.) and 2-anthraceneboronic acid (2.598 mmol, 576 mg, 4 eq.). The vessel was attached to a reflux cooler and then evacuated and backfilled with argon three times. Then, degassed tetrahydrofuran (10 mL) was added *via* syringe. Degassed 0.5 M aqueous K_3PO_4 solution (13 mL, freshly prepared) was added *via* syringe and the reaction was stirred at 82 °C for 20 hours (*elevated temperature necessary due to unfavourable solubility of the boronic acid, inhomogeneous orange mixture*).

Subsequently, tetrahydrofuran was evaporated directly from the reaction mixture and the resulting aqueous phase was extracted with dichloromethane several times. The combined organic phase was extracted with 1 M NaOH solution, until the resulting aqueous phase was colourless (*instead of neon-yellow*). The organic phase was dried with $MgSO_4$ and the solvent was evaporated.

The resulting dark red oil (383 mg) was taken up in dichloromethane and purified by column chromatography on basic aluminum oxide (eluent: pure dichloromethane). The first fraction contained anthracene, the second fraction (*yellow*) containing the product was then eluted using a mixture of chloroform + methanol(2 %). The second fraction was collected and dried to yield 290 mg (80 %) of the target ligand. The purified product slowly crystallizes to form a solid at room temperature.

M = 560.70 g/mol. **^{1}H NMR** ($CDCl_3$, 500 MHz): δ [ppm] = 8.52 (*d*, *J* = 3.6 Hz, 4H, ArH), 8.19 (*s*, 2H, ArH), 8.16 (*d*, *J* = 9.0 Hz, 2H, ArH), 8.05 (*m*, 4H, ArH), 7.96 (*s*, 2H, ArH), 7.71 (*s*, 2H, ArH), 7.62 (*dd*, *J* = 8.8 Hz, *J* = 1.8 Hz, 2H, ArH), 7.52 (*m*, 4H, ArH), 3.22 (*s*, 6H, CH_3). **^{13}C NMR**: δ [ppm] = 159.05, 134.19, 132.38, 132.27, 131.11, 130.98, 129.48, 128.84, 128.47, 128.25, 127.04, 126.62, 126.41, 126.06, 125.97, 125.23, 125.16, 123.61, 25.06. **DEPT NMR**: δ [ppm] = 129.28, 128.64, 128.05, 126.84, 126.42, 126.21, 125.86, 125.77, 124.96, 123.41, 24.86. **HRMS** (ESI) *m/z*: calcd. for $[M+H]^+$: 561.2325, found: 561.2325.

Syntheses of the complexes CunF, CunP and CunA

The syntheses of all complexes followed the same general procedure. The exact amounts used for synthesis are noted below.

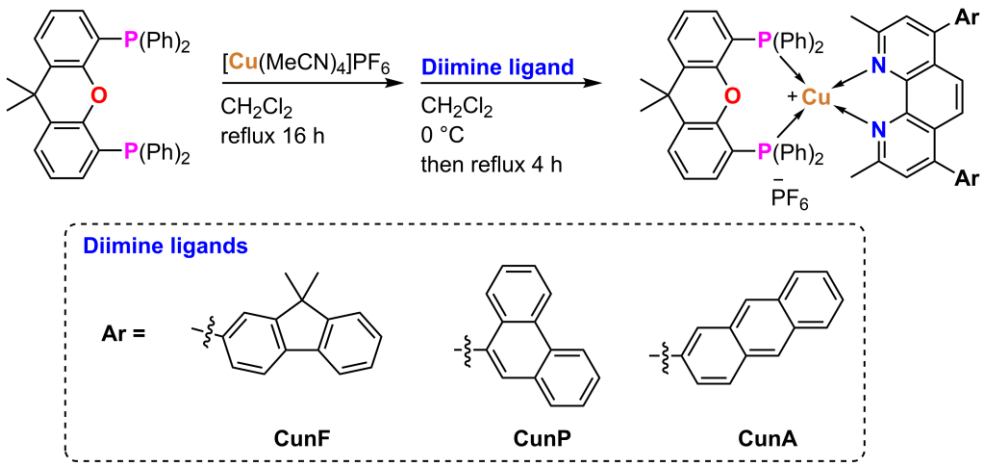

General Procedure:

Into an oven-dried schlenk-tube equipped with a stir bar were added $[Cu(CH_3CN)_4]PF_6$ (1.0 eq.) and xantphos ligand (1.0 eq.). The vessel was attached to a reflux condenser and the apparatus was put under vacuum and refilled with argon three times. Dry and degassed dichloromethane was added and the solution was refluxed for 16 hours.

The solution was cooled to 0 °C and a solution of the respective diimine ligand (**nF**, **nP** or **nA**) in dry and degassed dichloromethane was carefully added dropwise over 60-90 minutes. After an additional 60 min of stirring at 0 °C, the solution was refluxed for four hours and then allowed to cooled to room temperature.

The clear solution was treated with excess amounts of *n*-hexane (aerated conditions) while stirring vigorously. Instead of a crystalline solid, a turbid solution formed. The solution was cleared by filtering through celite. Additional *n*-hexane was added while stirring to again form a turbid solution and yield the final crude product complex as a red sticky oil after 1 hour of continued stirring. After letting the mixture stand for 1 hour, the slightly yellow solution was decanted and the remaining oil was treated with *n*-hexane and twice with diethyl ether (solutions were decanted off). The remaining oil was dried to afford the target complex as solid. The solid was further dried at 35 °C in high vacuum.

CunF: [Cu(**nF**)(xant)]PF_6

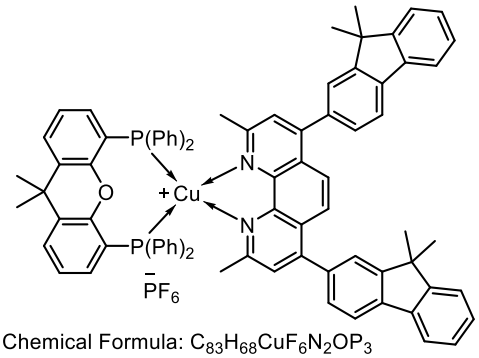

Chemical Formula: $C_{83}H_{68}CuF_6N_2OP_3$
Molecular Weight: 1379.9277

$[Cu(MeCN)_4]PF_6$	xantphos	diimine ligand	dichloromethane	**Yield**
67.1 mg (0.180 mmol)	104.2 mg (0.180 mmol)	101.4 mg (0.180 mmol)	20 mL + 20 mL	165 mg (66 %)

M = 1379.93 g/mol. **^{1}H NMR** (CD_3CN, 500 MHz): δ [ppm] = 7.96 (*d*, 2H, ArH, *J* = 7.5 Hz), 7.88 (*m*, 2H, ArH), 7.84 (*s*, 2H, ArH), 7.77 (*dd*, 2H, ArH, *J* = 7.6 Hz, *J* = 1.5 Hz), 7.67 (*d*, *J* = 1.0 Hz, 2H, ArH), 7.59 (*s*, 2H, ArH), 7.56 (*m*, 2H, ArH), 7.52 (*dd*, *J* = 7.9 Hz, *J* = 1.8 Hz, 2H, ArH), 7.40 (*m*, 4H, ArH), 7.30 (*t*, *J* = 7.3 Hz, 4H, ArH), 7.27 (*t*, *J* = 7.9 Hz, 2H, ArH), 7.17 (*m*, 8H, ArH), 7.11 (*t*, *J* = 7.6 Hz, 8H, ArH), 7.05 (*m*, 2H, ArH), 2.34 (*s*, 6H, CH_3), 1.74 (*s*, 6H, CH_3), 1.53 (*s*, 12H, CH_3). **^{13}C NMR**: δ [ppm] = 159.08, 155.96, 155.46, 155.15, 151.13, 144.69, 141.10, 139.10, 136.68, 135.01, 134.04, 132.64, 131.27, 131.05, 129.95, 129.65, 129.23, 128.97, 128.41, 126.63, 126.43, 125.24, 124.43, 123.93, 122.73, 121.66, 121.40, 48.01, 37.04, 28.92, 27.94, 27.30. **DEPT NMR**: δ [ppm] = 134.04, 131.27, 131.04, 129.95, 129.65, 129.23, 128.95, 128.41, 126.62, 126.42, 125.22, 124.41, 123.93, 121.63, 121.40, 28.92, 27.94, 27.30. **^{31}P NMR**: δ [ppm] = -13.05 (*s*, Ar_2P), -144.61 (septett, PF_6). **HRMS** (ESI) *m/z*: calcd. for $[M\text{-}PF_6]^+$: 1233.4097, found: 1233.4115.

CunP: [Cu(**nP**)(xant)]PF_6

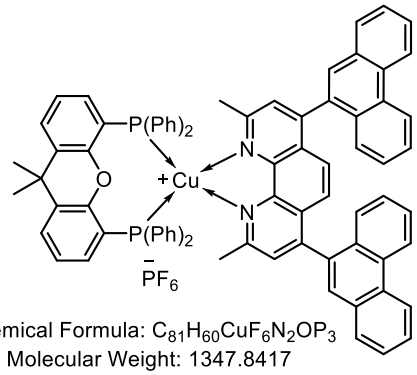

Chemical Formula: $C_{81}H_{60}CuF_6N_2OP_3$
Molecular Weight: 1347.8417

$[Cu(MeCN)_4]PF_6$	xantphos	diimine ligand	dichloromethane	**Yield**
67.1 mg (0.180 mmol)	104.2 mg (0.180 mmol)	95.8 mg (0.180 mmol)	20 mL + 20 mL	142 mg (59 %)

M = 1347.84 g/mol. **^{1}H NMR** (CD_3CN, 500 MHz): δ [ppm] = 8.81 (*m*, 4H, ArH), 7.95 (*m*, 2H, ArH), 7.79 (*m*, 2H, ArH), 7.74 (*m*, 4H, ArH), 7.67 (*m*, 6H, ArH), 7.50 (*m*, 2H, ArH), 7.29 (*m*, 24H, ArH), 7.08 (*m*, 4H, ArH), 2.40 (*s*, 6H, CH_3), 1.74 (*s*, 6H, CH_3). **^{13}C NMR**: δ [ppm] = 159.71, 156.05, 149.80, 144.33, 135.05, 134.55, 134.29, 134.20, 134.18, 134.09, 134.04, 133.84, 132.96, 132.83, 132.77, 132.72, 132.65, 132.60, 132.52, 132.01, 131.34, 131.26, 131.20, 131.03, 130.89, 129.96, 129.78, 129.55, 129.01, 128.96, 128.83, 128.53, 128.32, 128.16, 128.08, 127.88, 127.43, 126.49, 124.81, 124.40, 123.87, 122.78, 37.05, 28.87, 27.95. **DEPT NMR**: δ [ppm] = 134.60, 134.54, 134.48, 134.28, 134.24, 134.19, 134.17, 134.13, 134.08, 133.89, 133.83, 133.77, 131.32, 131.25, 131.18, 131.02, 130.88, 129.95, 129.78, 129.54, 128.95, 128.81, 128.52, 128.31, 128.22, 128.06, 127.88, 127.42, 126.47, 124.80, 124.38, 123.86, 28.87, 27.95, 27.94. **^{31}P NMR**: δ [ppm] = -12.69 (*s*, Ar_2P), -144.62 (septett, PF_6). **HRMS** (ESI) *m/z*: calcd. for $[M\text{-}PF_6]^+$: 1201.3471, found: 1201.3485.

CunA: [Cu(**nA**)(xant)]PF_6

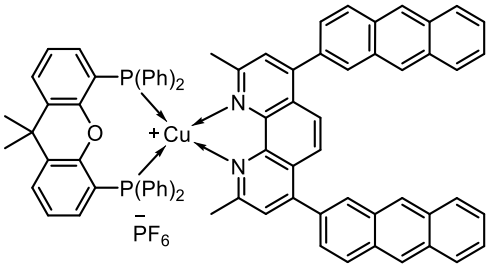

Chemical Formula: $C_{81}H_{60}CuF_6N_2OP_3$
Molecular Weight: 1347.8417

$[Cu(MeCN)_4]PF_6$	xantphos	diimine ligand	dichloromethane	**Yield**
55.9 mg (0.150 mmol)	86.8 mg (0.150 mmol)	84.0 mg (0.150 mmol)	20 mL + 20 mL	101 mg (50 %)

M = 1347.84 g/mol. **^{1}H NMR** (CD_2Cl_2, 500 MHz): δ [ppm] = 8.57 (*s*, 4H, ArH), 8.22 (*d*, *J* = 8.9 Hz, 2H, ArH), 8.16 (*d*, *J* = 1.5 Hz, 2H, ArH), 8.08 (m, 4H, ArH), 7.93 (*s*, 2H, ArH), 7.71 (*dd*, *J* = 7.8 Hz, *J* = 1.7 Hz, 2H, ArH), 7.62 (*s*, 2H, ArH), 7.58 (*dd*, *J* = 8.8 Hz, *J* = 1.8 Hz, 2H, ArH), 7.55 (*m*, 4H, ArH), 7.32 (*t*, *J* = 7.3 Hz, 4H, ArH), 7.25 (*t*, *J* = 7.8 Hz, 2H, ArH), 7.14 (*m*, 16 H, ArH), 7.03 (*m*, 2H, ArH), 2.40 (*s*, 6H, CH_3), 1.77 (*s*, 6H, CH_3). **^{13}C NMR**: δ [ppm] = 158.42, 155.45, 150.53, 144.22, 134.27, 133.88, 133.50, 132.90, 132.74, 131.98, 131.43, 131.39, 130.78, 130.36, 129.90, 129.46, 128.99, 128.61, 128.50, 128.06, 127.42, 126.85, 126.66, 126.58, 126.26, 125.99, 125.69, 124.14, 121.93, 36.50, 28.79, 27.79. **DEPT NMR**: δ [ppm] = 133.30, 130.58, 130.15, 129.70, 129.26, 128.79, 128.40, 128.31, 127.86, 127.22, 126.65, 126.46, 126.38, 125.79, 125.49, 123.94, 28.65, 27.59. **^{31}P NMR**: δ [ppm] = -12.60 (*s*, Ar_2P), -144.65 (septett, PF_6). **HRMS** (ESI) *m/z*: calcd. for $[M\text{-}PF_6]^+$: 1201.3471, found: 1201.3479

3 NMR Spectra

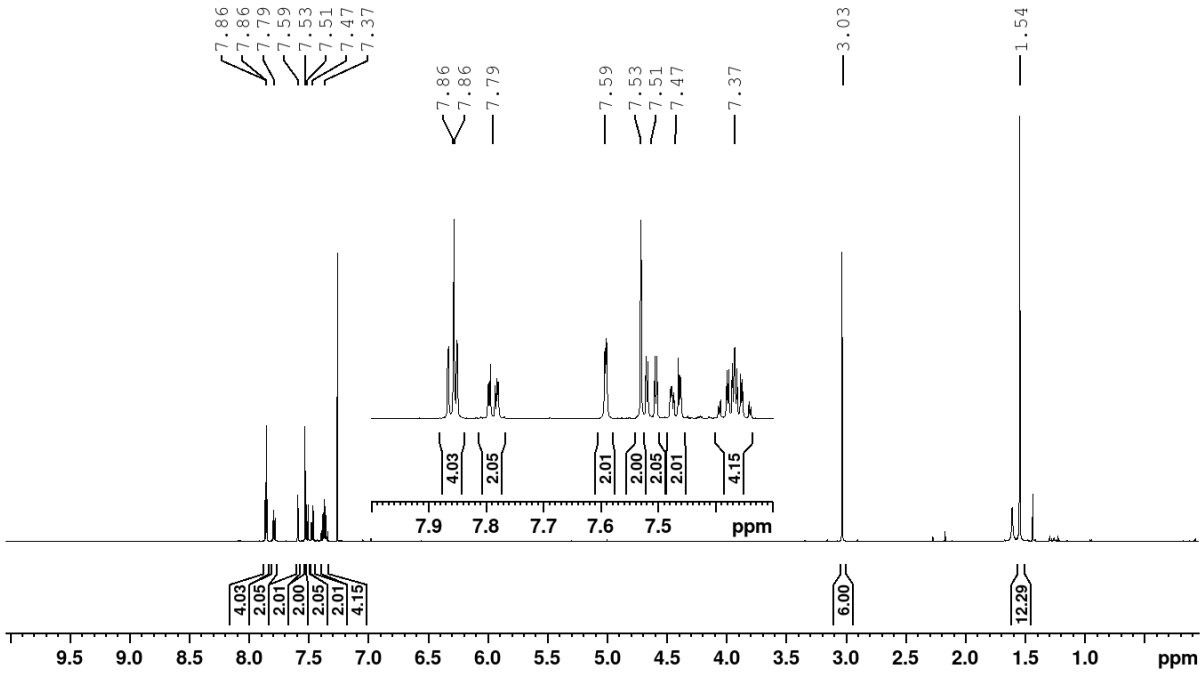

Figure S3.1. ^{1}H NMR spectrum of **nF** in $CDCl_3$.

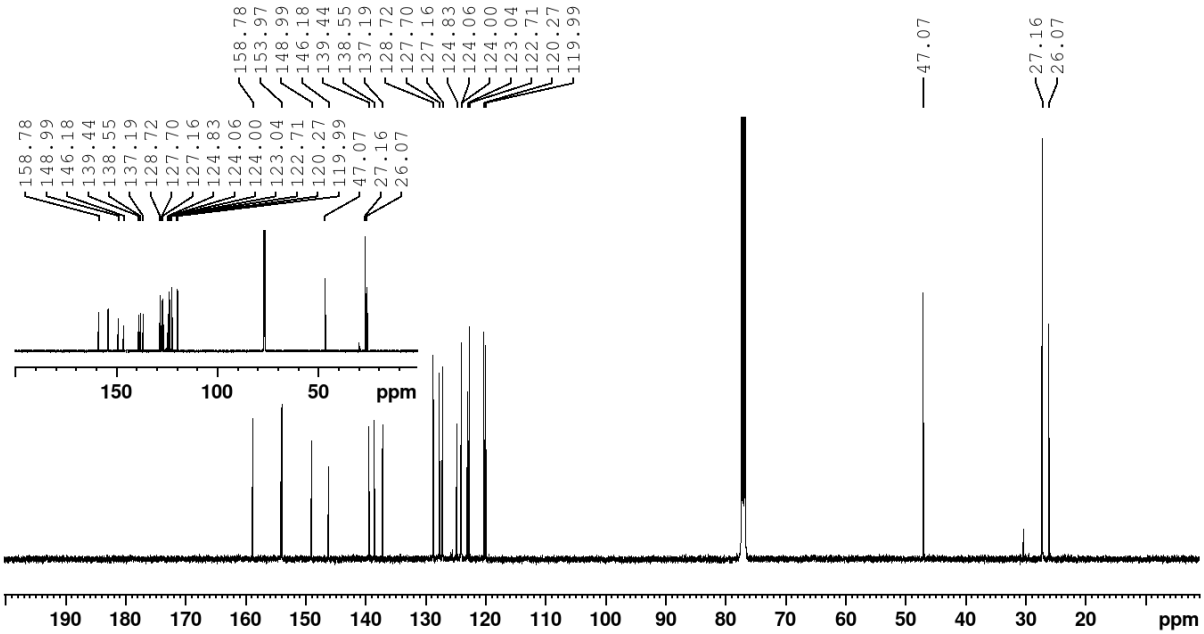

Figure S3.2. $^{13}C\{^{1}H\}$ NMR spectrum of the ligand **nF** in $CDCl_3$.

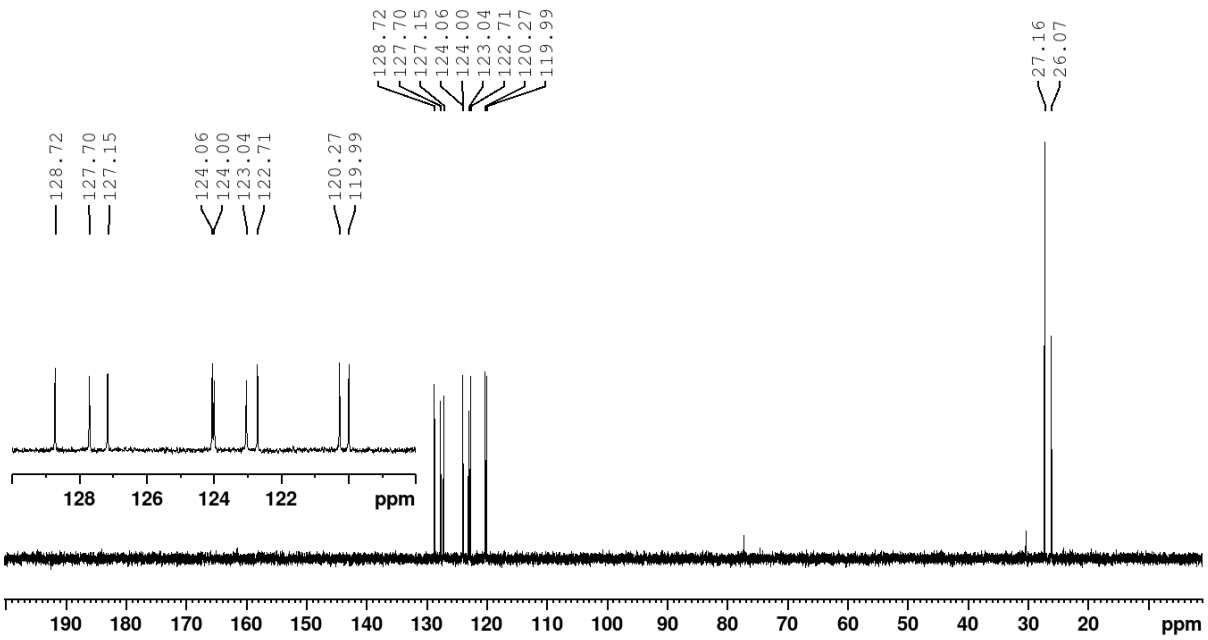

Figure S3.3. DEPT NMR spectrum of the ligand **nF** in $CDCl_3$.

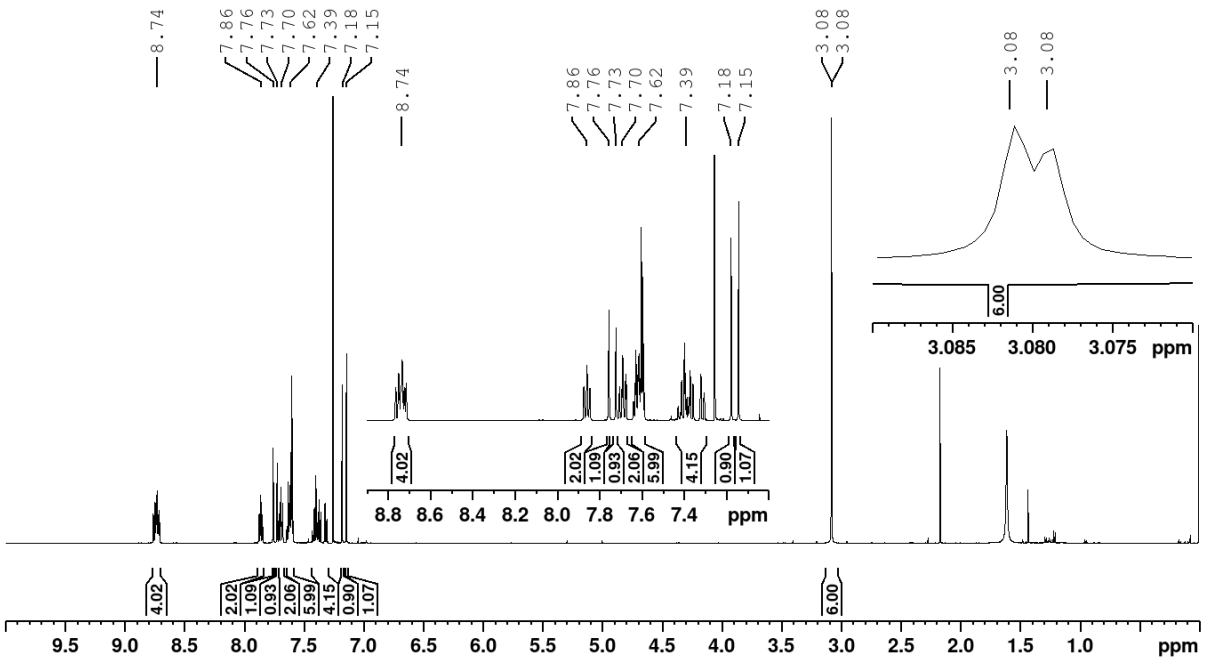

Figure S3.4. ^1H NMR spectrum of the ligand **nP** in $CDCl_3$.

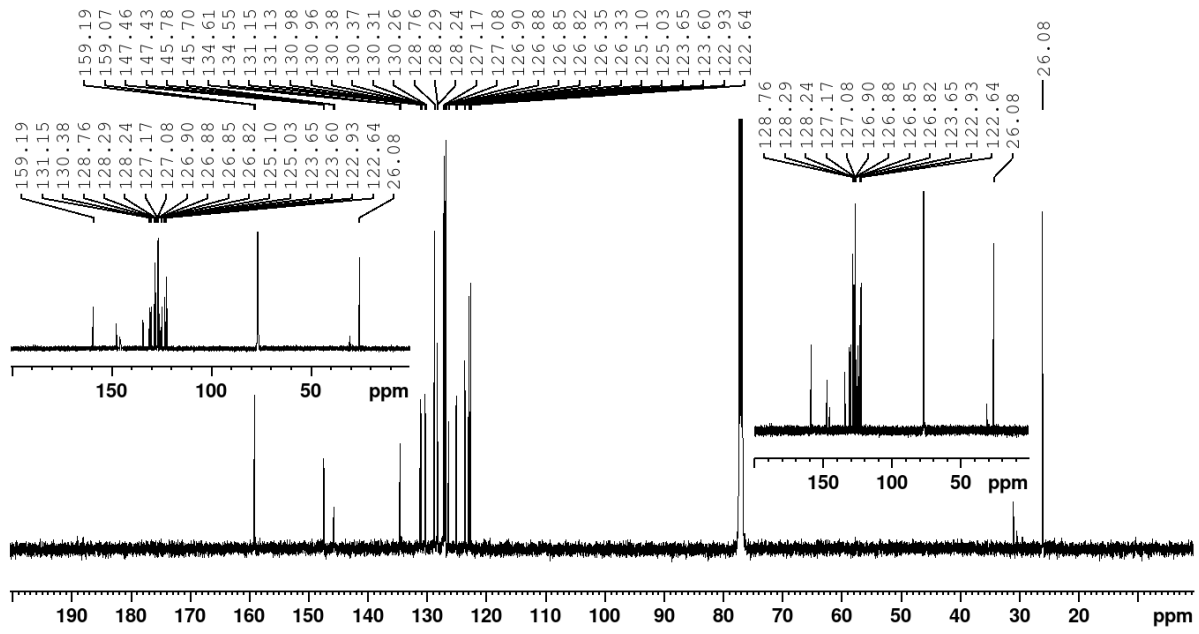

Figure S3.5. $^{13}C\{^{1}H\}$ NMR spectrum of the ligand **nP** in $CDCl_3$.

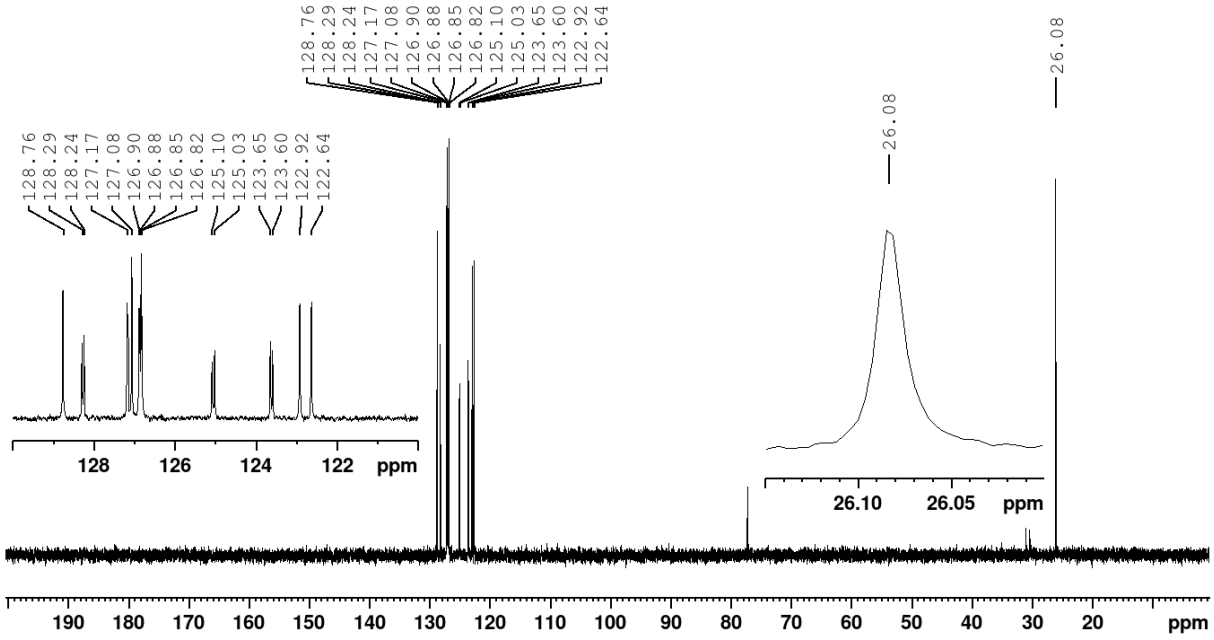

Figure S3.6. DEPT NMR spectrum of the ligand **nP** in $CDCl_3$.

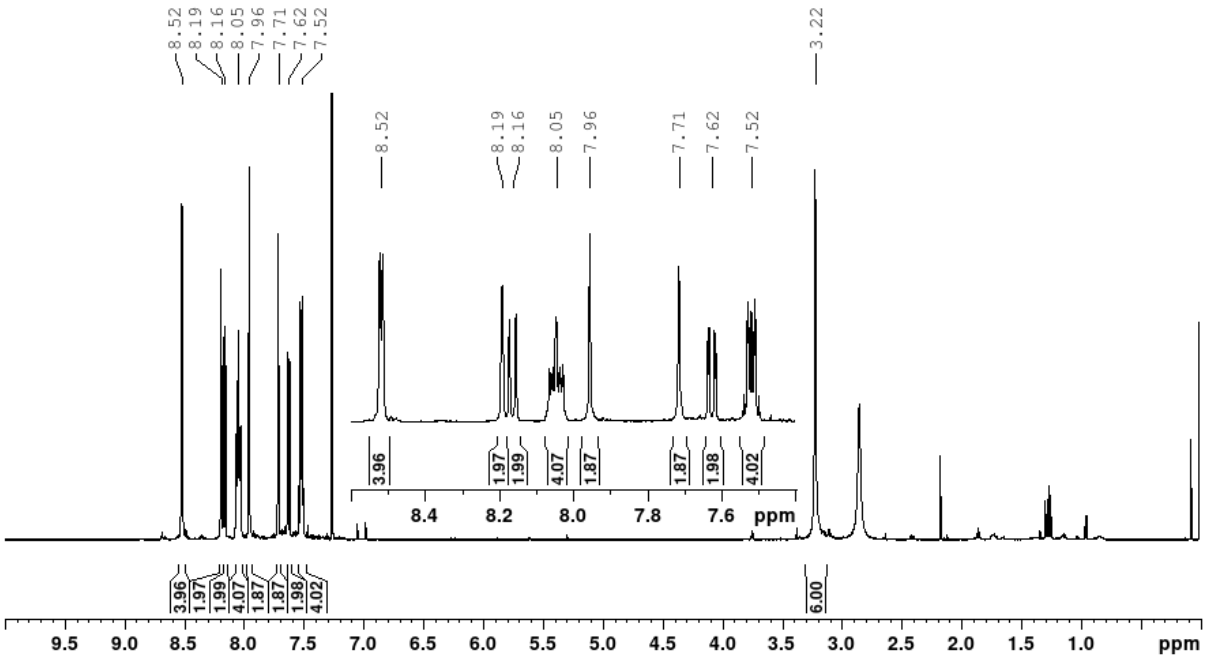

Figure S3.7. ^{1}H NMR spectrum of the ligand **nA** in $CDCl_3$.

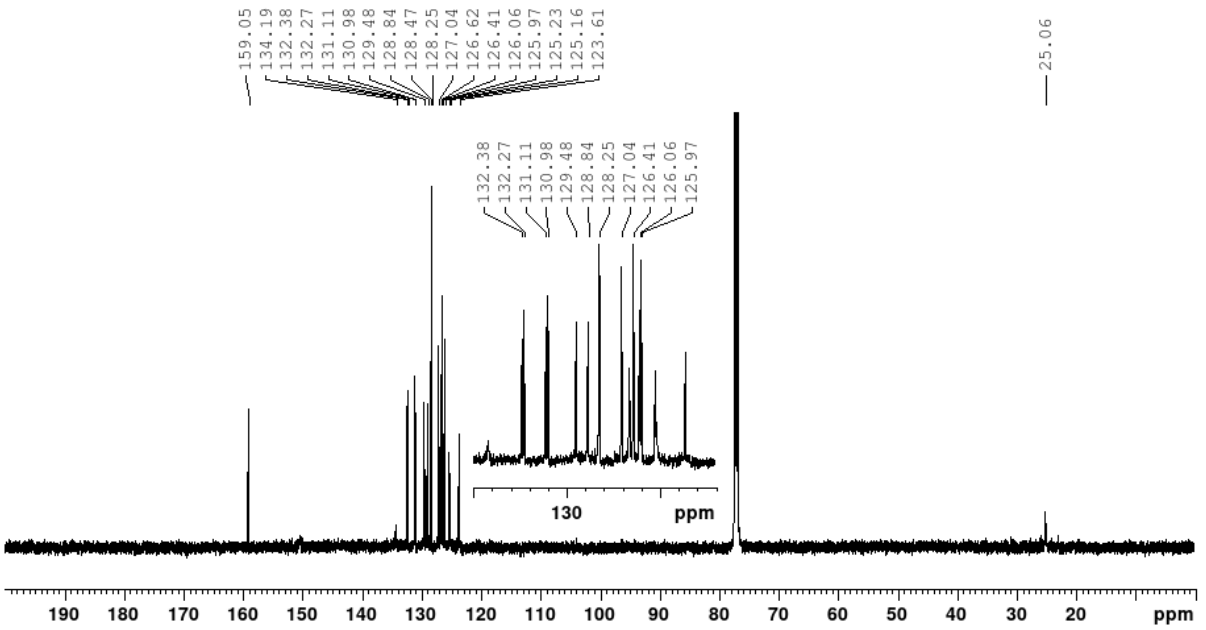

Figure S3.8. $^{13}C\{^{1}H\}$ NMR spectrum of the ligand **nA** in $CDCl_3$.

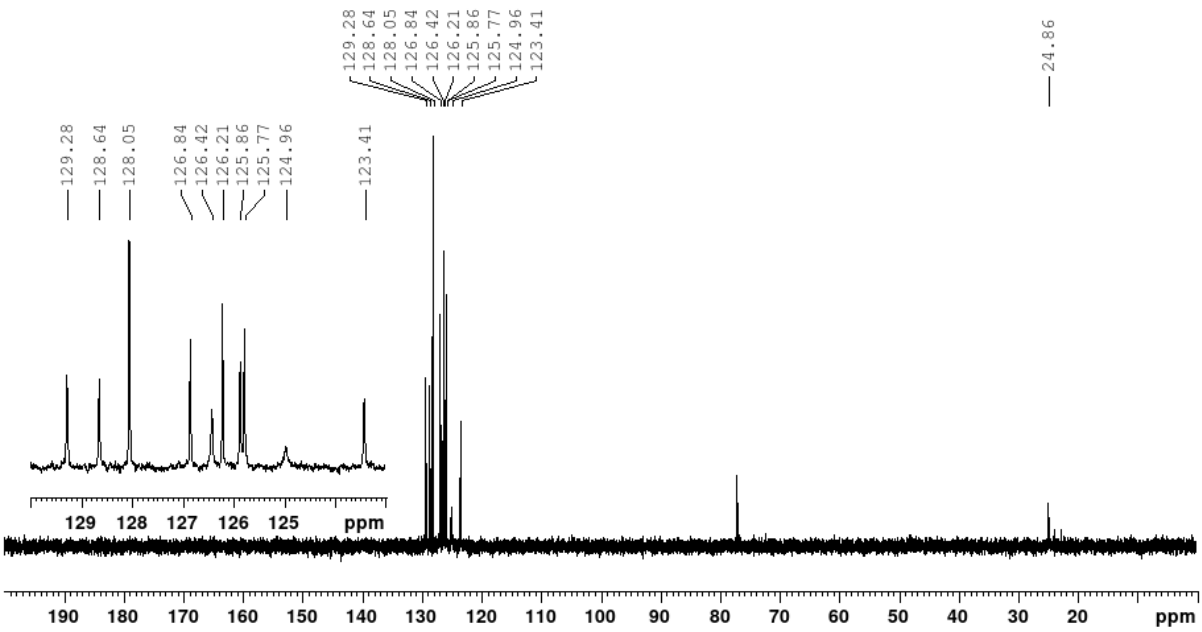

Figure S3.9. DEPT NMR spectrum of the ligand **nA** in $CDCl_3$.

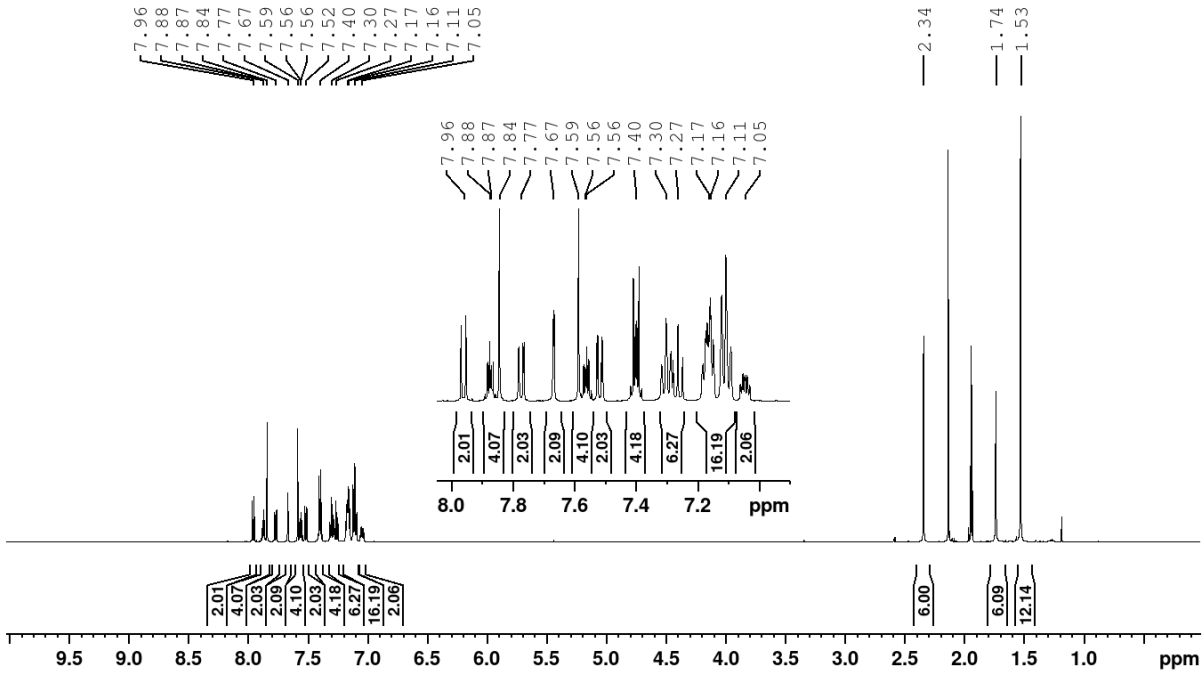

Figure S3.10. ^{1}H NMR spectrum of the complex **CunF** [Cu(**nF**)(xant)]PF_6 in CD_3CN.

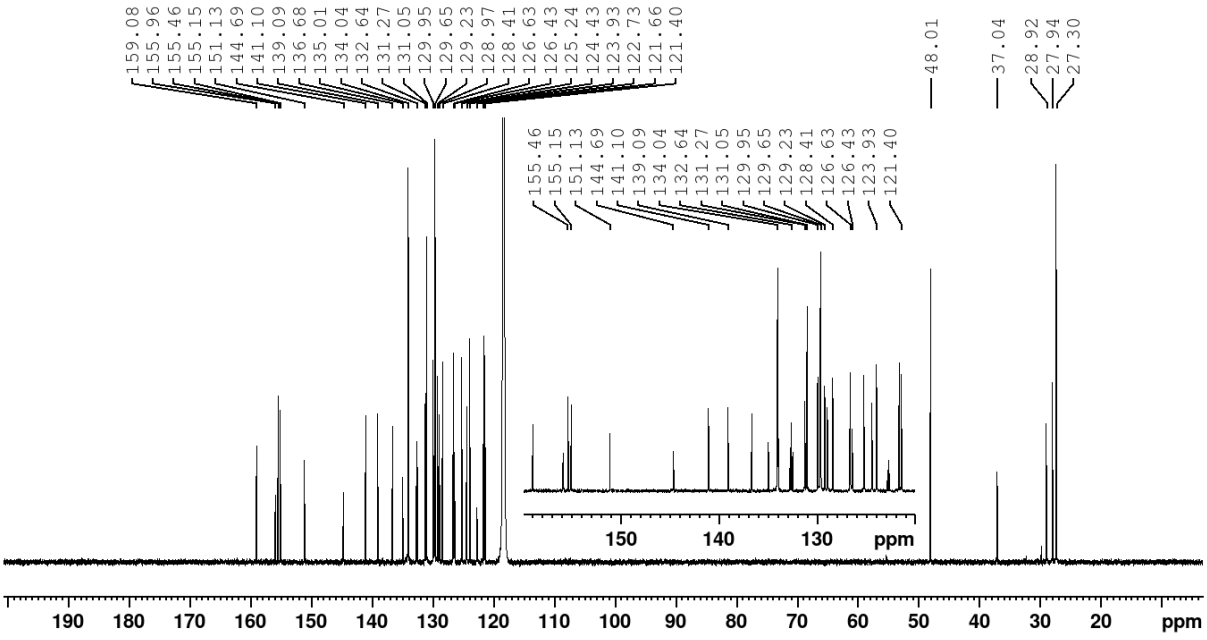

Figure S3.11. $^{13}C\{^{1}H\}$ NMR spectrum of the complex **CunF** [Cu(**nF**)(xant)]PF_6 in CD_3CN.

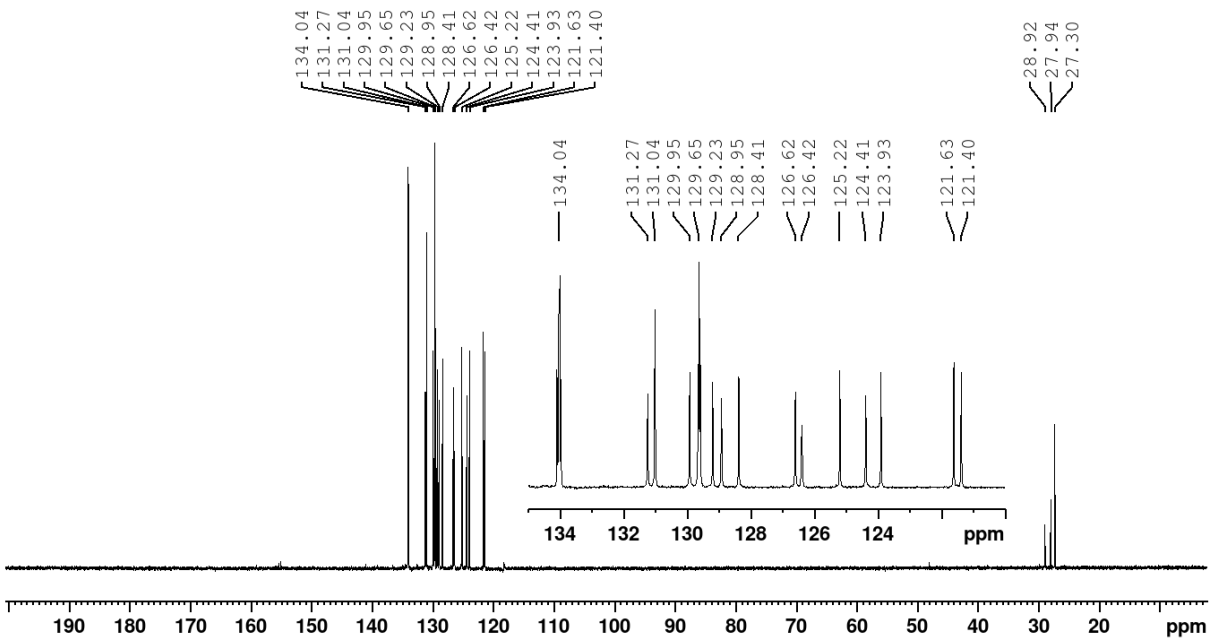

Figure S3.12. DEPT NMR spectrum of the complex **CunF** [Cu(**nF**)(xant)]PF_6 in CD_3CN.

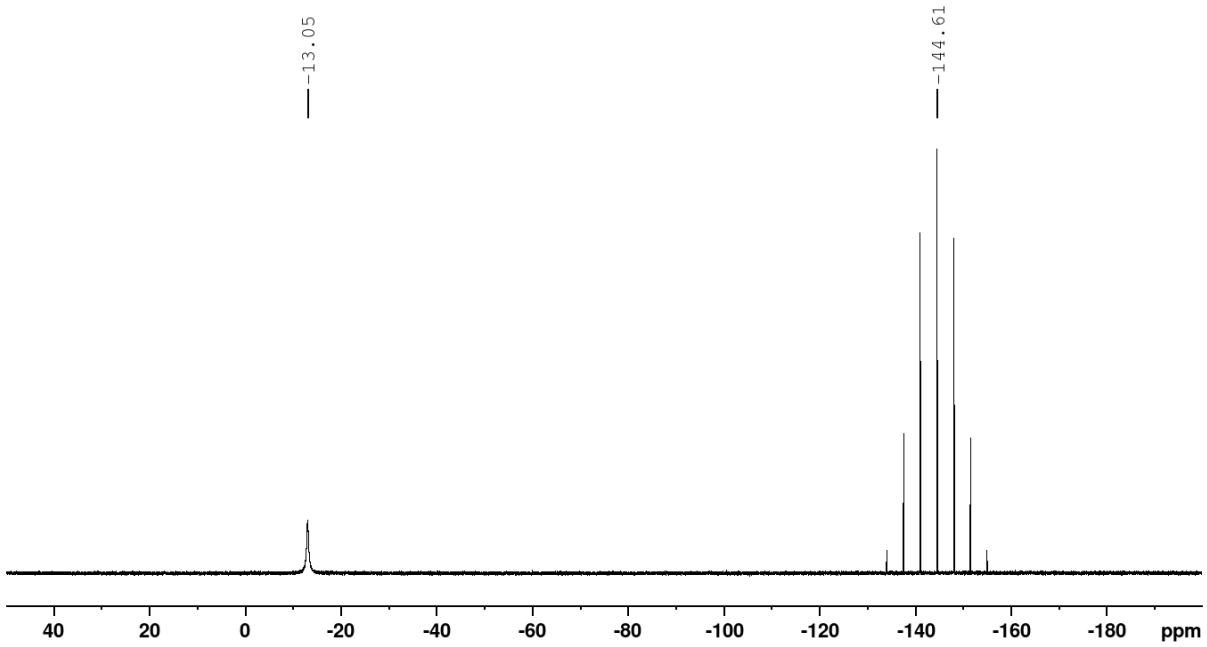

Figure S3.13. $^{31}P\{^1H\}$ NMR spectrum of the complex **CunF** [Cu(**nF**)(xant)]PF_6 in CD_3CN.

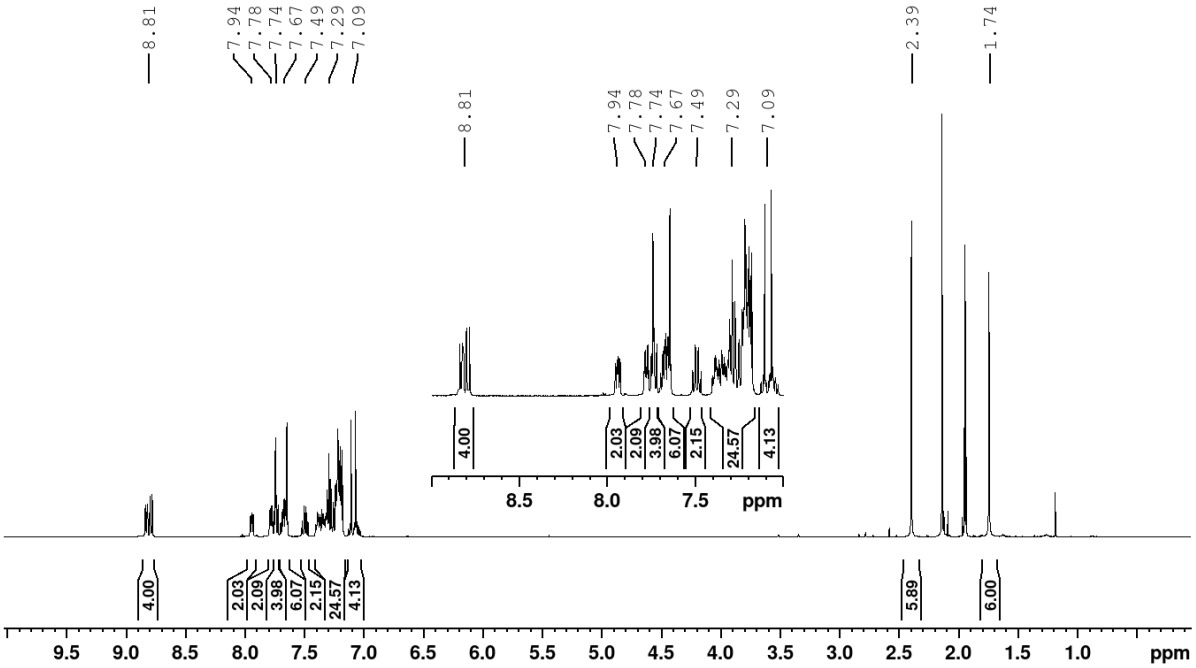

Figure S3.14. ^{1}H NMR spectrum of the complex **CunP** [Cu(**nP**)(xant)]PF_6 in CD_3CN.

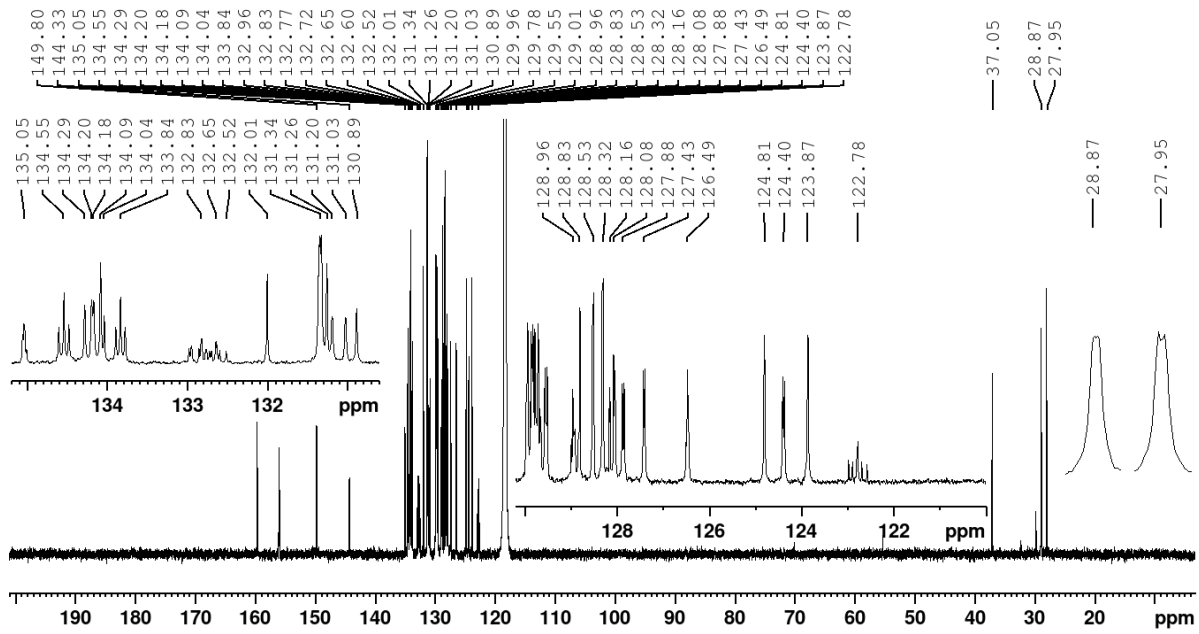

Figure S3.15. $^{13}C\{^{1}H\}$ NMR spectrum of the complex **CunP** [Cu(**nP**)(xant)]PF_6 in CD_3CN.

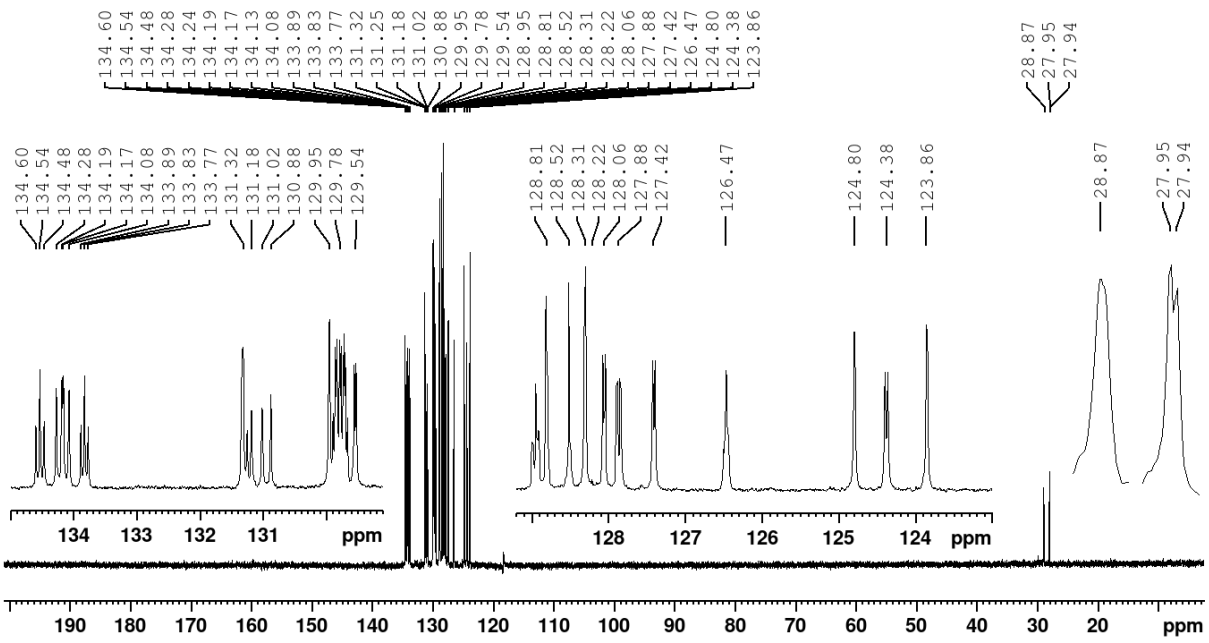

Figure S3.16. DEPT NMR spectrum of the complex **CunP** [Cu(**nP**)(xant)]PF_6 in CD_3CN.

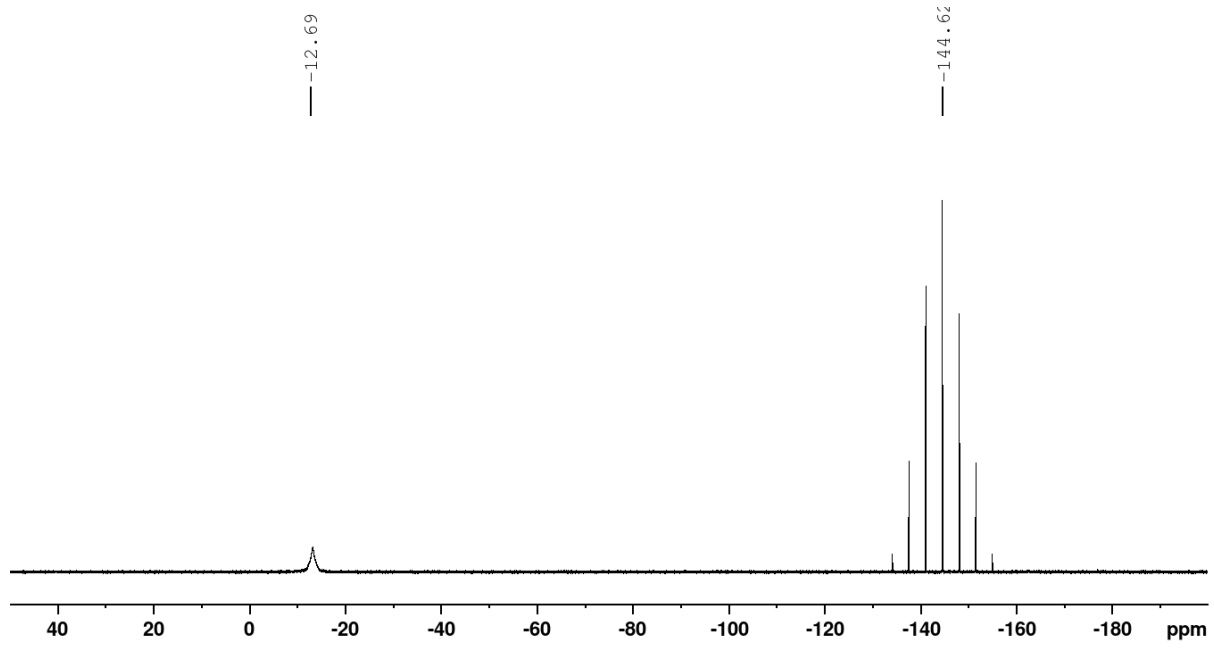

Figure S3.17. $^{31}P\{^1H\}$ NMR spectrum of the complex **CunP** [Cu(**nP**)(xant)]PF_6 in CD_3CN.

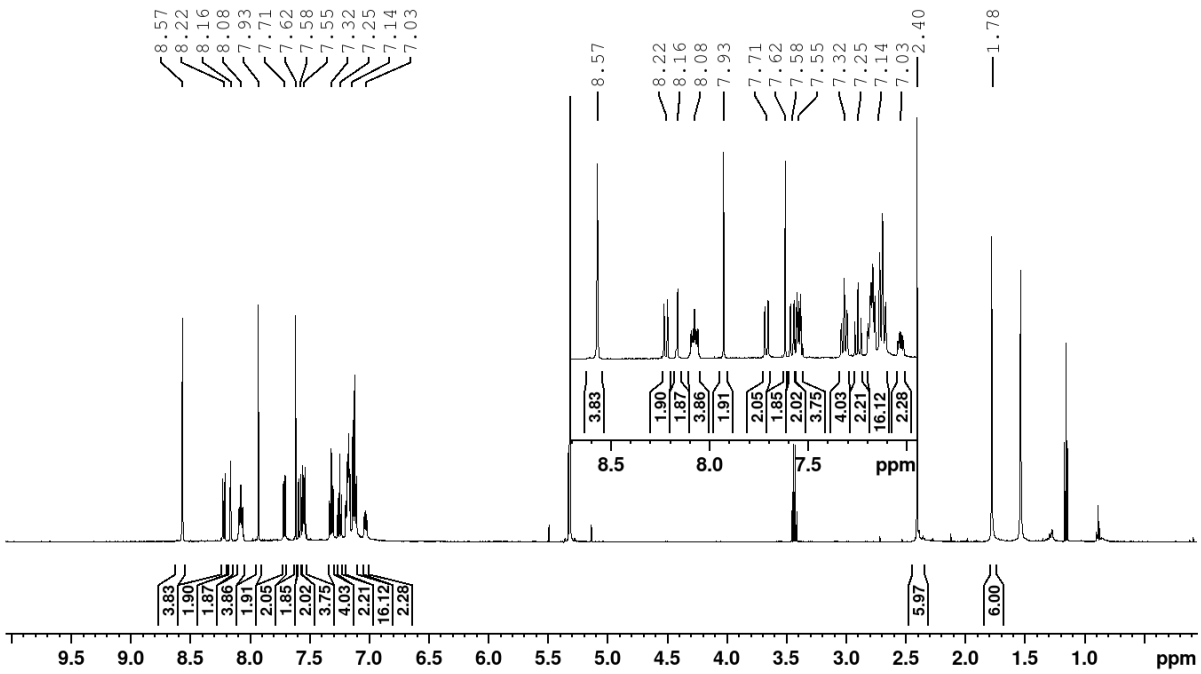

Figure S3.18. ^{1}H NMR spectrum of the complex **CunA** [Cu(**nA**)(xant)]PF_6 in CD_2Cl_2.

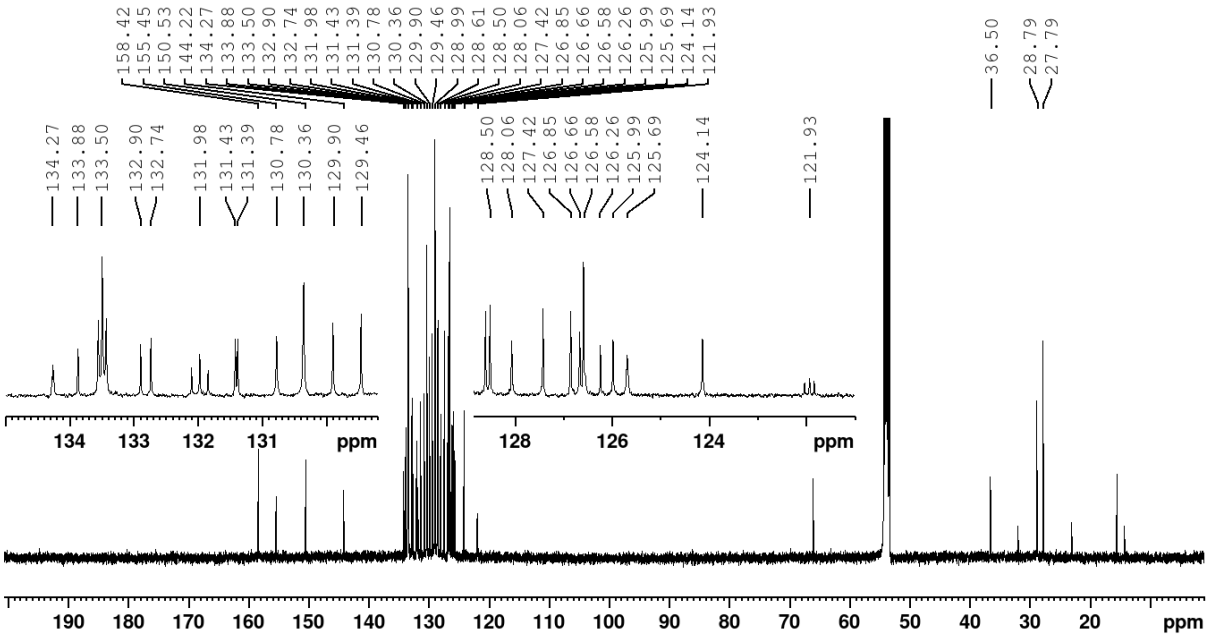

Figure S3.19. $^{13}C\{^{1}H\}$ NMR spectrum of the complex **CunA** [Cu(**nA**)(xant)]PF_6 in CD_2Cl_2.

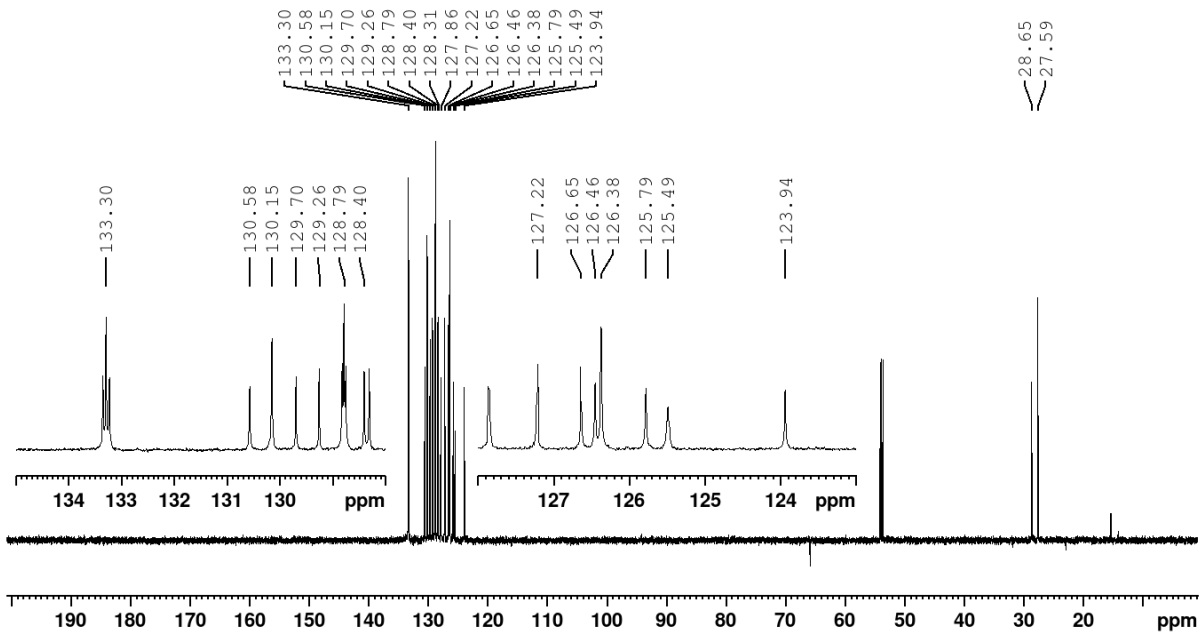

Figure S3.20. DEPT NMR spectrum of the complex **CunA** [Cu(**nA**)(xant)]PF_6 in CD_2Cl_2.

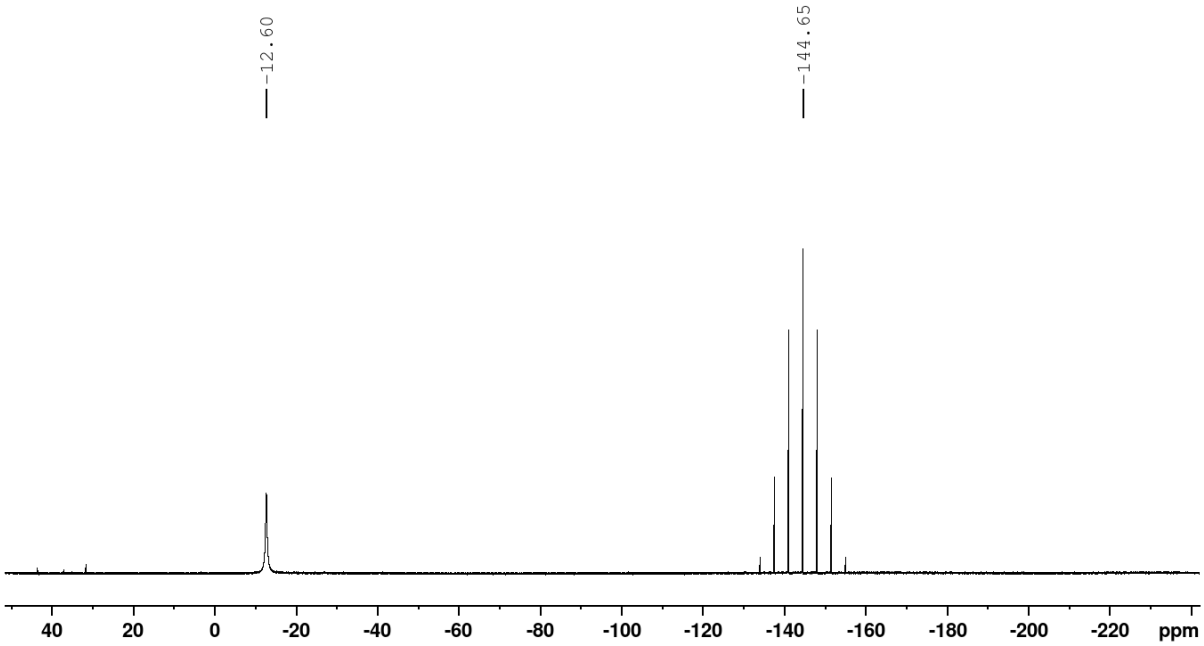

Figure S3.21. $^{31}P\{^1H\}$ NMR spectrum of the complex **CunA** [Cu(**nA**)(xant)]PF_6 in CD_2Cl_2.

4 MS Spectra

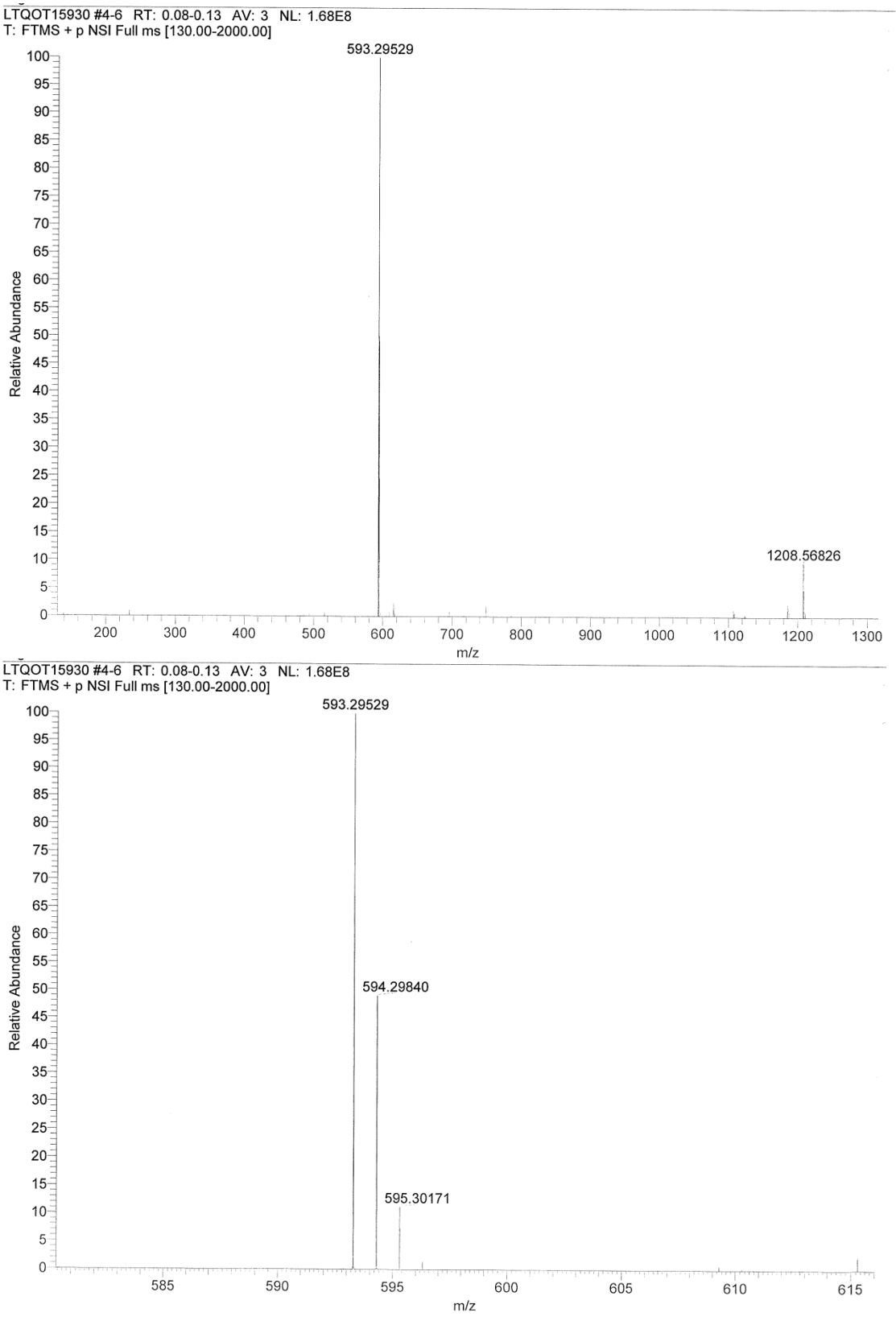

Figure S4.1. High resolution ESI mass (HRMS) spectrum of **nF**.

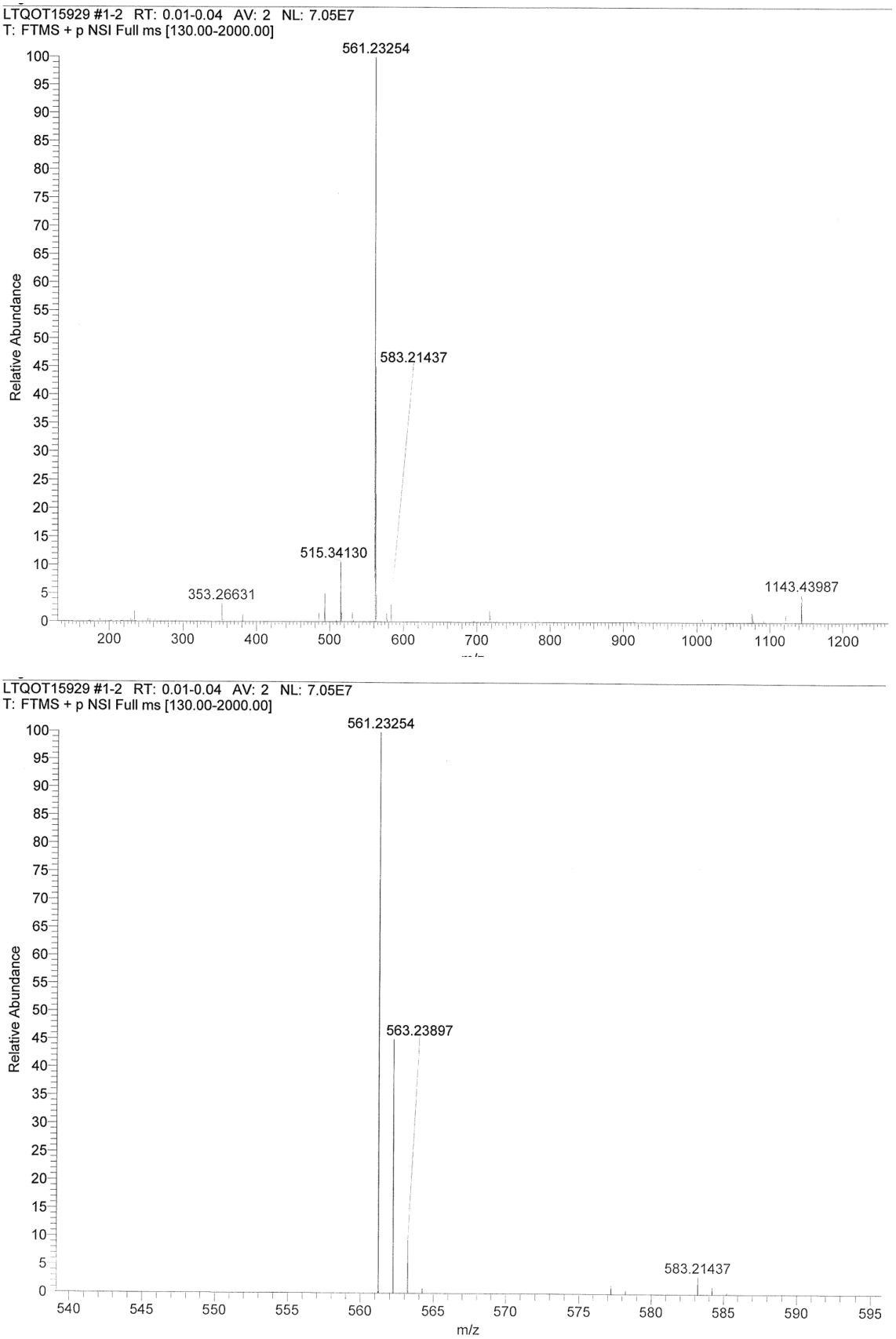

Figure S4.2. High resolution ESI mass (HRMS) spectrum of **nP**.

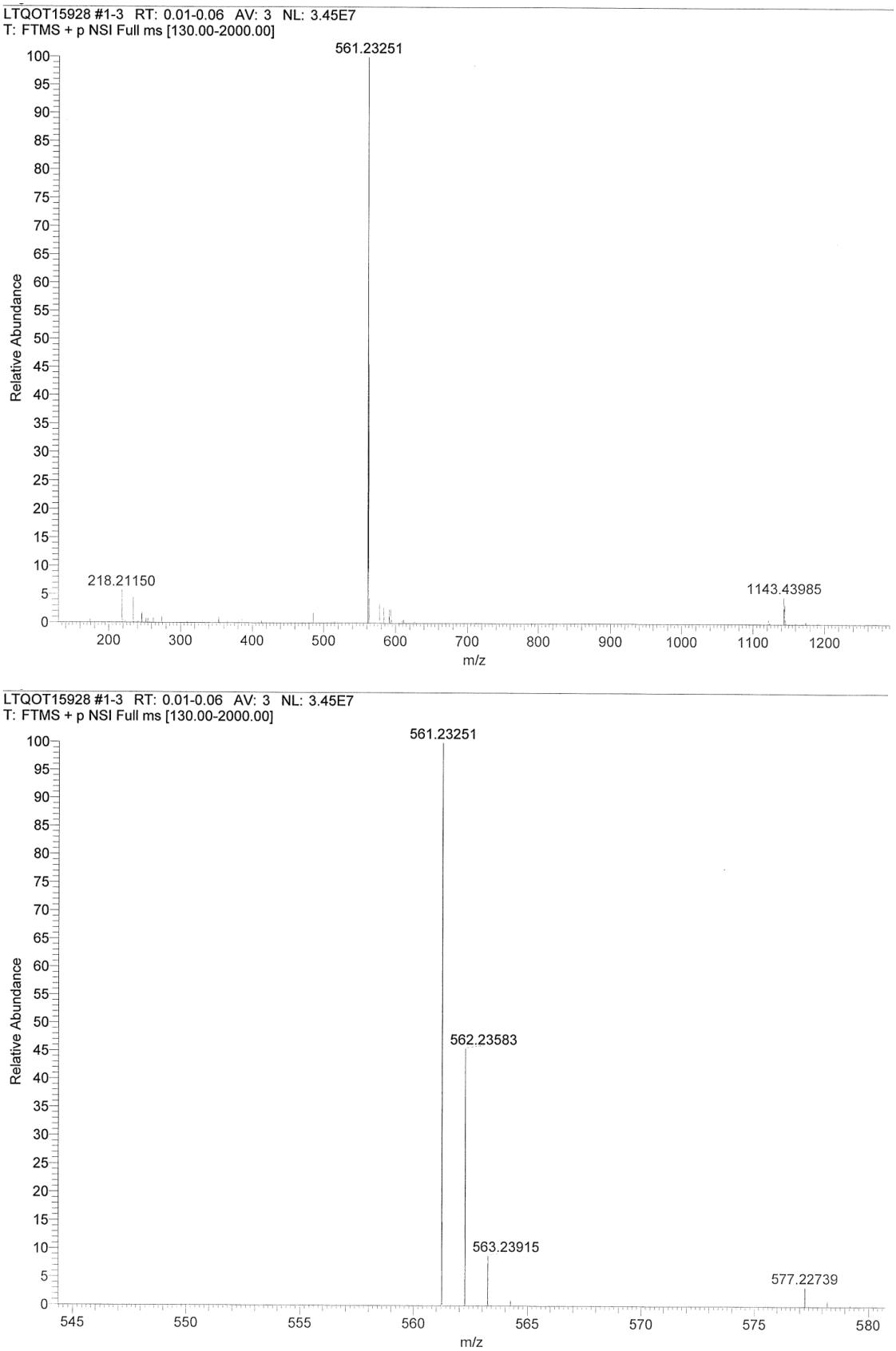

Figure S4.3. High resolution ESI mass (HRMS) spectrum of **nA**.

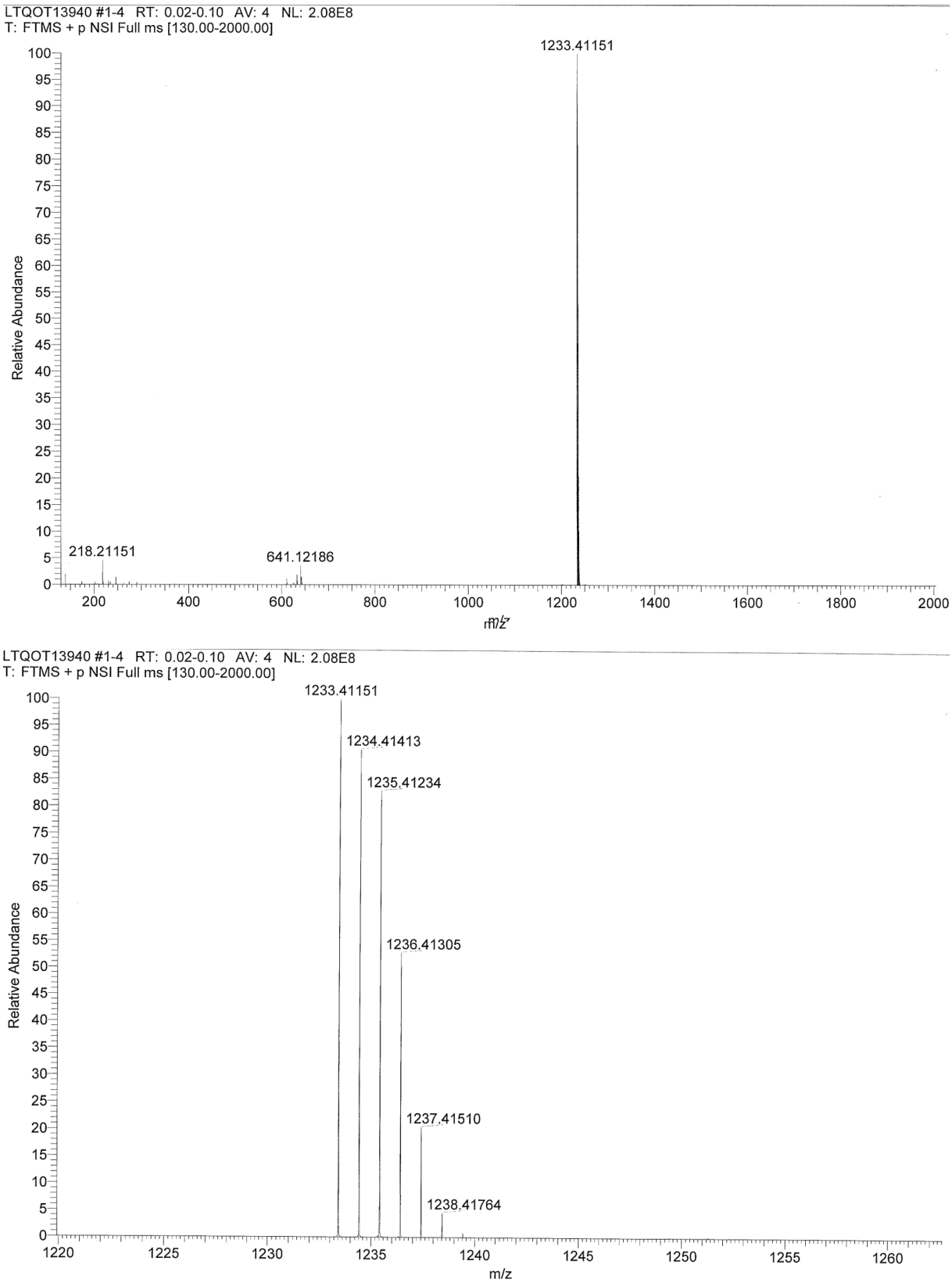

Figure S4.4. High resolution ESI mass (HRMS) spectrum of [Cu(**nF**)(xant)]PF_6: **CunF**.

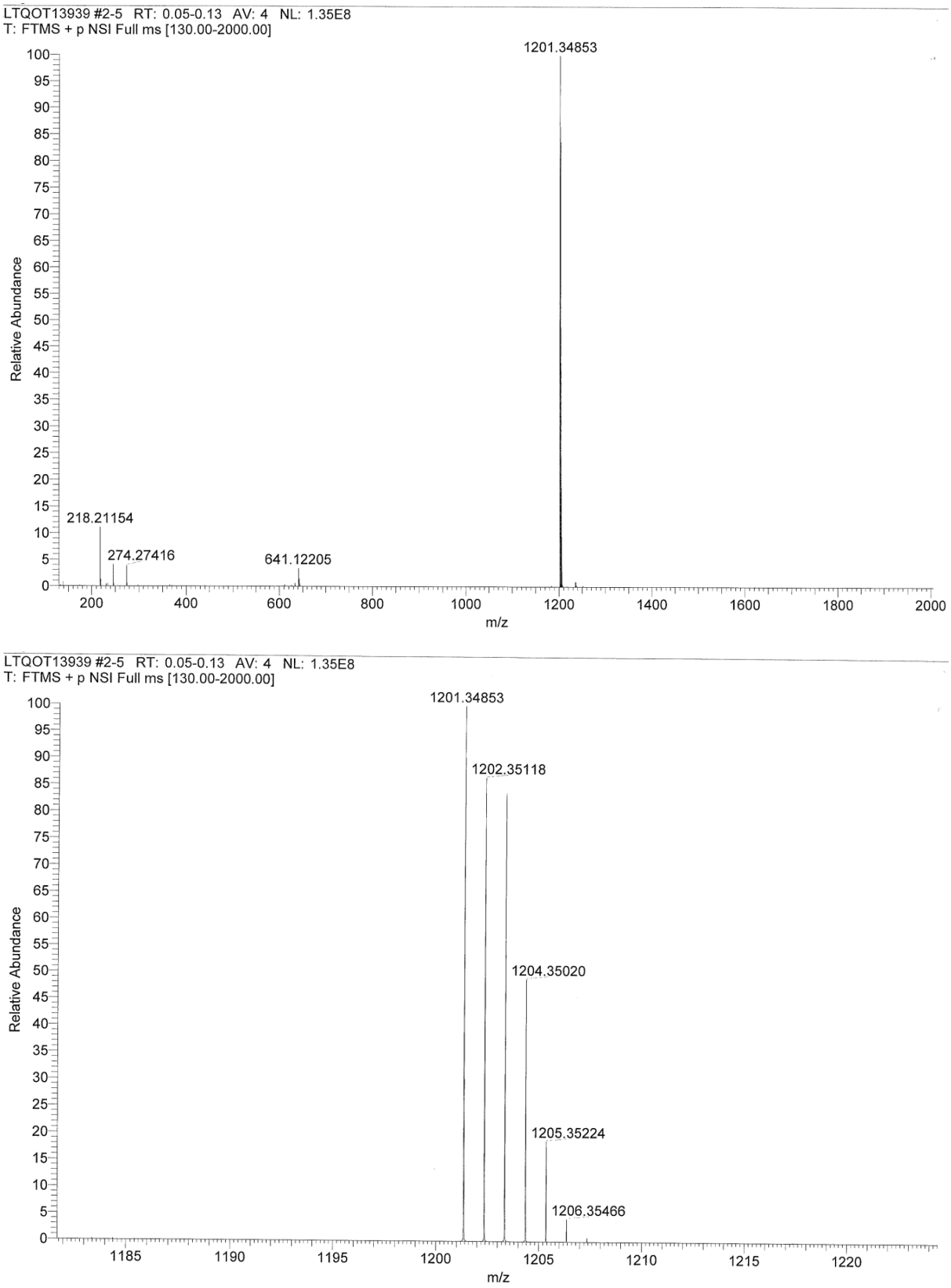

Figure S4.5. High resolution ESI mass (HRMS) spectrum of [Cu(**nP**)(xant)]PF_6: **CunP**.

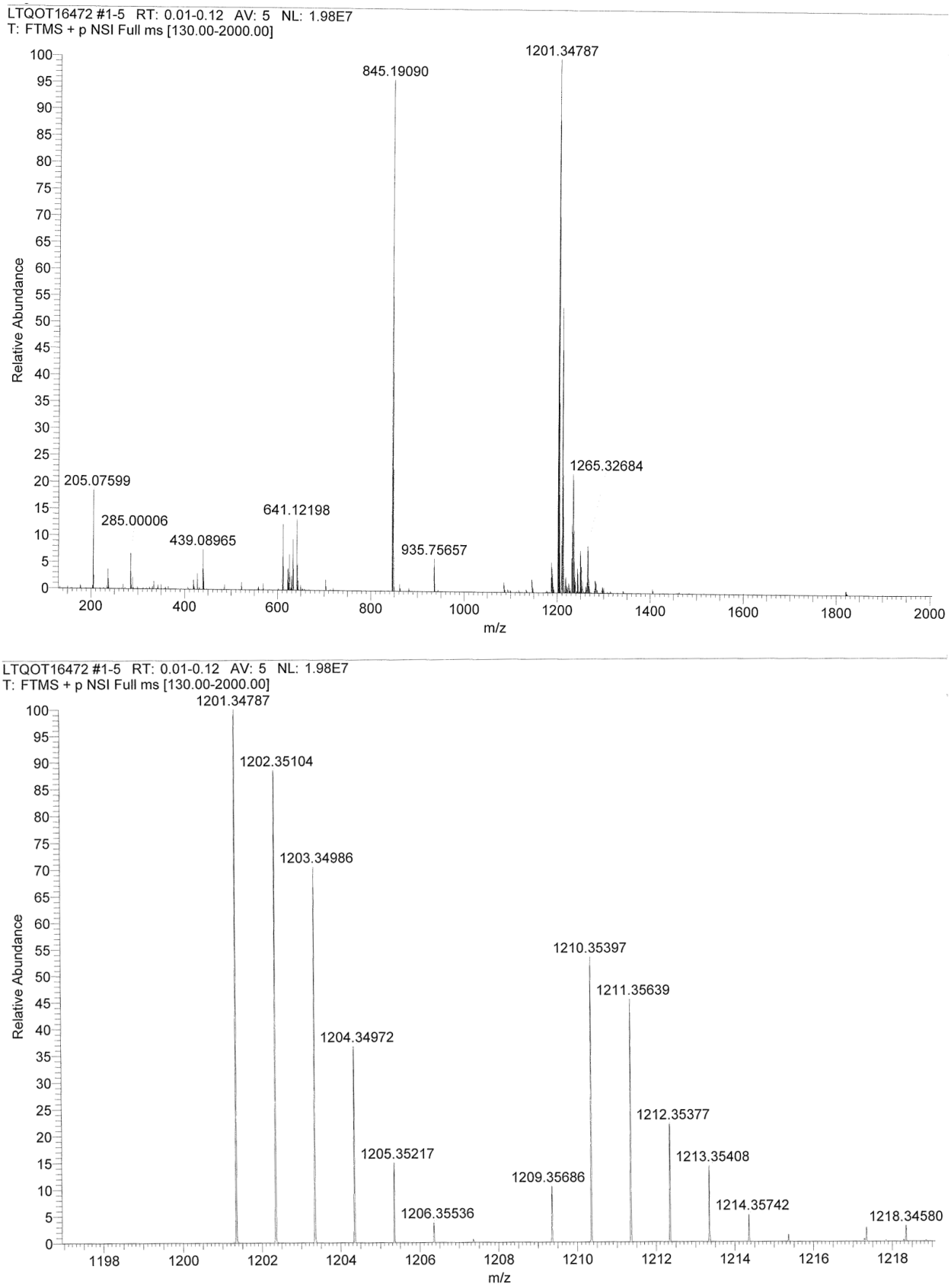

Figure S4.6. High resolution ESI mass (HRMS) spectrum of [Cu(**nA**)(xant)]PF_6: **CunA**.

5 Structural Data

Single crystals containing **CunA** were obtained by slow crystallization at room temperature from a concentrated dichloromethane/diethyl ether solution and then with *n*-hexane. Crystal growth was completed after 14 days.

The crystal comprises two domains described by a 0.6364° rotation around the [0.55 -0.81 0.18] (rec) or [0.82 -0.56 0.11] (dir) axis. Both domains were indexed separately and the data were reduced to a dataset containing intensity data of both domains (HKLF 5). During the refinement a parameter for the domain ratio was freely refined to 0.411(6). A refinement of a possible additional inversion twinning was not conducted as the Flack parameter differed only marginally from zero within a 3-sigma-criterion.

CunA crystallizes as a solvate containing 2.31 molecules of dichloromethane per complex molecule, disordered over three positions (freely refined site occupancies: 0.808(5), 0.795(5), 0.706(5)). Additional co-crystallized solvent is located in channels along the *a* axis. The electron density associated with this highly disordered solvent (presumably *n*-hexane) could not be satisfactorily described with a molecular model and was taken into account applying the BYPASS algorithm as implemented in OLEX2.[3a,15]

Table S5.1. Crystallographic data of the complex **CunA**.

Complex	**CunA** (solvate)
CCDC Number [a]	2491672
Empirical formula	$[C_{81}H_{60}CuN_2OP_2][PF_6] \cdot (2.31\ CH_2Cl_2)$
Empirical Formula weight [g/mol]	1543.81
Temperature [K]	100(2)
Wavelength [Å]	1.54184
Crystal system, space group	orthorhombic, $P2_12_12_1$ (19)
Unit cell dimensions [Å] and [°]	a = 14.94930(10) α = 90 b = 22.1311(2) β = 90 c = 23.2701(3) γ = 90
Volume [Å^3]	7698.78(13)
Z, Calculated density [g/cm^{-3}]	4, 1.332
Absorption coefficient [mm^{-1}]	2.966
F(000)	3172
Crystal size [mm]	0.447 x 0.092 x 0.078
Theta range for data collection	2.76° < θ < 77.87°
Limiting indices	-18<=h<=18, -28<=k<=27, -29<=l<=29
Reflections collected / indep. / obs.	17461 / 17461 / 16497
Completeness to θ = 67.68°	100.0 %
Absorption correction	Gaussian
Max. and min. transmission	1.000 and 0.507
Refinement method	Full-matrix least-squares on F^2
Data / restraints / parameters	17461 / 0 / 936
Goodness-of-fit on F^2	1.040
Final R indices [I>2σ(I)]	R_1 = 0.0513, wR_2 = 0.1370
R indices (all data)	R_1 = 0.0546, wR_2 = 0.1407
Absolute structure parameter	0.033(10)
Largest diff. peak and hole [e.A^{-3}]	0.697 and -0.422

[a] The CCDC reference numbers shown contain the supplementary crystallographic data for this paper. The data can be accessed free of charge at the Cambridge Crystallographic Data Centre via www.ccdc.cam.ac.uk/data_request/cif

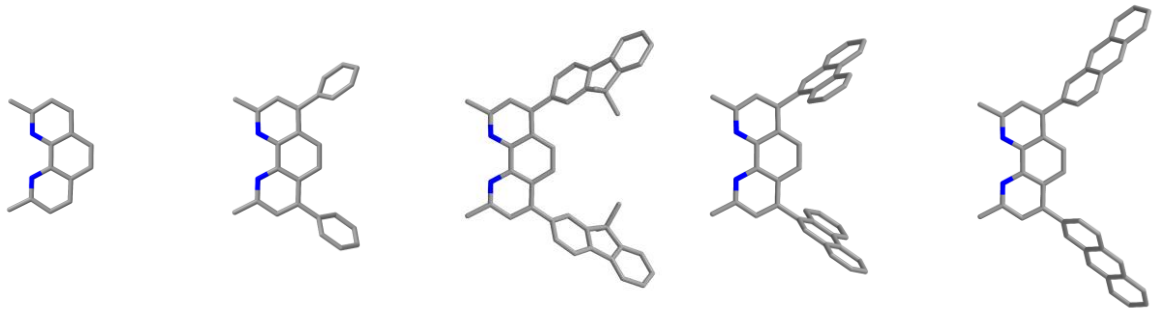

Figure S5.1. PBE0/def2-TZVP ground state structures of the ligands. Left to right: **neo**, **bcp**, **nF**, **nP**, **nA**. Carbon atoms are displayed in gray and nitrogen atoms in blue. Hydrogen atoms are omitted for visual clarity.

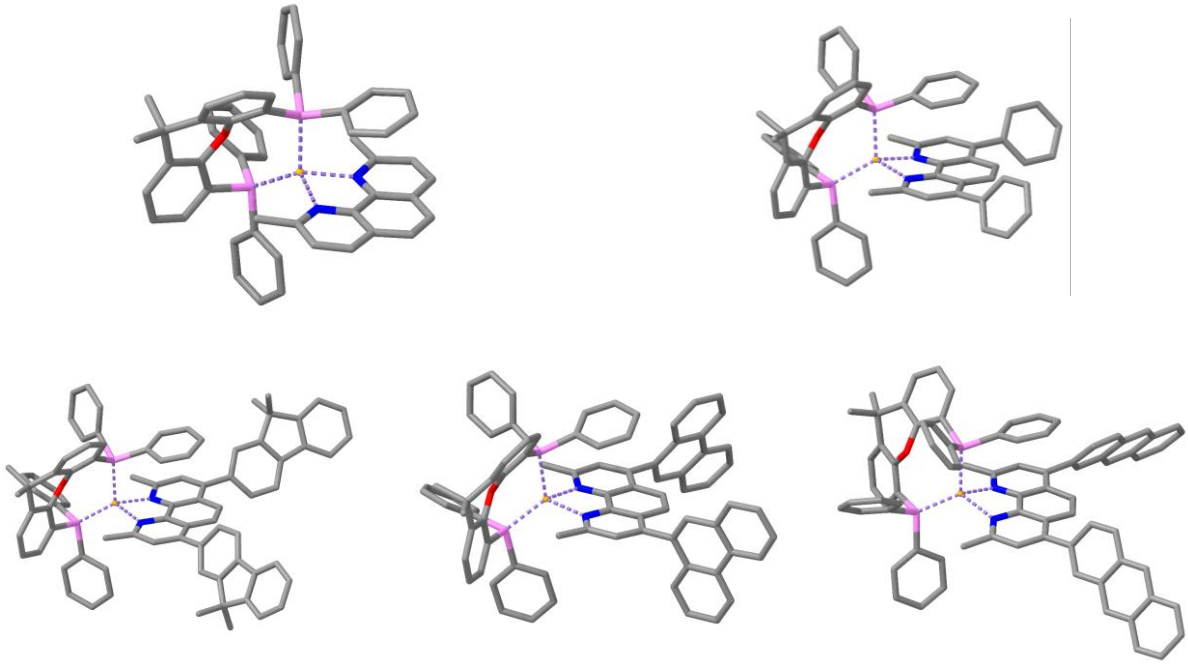

Figure S5.2. PBE0/def2-TZVP ground state structures of the complexes. Top row: **Cuneo**, **Cubcp**. Bottom row: **CunF**, **CunP**, **CunA**. Carbon atoms are displayed in gray, nitrogen atoms in blue, oxygen atoms in red, phosphorus atoms in pink and copper atoms in orange. Hydrogen atoms are omitted for visual clarity.

Excited-State Structures – Complexes' Singlets and Triplets

Table S5.2. Selected bond lengths (pm), bond angles (°), interplane angles θ (°) and torsion angles ϑ (°) of the optimized singlet excited state of all complexes obtained by TDDFT calculations (calc.). The C_{neo}-C_{sub} bond lengths describe the bond length between the respective substituent and the C_4/C_7 of **neo**. Torsion angles ϑ_1 and ϑ_2 express torsion angles along the substituent linkages from C_3-C_4-$C_{Sub1,1}$-$C_{Sub1,2}$ and C_8-C_7-$C_{Sub2,1}$-$C_{Sub2,2}$, where the second substituent carbon atom is on the same side as the stacking phenyl ring. Computations were performed on PBE0/def2-TZVP level. **CunA** yielded two excited states, one of MLCT nature and one of π_A-π_A* nature.

		S_1 **Cuneo**$_{calc.}$	S_1 **Cubcp**$_{calc.}$	S_1 **CunF**$_{calc.}$	S_1 **CunP**$_{calc.}$	$S_{1,MLCT}$ **CunA**$_{calc.}$	$S_{2,\pi\pi^*A}$ **CunA**$_{calc.}$
Cu-N1	/pm	205.5	203.5	204.0	204.2	209.5	209.7
Cu-N2		200.9	199.8	199.7	200.2	197.7	205.9
Cu-P1		237.3	234.7	235.2	236.4	231.5	226.6
Cu-P2		239.9	242.3	242.0	239.9	239.4	234.4
C_4-C_{sub1}		-	147.0	146.7	147.6	147.2	147.2
C_7-C_{sub2}		-	147.3	147.2	147.8	145.7	145.1
N-Cu-N	/°	83.5	83.1	82.9	83.3	82.2	80.4
P-Cu-P		105.0	109.9	109.2	107.1	108.5	113.5
θ		70.1	74.3	73.7	70.4	75.5	82.8
ϑ_{sub1}		-	-129.6	-132.5	-60.6	-131.0	-129.4
ϑ_{sub2}		-	49.7	50.6	111.3	139.1	140.0

Table S5.3. Selected bond lengths (pm), bond angles (°), interplane angles θ (°) and torsion angles ϑ (°) of the optimized T_1 excited state of all complexes obtained by DFT ΔSCF calculations (calc.). The C_{neo}-C_{sub} bond lengths describe the bond length between the respective substituent and the C_4/C_7 of **neo**. Torsion angles ϑ_1 and ϑ_2 express torsion angles along the substituent linkages from C_3-C_4-$C_{Sub1,1}$-$C_{Sub1,2}$ and C_8-C_7-$C_{Sub2,1}$-$C_{Sub2,2}$, where the second substituent carbon atom is on the same side as the stacking phenyl ring. Computations performed on PBE0/def2-TZVP level.

		$T_{1,MLCT}$ **Cuneo**$_{calc.}$	$T_{1,MLCT}$ **Cubcp**$_{calc.}$	$T_{1,MLCT}$ **CunF**$_{calc.}$	$T_{1,MLCT}$ **CunP**$_{calc.}$	$T_{1,\pi\pi^*A}$ **CunA**$_{calc.}$
Cu-N1	/pm	201.5	202.2	201.4	200.7	211.4
Cu-N2		198.0	196.8	196.1	198.3	210.0
Cu-P1		237.9	238.0	237.8	237.4	225.4
Cu-P2		240.4	240.4	240.3	239.1	232.5
C_4-C_{sub1}		-	147.1	147.2	147.5	147.3
C_7-C_{sub2}		-	147.2	146.9	148.1	146.5
N-Cu-N	/°	84.0	83.3	83.4	83.7	79.0
P-Cu-P		107.2	107.1	109.1	107.6	116.5
θ		70.4	71.0	71.6	70.7	83.8
ϑ_{sub1}		-	-129.1	-126.0	-59.8	-126.5
ϑ_{sub2}		-	48.6	45.0	91.8	132.5

6 Computational Data

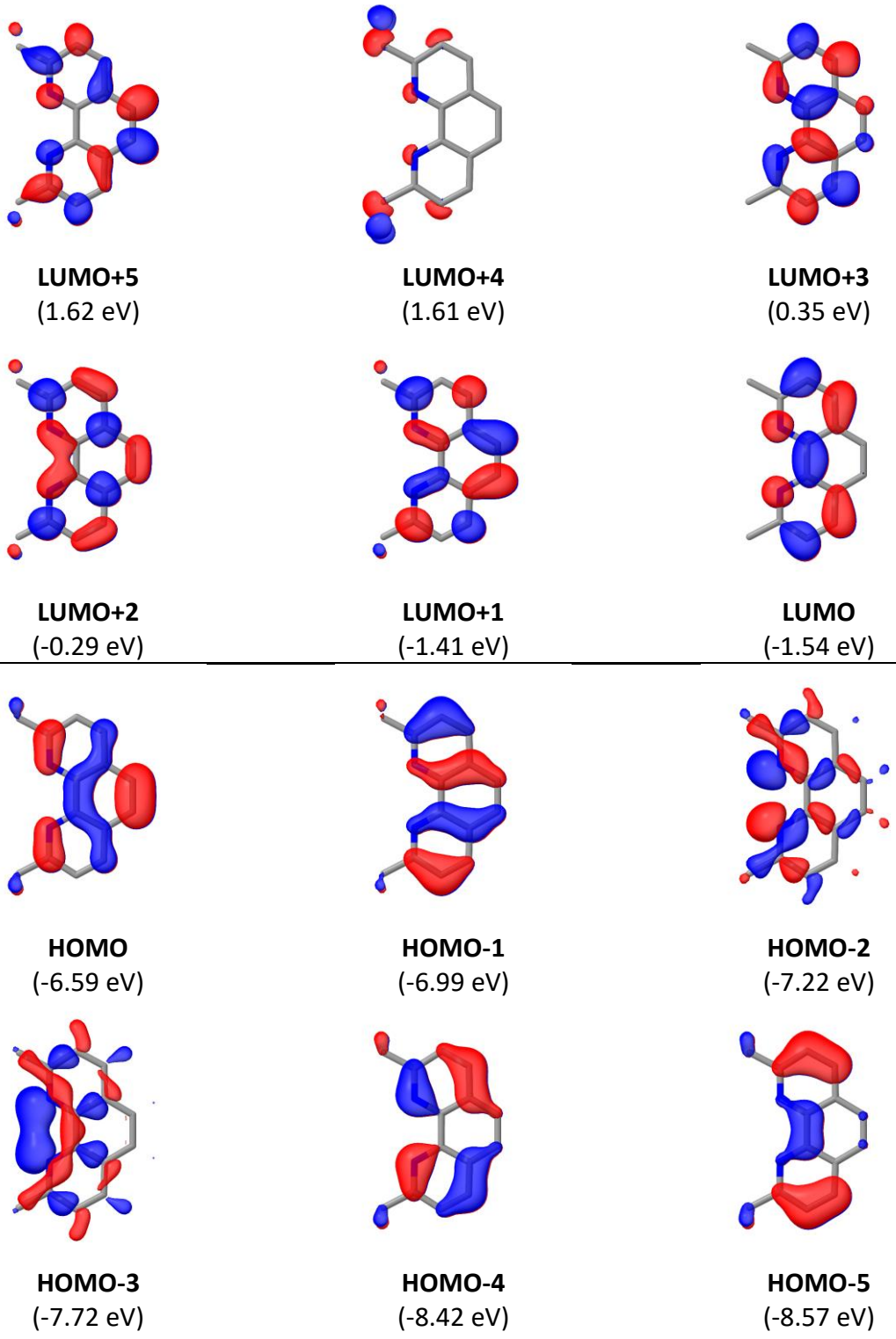

Figure S6.1. PBE0/def2-TZVP ground state frontier molecular orbitals of **neo** with respective energies in eV in parentheses. Positive lobes are depicted in red and negative in blue.

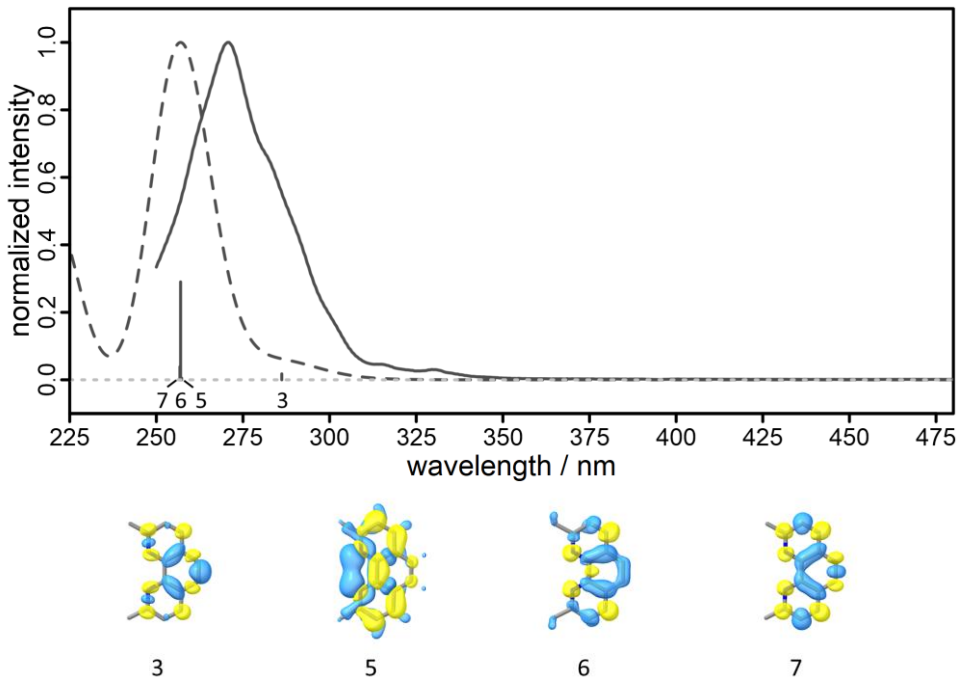

Figure S6.2. Normalized broadened calculated singlet excitation energies (dashed) with PBE0/def2-TZVP compared to the normalized experimental absorption spectrum (solid) of **neo** (top). Sticks are scaled down by a factor 0.25. Difference density plots corresponding to the excitation energies visualize the migration of electron density from cyan (-) to yellow (+) during the excitation (bottom).

Table S6.1. Excitation energies, oscillator strengths f_{osc} and corresponding transitions of **neo** obtained from TD-DFT with PBE0/def2-TZVP simulated in dichloromethane. Excitations with an oscillator strength > 0.01 and corresponding orbital contributions with an OC ≥ 0.15 are given.

State	**Exc. energy**		f_{osc}	**Dominant contribution**			**Transition**
#	cm^{-1}	nm		OC	occ. orb.	virt. orb.	
3	34938.8	286.2	0.070	0.278	HOMO-1	LUMO	$\pi_{neo} \rightarrow \pi_{neo}^*$
				0.714	HOMO	LUMO+1	$\pi_{neo} \rightarrow \pi_{neo}^*$
5	38860.9	257.3	0.020	0.843	HOMO-3	LUMO	$n_{neo} \rightarrow \pi_{neo}^*$
6	38912	257.0	1.161	0.643	HOMO-1	LUMO	$\pi_{neo} \rightarrow \pi_{neo}^*$
				0.254	HOMO	LUMO+1	$\pi_{neo} \rightarrow \pi_{neo}^*$
7	38938.4	256.8	0.155	0.678	HOMO-1	LUMO+1	$\pi_{neo} \rightarrow \pi_{neo}^*$
				0.155	HOMO	LUMO	$\pi_{neo} \rightarrow \pi_{neo}^*$

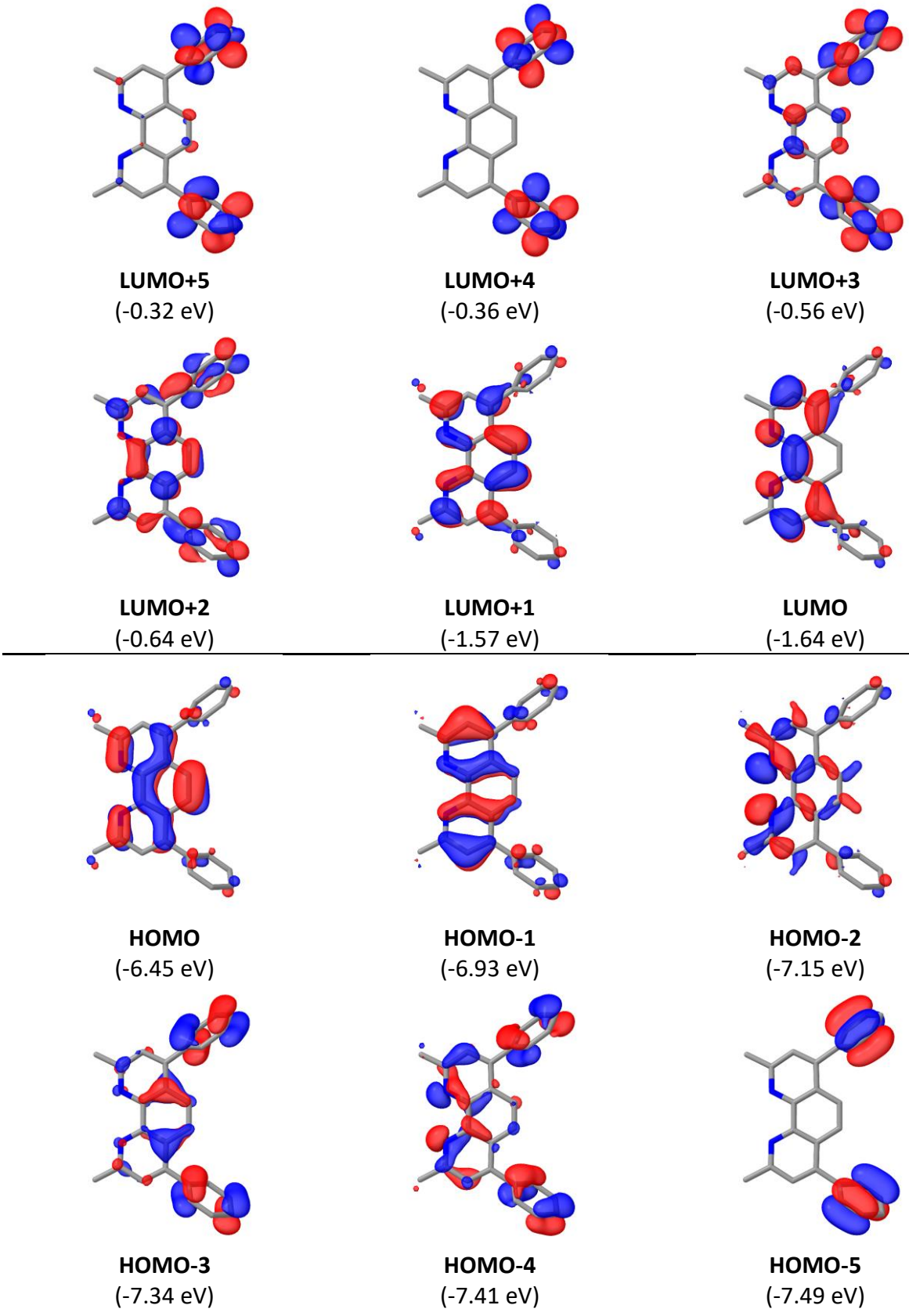

Figure S6.3. PBE0/def2-TZVP ground state frontier molecular orbitals of **bcp** with respective energies in eV in parentheses. Positive lobes are depicted in red and negative in blue.

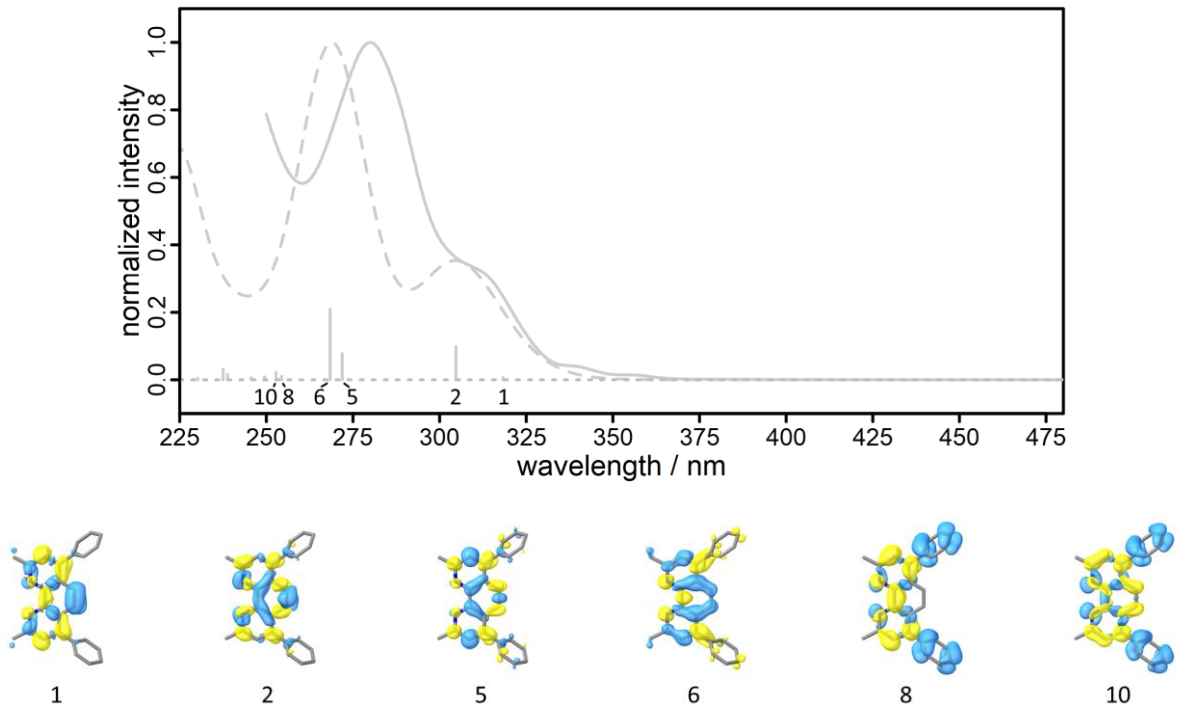

Figure S6.4. Normalized broadened calculated singlet excitation energies (dashed) with PBE0/def2-TZVP compared to the normalized experimental absorption spectrum (solid) of **bcp** (top). Sticks are scaled down by a factor 0.25. Difference density plots corresponding to the excitation energies visualize the migration of electron density from cyan (-) to yellow (+) during the excitation (bottom).

Table S6.2. Excitation energies, oscillator strengths f_{osc} and corresponding transitions of **bcp** obtained from TD-DFT with PBE0/def2-TZVP simulated in dichloromethane. Excitations with an oscillator strength > 0.01 and corresponding orbital contributions with an OC ≥ 0.15 are given.

State	Exc. energy		f_{osc}	Dominant contribution			Transition
#	cm^{-1}	nm		OC	#	cm^{-1}	nm
1	31414.6	318.3	0.026	0.852	HOMO	LUMO	$\pi_{neo} \rightarrow \pi_{neo}^*$
2	32824.0	304.7	0.392	0.876	HOMO	LUMO+1	$\pi_{neo} \rightarrow \pi_{neo}^*$
5	36782.6	271.9	0.311	0.655	HOMO-1	LUMO+1	$\pi_{neo} \rightarrow \pi_{neo}^*$
				0.170	HOMO	LUMO+2	$\pi_{neo} \rightarrow \pi_{neo}^*$
6	37253.0	268.4	0.840	0.713	HOMO-1	LUMO	$\pi_{neo} \rightarrow \pi_{neo}^*$
8	39306.0	254.4	0.041	0.157	HOMO-7	LUMO	$n_{neo} \rightarrow \pi_{neo}^*$
				0.636	HOMO-3	LUMO	$\pi_{neo,Ph} \rightarrow \pi_{neo}^*$
10	39559.7	252.8	0.087	0.181	HOMO-7	LUMO+1	$n_{neo} \rightarrow \pi_{neo}^*$
				0.264	HOMO-4	LUMO	$\pi_{neo,Ph} \rightarrow \pi_{neo}^*$
				0.324	HOMO-3	LUMO+1	$\pi_{neo,Ph} \rightarrow \pi_{neo}^*$

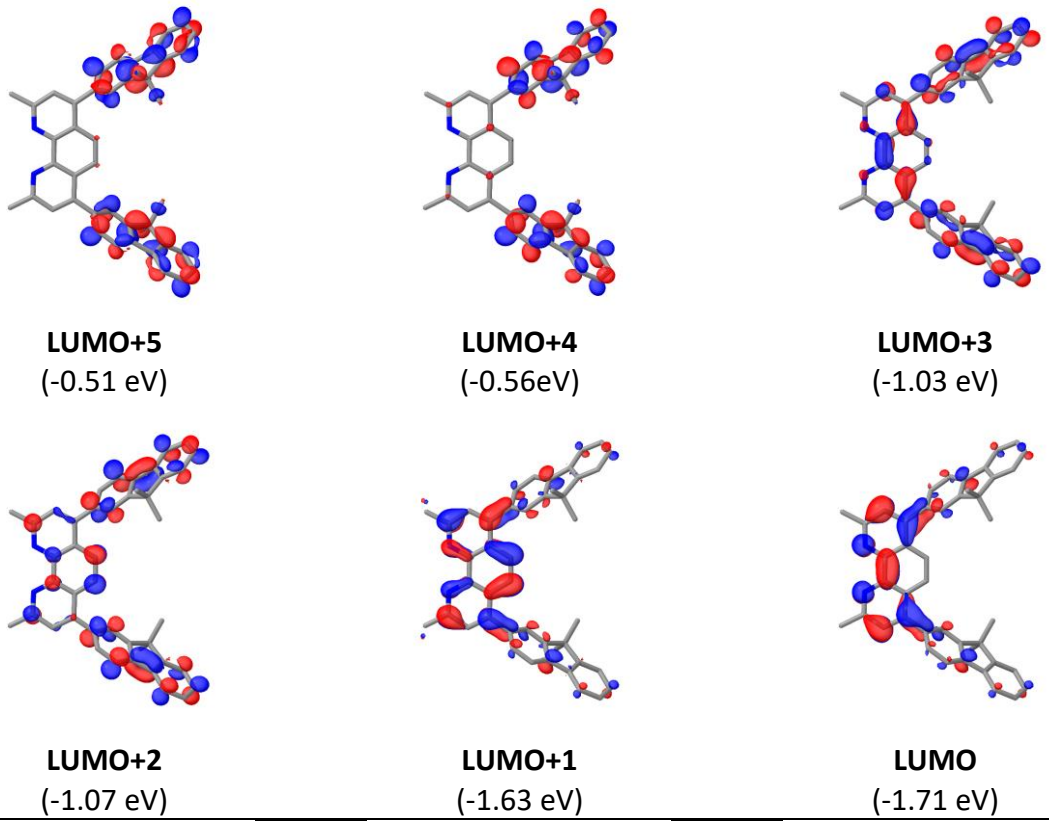

Figure S6.5. PBE0/def2-TZVP ground state frontier molecular orbitals of **nF** with respective energies in eV in parentheses. Positive lobes are depicted in red and negative in blue.

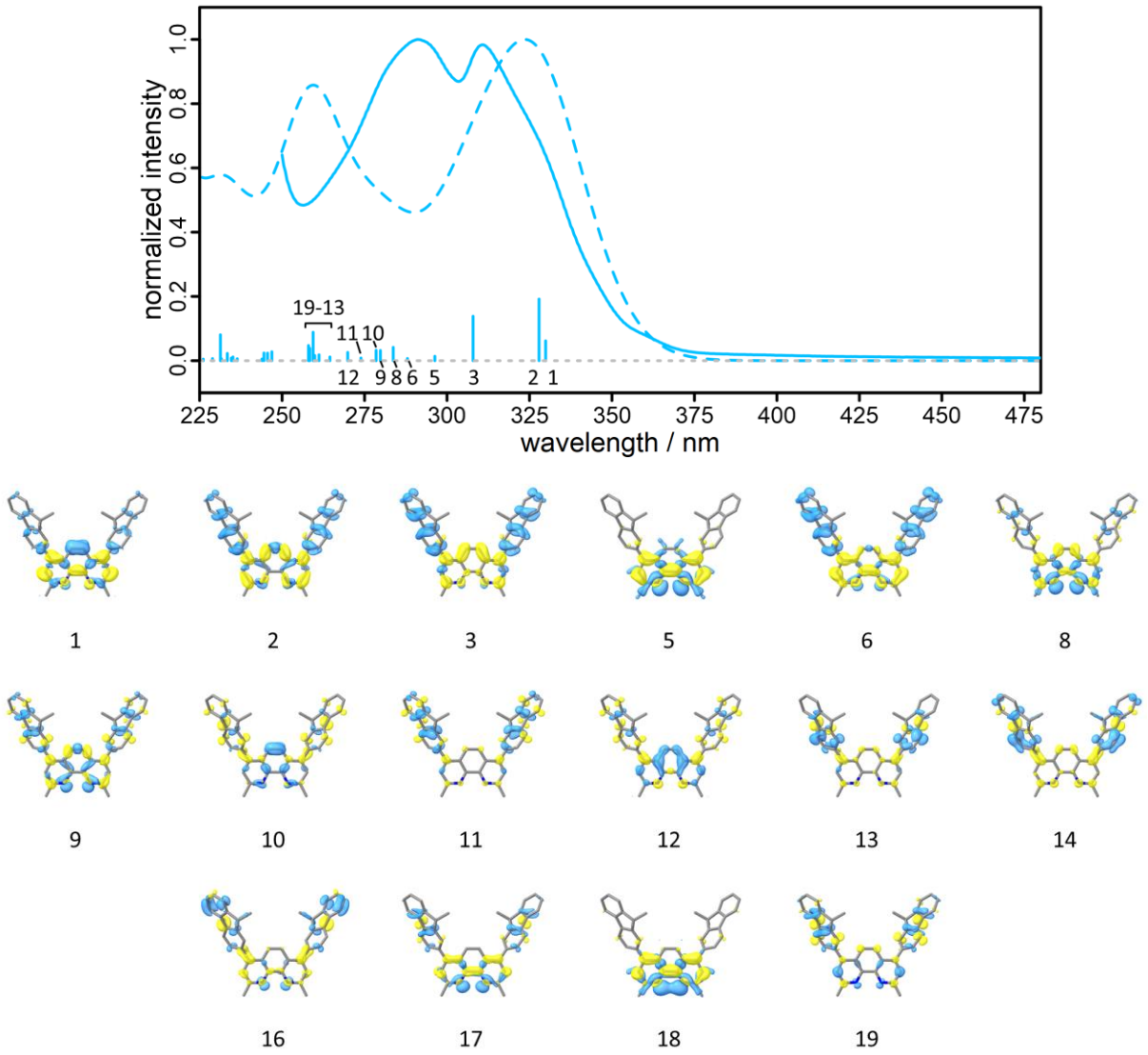

Figure S6.6. Normalized broadened calculated singlet excitation energies (dashed) with PBE0/def2-TZVP compared to the normalized experimental absorption spectrum (solid) of **nF** (top). Sticks are scaled down by a factor 0.25. Difference density plots corresponding to the excitation energies visualize the migration of electron density from cyan (-) to yellow (+) during the excitation (bottom).

Table S6.3. Excitation energies, oscillator strengths f_{osc} and corresponding transitions of **nF** obtained from TD-DFT with PBE0/def2-TZVP simulated in dichloromethane. Excitations with an oscillator strength > 0.01 and corresponding orbital contributions with an OC ≥ 0.15 are given.

State	Exc. energy		f_{osc}	Dominant contribution			Transition
#	cm^{-1}	nm		OC	#	cm^{-1}	nm
1	30307.9	329.9	0.247	0.832	HOMO	LUMO	$\pi_{neo,F} \rightarrow \pi_{neo}^*$
2	30500.9	327.9	0.767	0.170	HOMO-1	LUMO	$\pi_F \rightarrow \pi_{neo}^*$
				0.789	HOMO	LUMO+1	$\pi_{neo,F} \rightarrow \pi_{neo}^*$
3	32475.5	307.9	0.553	0.196	HOMO-2	LUMO	$\pi_{neo} \rightarrow \pi_{neo}^*$
				0.663	HOMO-1	LUMO+1	$\pi_F \rightarrow \pi_{neo}^*$
5	33755.2	296.3	0.055	0.709	HOMO-4	LUMO	$n_{neo} \rightarrow \pi_{neo}^*$
6	34719.3	288.0	0.027	0.452	HOMO-2	LUMO	$\pi_{neo} \rightarrow \pi_{neo}^*$
				0.213	HOMO-1	LUMO+1	$\pi_F \rightarrow \pi_{neo}^*$
8	35244.5	283.7	0.166	0.321	HOMO-4	LUMO+1	$n_{neo} \rightarrow \pi_{neo}^*$
				0.176	HOMO-3	LUMO	$\pi_{neo} \rightarrow \pi_{neo}^*$
9	35743.9	279.8	0.127	0.217	HOMO-2	LUMO+1	$\pi_{neo} \rightarrow \pi_{neo}^*$
				0.431	HOMO	LUMO+2	$\pi_{neo,F} \rightarrow \pi_{neo,F}^*$
10	35907.3	278.5	0.130	0.184	HOMO-3	LUMO+1	$\pi_{neo} \rightarrow \pi_{neo}^*$
				0.160	HOMO-2	LUMO	$\pi_{neo} \rightarrow \pi_{neo}^*$
				0.518	HOMO	LUMO+3	$\pi_{neo,F} \rightarrow \pi_{neo,F}^*$
11	36506	273.9	0.034	0.153	HOMO-3	LUMO+1	$\pi_{neo} \rightarrow \pi_{neo}^*$
				0.273	HOMO-1	LUMO+2	$\pi_F \rightarrow \pi_{neo,F}^*$
				0.165	HOMO	LUMO+4	$\pi_{neo,F} \rightarrow \pi_F^*$
12	37054.7	269.9	0.103	0.319	HOMO-3	LUMO	$\pi_{neo} \rightarrow \pi_{neo}^*$
				0.157	HOMO-1	LUMO+3	$\pi_F \rightarrow \pi_{neo,F}^*$
13	37808	264.5	0.046	0.150	HOMO-1	LUMO+3	$\pi_F \rightarrow \pi_{neo,F}^*$
14	38286.1	261.2	0.073	0.179	HOMO-5	LUMO	$\pi_F \rightarrow \pi_{neo}^*$
16	38472.9	259.9	0.064	0.242	HOMO-6	LUMO	$\pi_F \rightarrow \pi_{neo}^*$
				0.188	HOMO-5	LUMO+1	$\pi_F \rightarrow \pi_{neo}^*$
17	38547.2	259.4	0.354	0.168	HOMO-9	LUMO	$n_{neo} \rightarrow \pi_{neo}^*$
				0.341	HOMO-1	LUMO+3	$\pi_F \rightarrow \pi_{neo,F}^*$
18	38695	258.4	0.154	0.554	HOMO-9	LUMO	$n_{neo} \rightarrow \pi_{neo}^*$
19	38757.1	258.0	0.189	0.170	HOMO-3	LUMO+1	$\pi_{neo} \rightarrow \pi_{neo}^*$
				0.424	HOMO-1	LUMO+2	$\pi_F \rightarrow \pi_{neo,F}^*$
				0.193	HOMO	LUMO+3	$\pi_{neo,F} \rightarrow \pi_{neo,F}^*$

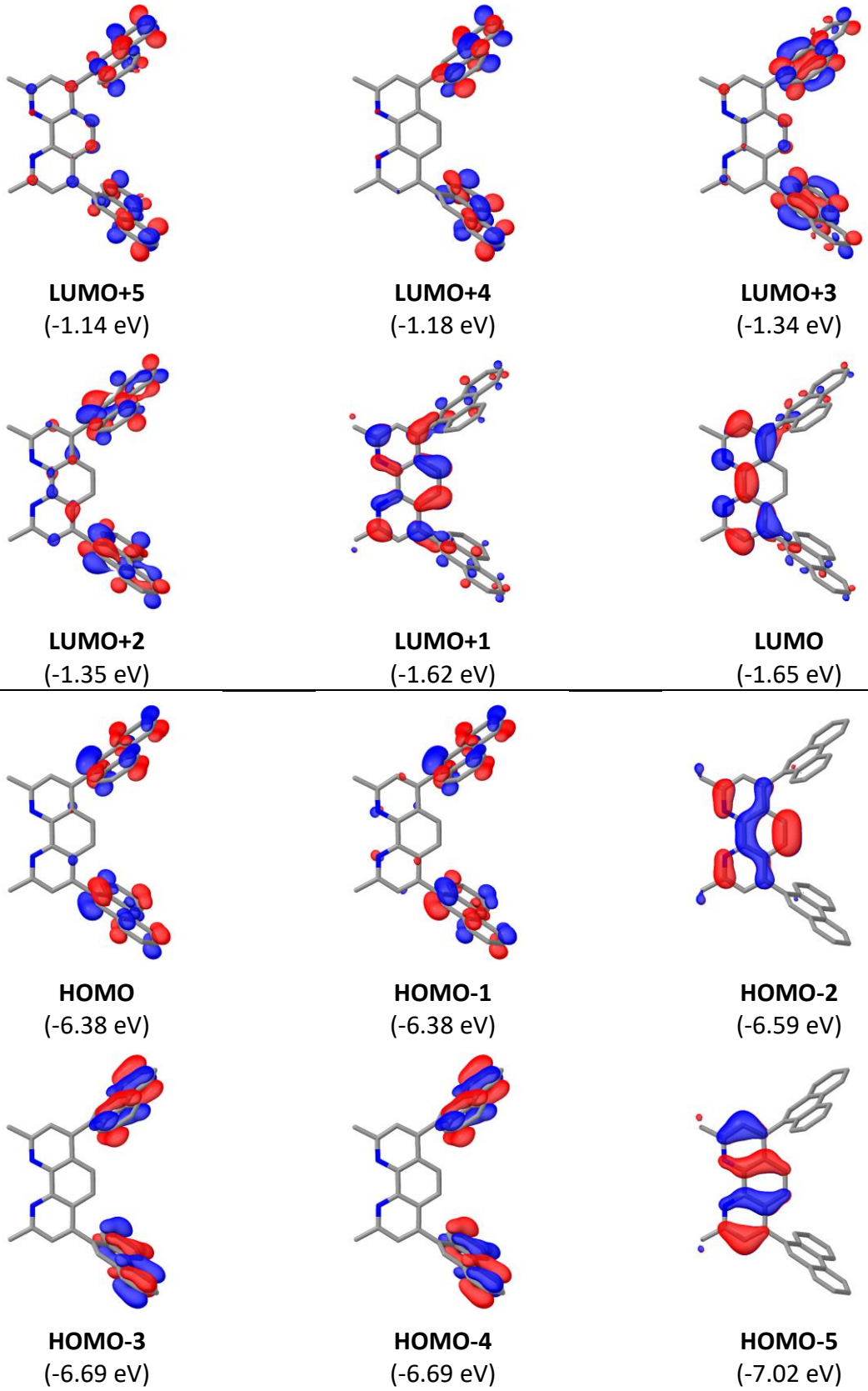

Figure S6.7. PBE0/def2-TZVP ground state frontier molecular orbitals of **nP** with respective energies in eV in parentheses. Positive lobes are depicted in red and negative in blue.

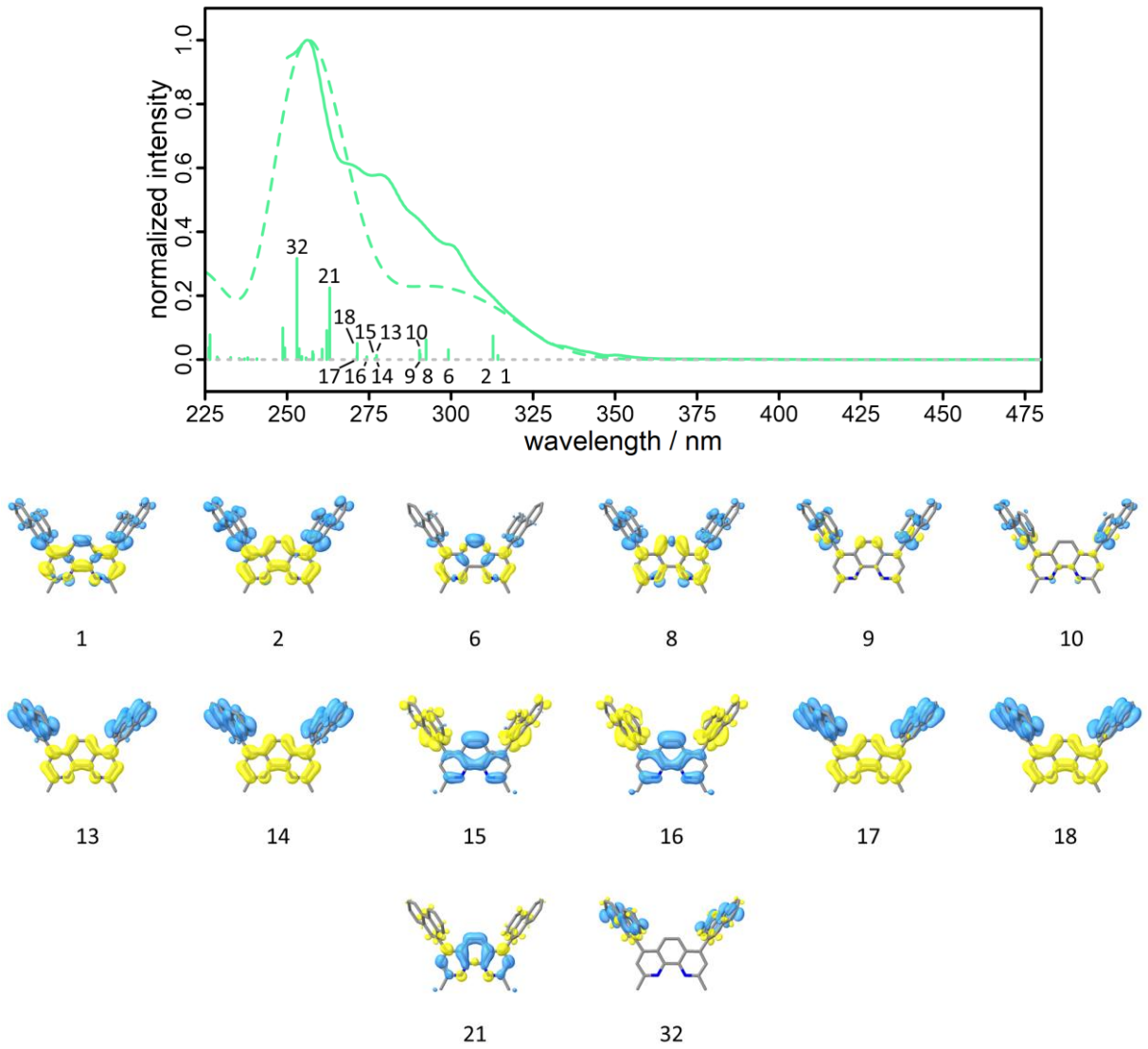

Figure S6.8. Normalized broadened calculated singlet excitation energies (dashed) with PBE0/def2-TZVP compared to the normalized experimental absorption spectrum (solid) of **nP** (top). Sticks are scaled down by a factor 0.25. Difference density plots corresponding to the excitation energies visualize the migration of electron density from cyan (-) to yellow (+) during the excitation (bottom).

Table S6.4. Excitation energies, oscillator strengths f_{osc} and corresponding transitions of **nP** obtained from TD-DFT with PBE0/def2-TZVP simulated in dichloromethane. Excitations with an oscillator strength > 0.01 and corresponding orbital contributions with an OC ≥ 0.15 are given.

State	Exc. energy		f_{osc}	Dominant contribution			Transition
#	cm^{-1}	nm		OC	occ. orb.	virt. orb.	
1	31816.7	314.3	0.052	0.190	HOMO-2	LUMO	$\pi_{neo} \rightarrow \pi_{neo}^*$
				0.465	HOMO-1	LUMO	$\pi_P \rightarrow \pi_{neo}^*$
				0.209	HOMO	LUMO+1	$\pi_P \rightarrow \pi_{neo}^*$
2	31970.2	312.8	0.296	0.460	HOMO-1	LUMO+1	$\pi_P \rightarrow \pi_{neo}^*$
				0.478	HOMO	LUMO	$\pi_P \rightarrow \pi_{neo}^*$
6	33419.6	299.2	0.124	0.419	HOMO-2	LUMO+1	$\pi_{neo} \rightarrow \pi_{neo}^*$
8	34203.7	292.4	0.248	0.325	HOMO-2	LUMO+1	$\pi_{neo} \rightarrow \pi_{neo}^*$
				0.162	HOMO-1	LUMO+1	$\pi_P \rightarrow \pi_{neo}^*$
9	34417.3	290.6	0.067	0.355	HOMO-1	LUMO+2	$\pi_P \rightarrow \pi_P^*$
				0.300	HOMO	LUMO+3	$\pi_P \rightarrow \pi_P^*$
10	34434.2	290.4	0.118	0.269	HOMO-1	LUMO+3	$\pi_P \rightarrow \pi_P^*$
				0.363	HOMO	LUMO+2	$\pi_P \rightarrow \pi_P^*$
13	36067.2	277.3	0.053	0.373	HOMO-4	LUMO+1	$\pi_P \rightarrow \pi_{neo}^*$
				0.326	HOMO-3	LUMO	$\pi_P \rightarrow \pi_{neo}^*$
14	36098	277.0	0.018	0.377	HOMO-4	LUMO	$\pi_P \rightarrow \pi_{neo}^*$
				0.361	HOMO-3	LUMO+1	$\pi_P \rightarrow \pi_{neo}^*$
15	36124.9	276.8	0.011	0.546	HOMO-2	LUMO+2	$\pi_{neo} \rightarrow \pi_P^*$
16	36460.9	274.3	0.036	0.624	HOMO-2	LUMO+3	$\pi_{neo} \rightarrow \pi_P^*$
17	36851.9	271.4	0.202	0.443	HOMO-4	LUMO	$\pi_P \rightarrow \pi_{neo}^*$
				0.433	HOMO-3	LUMO+1	$\pi_P \rightarrow \pi_{neo}^*$
18	36864.8	271.3	0.043	0.455	HOMO-4	LUMO+1	$\pi_P \rightarrow \pi_{neo}^*$
				0.436	HOMO-3	LUMO	$\pi_P \rightarrow \pi_{neo}^*$
21	38028.9	263.0	0.898	0.553	HOMO-5	LUMO	$\pi_{neo} \rightarrow \pi_{neo}^*$
				0.178	HOMO-2	LUMO+3	$\pi_{neo} \rightarrow \pi_P^*$
32	39531.6	253.0	1.267	0.153	HOMO-4	LUMO+2	$\pi_P \rightarrow \pi_P^*$
				0.247	HOMO-4	LUMO+4	$\pi_P \rightarrow \pi_P^*$
				0.239	HOMO-3	LUMO+3	$\pi_P \rightarrow \pi_P^*$
				0.183	HOMO-3	LUMO+5	$\pi_P \rightarrow \pi_P^*$

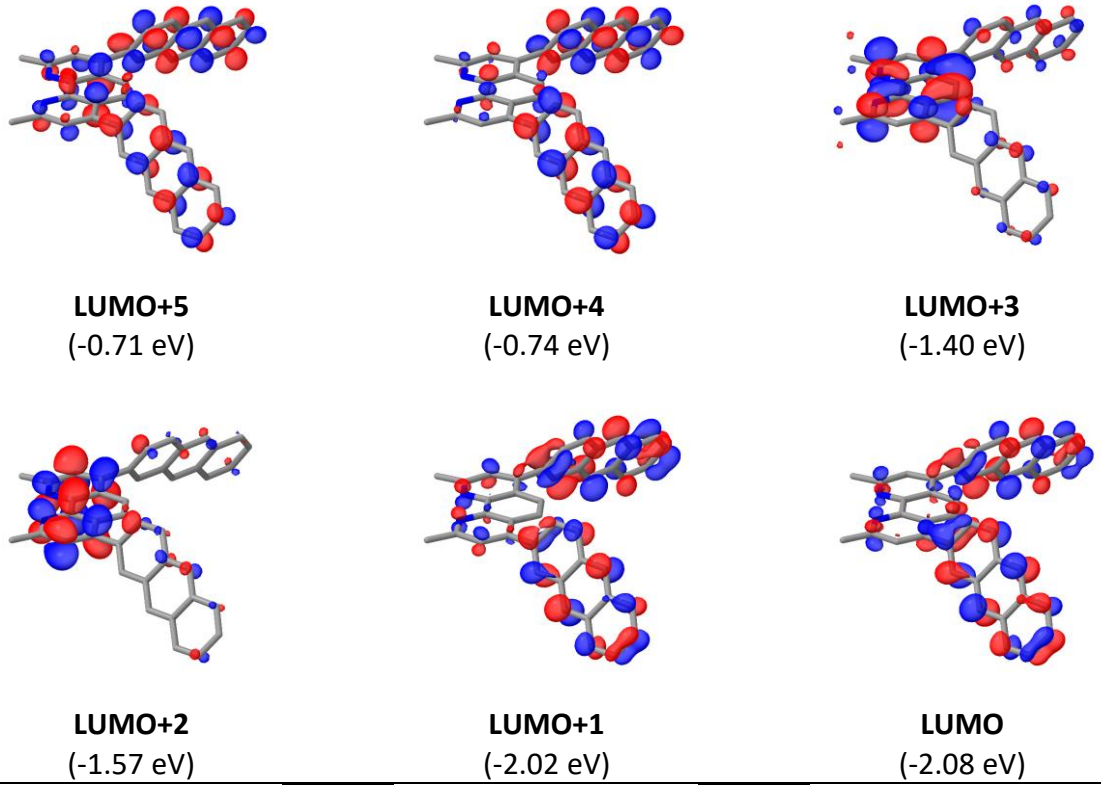

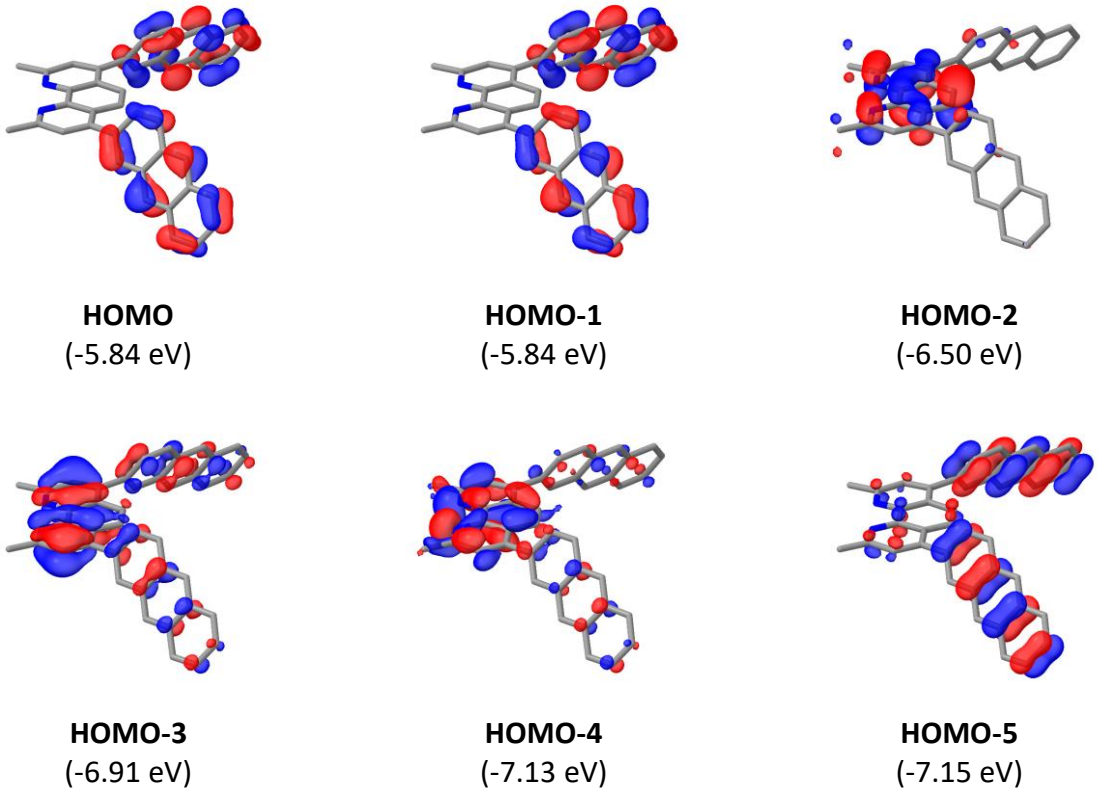

Figure S6.9. PBE0/def2-TZVP ground state frontier molecular orbitals of **nA** with respective energies in eV in parentheses. Positive lobes are depicted in red and negative in blue.

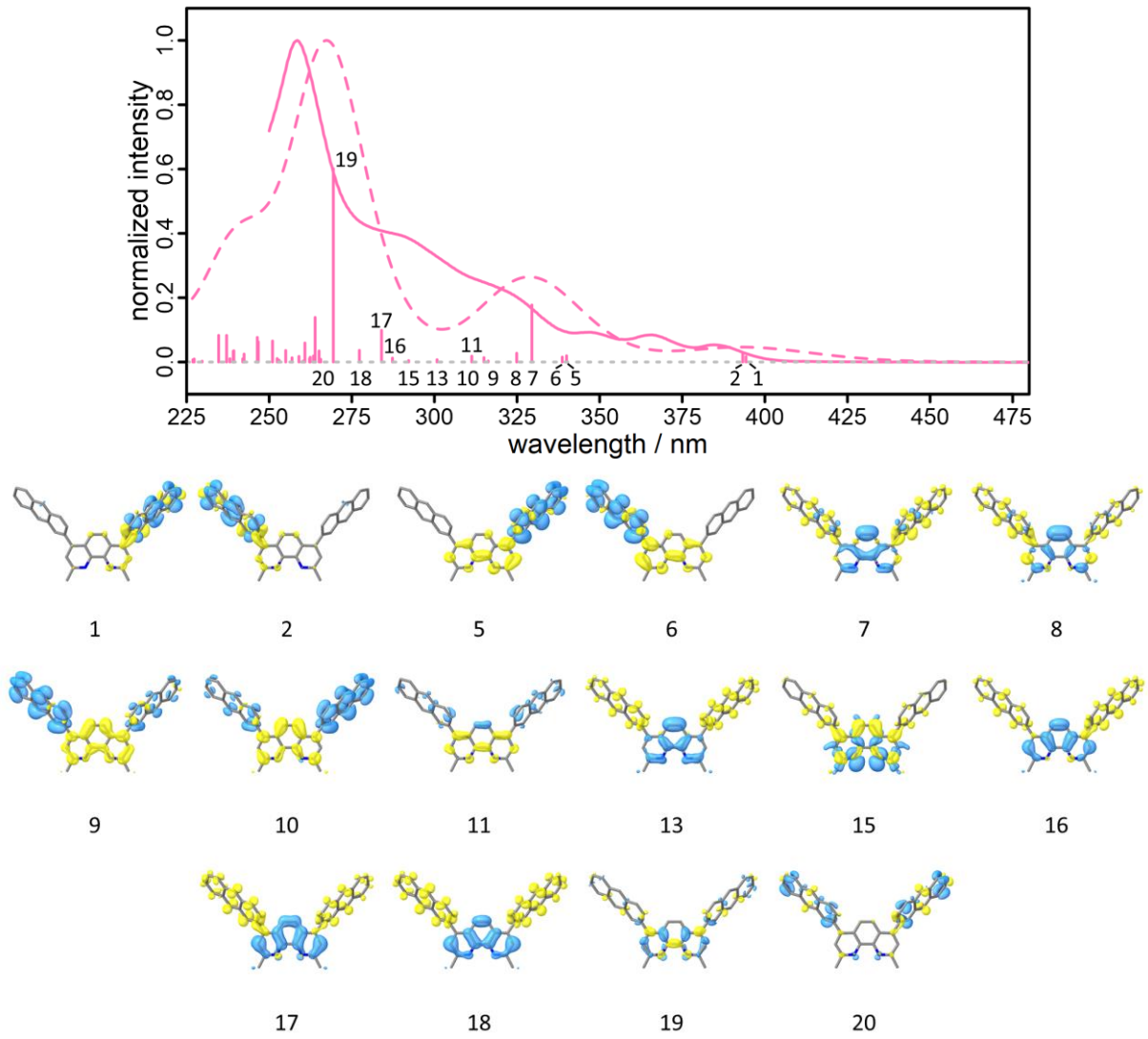

Figure S6.10. Normalized broadened calculated singlet excitation energies (dashed) with PBE0/def2-TZVP compared to the normalized experimental absorption spectrum (solid) of **nA** (top). Sticks are scaled down by a factor 0.25. Difference density plots corresponding to the excitation energies visualize the migration of electron density from cyan (-) to yellow (+) during the excitation (bottom).

Table S6.5. Excitation energies, oscillator strengths f_{osc} and corresponding transitions of **nA** obtained from TD-DFT with PBE0/def2-TZVP simulated in dichloromethane. Excitations with an oscillator strength > 0.01 and corresponding orbital contributions with an OC ≥ 0.15 are given.

State	Exc. energy		f_{osc}	Dominant contribution			Transition
#	cm^{-1}	nm		OC	occ. orb.	virt. orb.	
1	25363	394.3	0.067	0.317	HOMO-1	LUMO+1	$\pi_A \rightarrow \pi_A^*$
				0.556	HOMO	LUMO	$\pi_A \rightarrow \pi_A^*$
2	25424	393.3	0.104	0.512	HOMO-1	LUMO	$\pi_A \rightarrow \pi_A^*$
				0.357	HOMO	LUMO+1	$\pi_A \rightarrow \pi_A^*$
5	29414.3	340.0	0.078	0.295	HOMO-1	LUMO+2	$\pi_A \rightarrow \pi_{neo}^*$
				0.381	HOMO	LUMO+2	$\pi_A \rightarrow \pi_{neo}^*$
6	29524.2	338.7	0.062	0.349	HOMO-1	LUMO+2	$\pi_A \rightarrow \pi_{neo}^*$
				0.292	HOMO	LUMO+2	$\pi_A \rightarrow \pi_{neo}^*$
7	30346.1	329.5	0.709	0.786	HOMO-2	LUMO	$\pi_{neo} \rightarrow \pi_A^*$
8	30774	324.9	0.110	0.639	HOMO-2	LUMO+1	$\pi_{neo} \rightarrow \pi_A^*$
9	31617.9	316.3	0.013	0.241	HOMO-1	LUMO+2	$\pi_A \rightarrow \pi_{neo}^*$
				0.642	HOMO	LUMO+3	$\pi_A \rightarrow \pi_{neo}^*$
10	31747.8	315.0	0.055	0.766	HOMO-1	LUMO+3	$\pi_A \rightarrow \pi_{neo}^*$
11	32128.1	311.3	0.073	0.270	HOMO-3	LUMO	$\pi_{neo} \rightarrow \pi_A^*$
				0.164	HOMO-2	LUMO+2	$\pi_{neo} \rightarrow \pi_{neo}^*$
				0.151	HOMO	LUMO+2	$\pi_A \rightarrow \pi_{neo}^*$
13	33248.1	300.8	0.029	0.234	HOMO-2	LUMO+1	$\pi_{neo} \rightarrow \pi_A^*$
				0.344	HOMO-2	LUMO+2	$\pi_{neo} \rightarrow \pi_{neo}^*$
15	34217.8	292.2	0.018	0.307	HOMO-6	LUMO	$n_{neo} \rightarrow \pi_A^*$
				0.221	HOMO-4	LUMO	$n_{neo} \rightarrow \pi_A^*$
16	34810.9	287.3	0.049	0.339	HOMO-3	LUMO+1	$\pi_{neo} \rightarrow \pi_A^*$
				0.371	HOMO-2	LUMO+3	$\pi_{neo} \rightarrow \pi_{neo}^*$
17	35208	284	0.394	0.493	HOMO-3	LUMO	$\pi_{neo} \rightarrow \pi_A^*$
				0.233	HOMO-2	LUMO+2	$\pi_{neo} \rightarrow \pi_{neo}^*$
18	36056.1	277.3	0.146	0.301	HOMO-3	LUMO+1	$\pi_{neo} \rightarrow \pi_A^*$
				0.375	HOMO-2	LUMO+3	$\pi_{neo} \rightarrow \pi_{neo}^*$
19	37117.3	269.4	2.404	0.199	HOMO-3	LUMO+2	$\pi_{neo} \rightarrow \pi_{neo}^*$
				0.194	HOMO	LUMO+4	$\pi_A \rightarrow \pi_A^*$
20	37656.5	265.6	0.034	0.211	HOMO-8	LUMO+1	$\pi_A \rightarrow \pi_A^*$
				0.303	HOMO-7	LUMO	$\pi_A \rightarrow \pi_A^*$

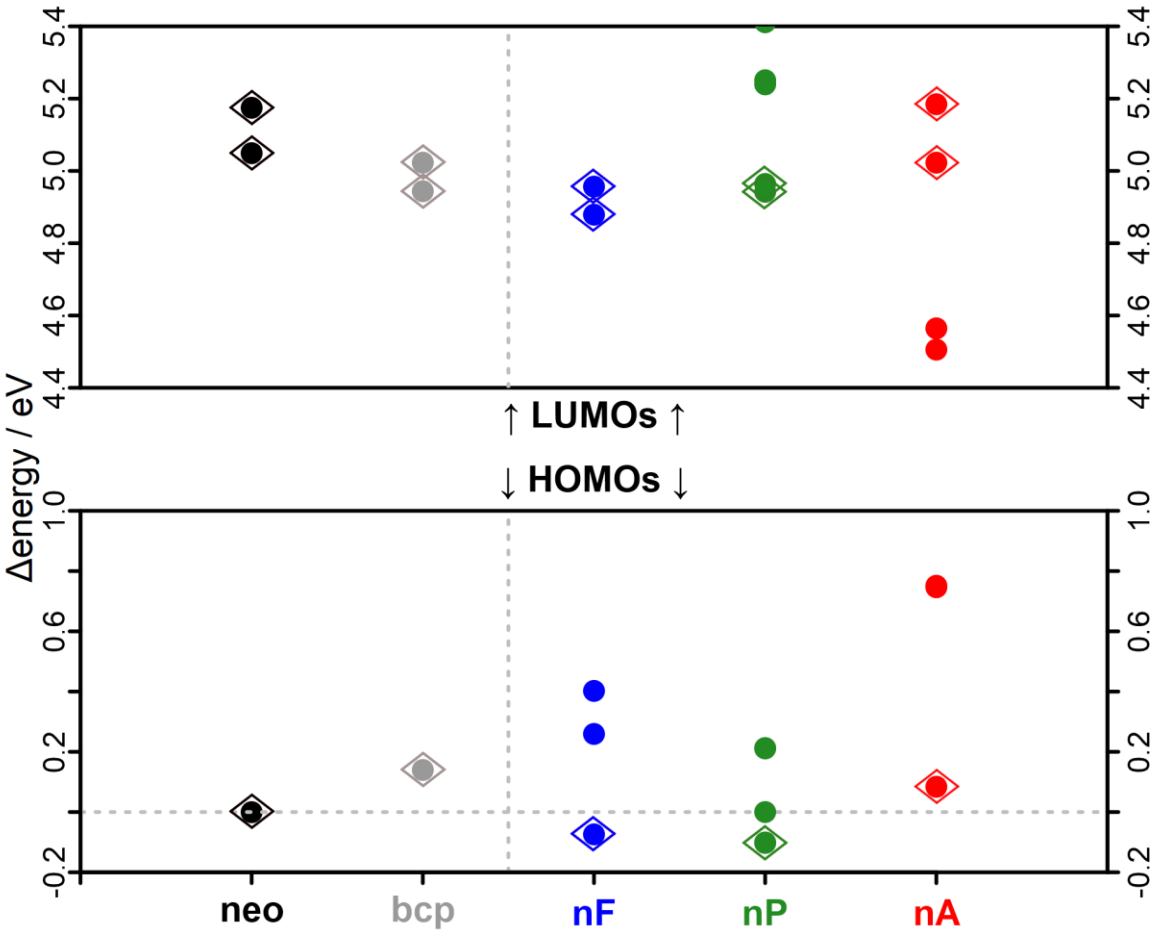

Figure S6.11. Energy diagram of the frontier orbitals of the free ligands with PBE0/def2-TZVP. Orbitals marked with diamonds are attributed to **neo** whereas those unmarked are attributed to the substituents. The energy of the **neo** HOMO orbital has been set to 0 eV (-6.59 eV) for reference.

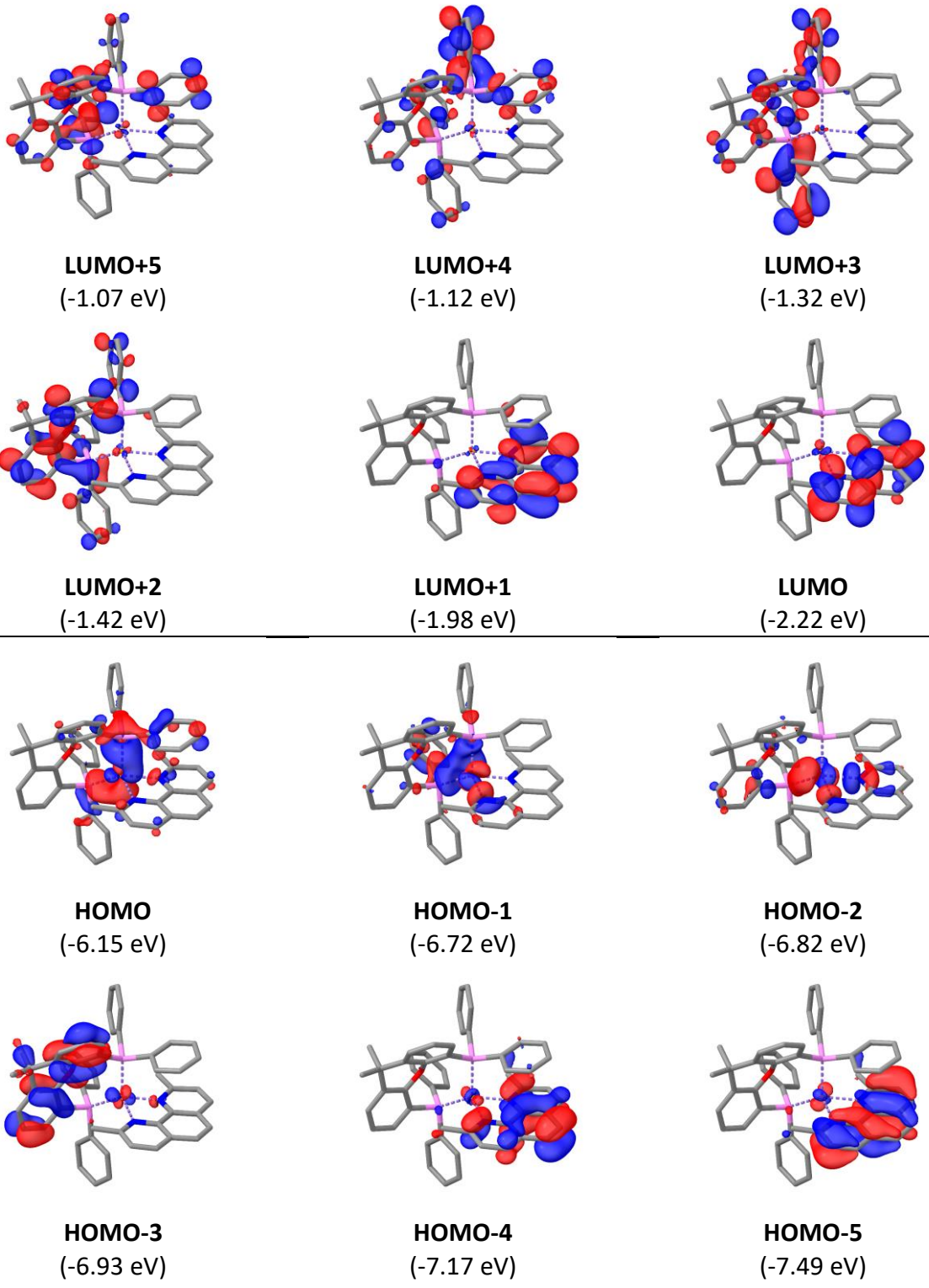

Figure S6.12. PBE0/def2-TZVP ground state frontier molecular orbitals of **Cuneo** with respective energies in eV in parentheses. Positive lobes are depicted in red and negative in blue.

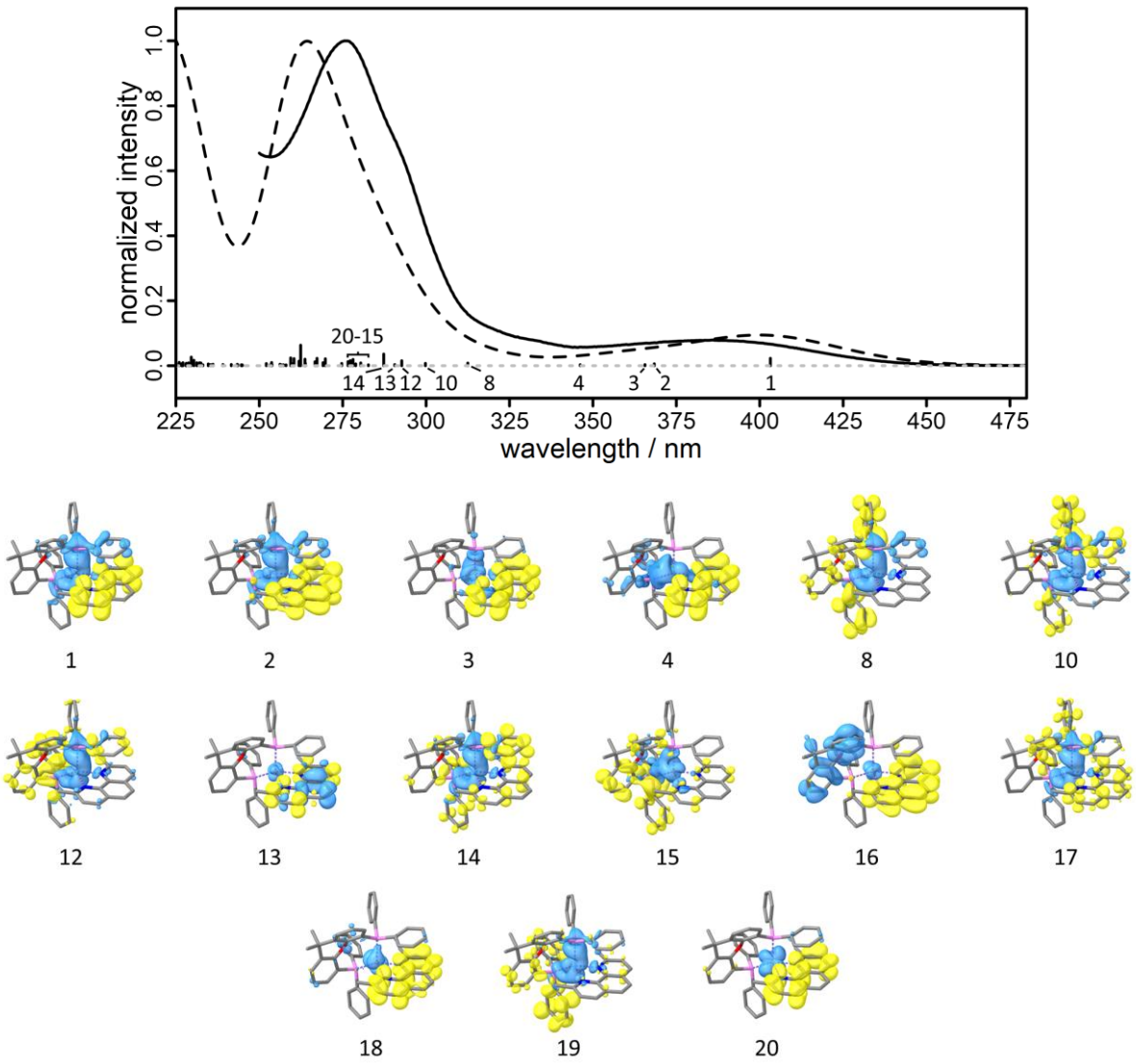

Figure S6.13. Normalized broadened calculated singlet excitation energies (dashed) with PBE0/def2-TZVP compared to the normalized experimental absorption spectrum (solid) of **Cuneo** (top). Sticks are scaled down by a factor of 0.25. Difference density plots corresponding to the excitation energies visualize the migration of electron density from cyan (-) to yellow (+) during the excitation (bottom).

Table S6.6. Excitation energies, oscillator strengths f_{osc} and corresponding transitions of **Cuneo** obtained from TD-DFT with PBE0/def2-TZVP simulated in dichloromethane. Excitations with an oscillator strength > 0.01 and corresponding orbital contributions with an OC ≥ 0.15 are given. Phenyl rings and xantphos are abbreviated as x and Ph.

State	Exc. energy		f_{osc}	Dominant contribution			Transition
#	cm^{-1}	nm		OC	occ. orb.	virt. orb.	
1	24801.9	403.2	0.091	0.959	HOMO	LUMO	$d_{Cu} \rightarrow \pi_{neo}^*$
2	27147.6	368.4	0.024	0.818	HOMO	LUMO+1	$d_{Cu} \rightarrow \pi_{neo}^*$
3	27350.9	365.6	0.013	0.412	HOMO-2	LUMO	$d_{Cu} \rightarrow \pi_{neo}^*$
				0.406	HOMO-1	LUMO	$d_{Cu} \rightarrow \pi_{neo}^*$
4	28889.1	346.2	0.012	0.397	HOMO-2	LUMO	$d_{Cu} \rightarrow \pi_{neo}^*$
				0.490	HOMO-1	LUMO	$d_{Cu} \rightarrow \pi_{neo}^*$
8	32000.6	312.5	0.033	0.899	HOMO	LUMO+3	$d_{Cu} \rightarrow \pi_x^*, \pi_{Ph,x}^*$
10	33354.7	299.8	0.029	0.823	HOMO	LUMO+4	$d_{Cu} \rightarrow \pi_x^*, \pi_{Ph,x}^*$
12	34159.7	292.7	0.061	0.824	HOMO	LUMO+5	$d_{Cu} \rightarrow \pi_x^*, \pi_{Ph,x}^*$
13	34416.7	290.6	0.014	0.388	HOMO-5	LUMO	$\pi_{neo} \rightarrow \pi_{neo}^*$
				0.491	HOMO-4	LUMO+1	$\pi_{neo} \rightarrow \pi_{neo}^*$
14	34800.9	287.3	0.143	0.886	HOMO	LUMO+6	$d_{Cu} \rightarrow \pi_{Ph,x}^*, \pi_{neo}^*$
15	35368.1	282.7	0.011	0.610	HOMO-1	LUMO+2	$d_{Cu} \rightarrow \pi_x^*, \pi_{Ph,x}^*$
16	35662.9	280.4	0.035	0.741	HOMO-3	LUMO+1	$\pi_x \rightarrow \pi_{neo}^*$
17	35854.4	278.9	0.023	0.714	HOMO	LUMO+8	$d_{Cu} \rightarrow \pi_{Ph,x}^*, \pi_{neo}^*$
18	35964.0	278.1	0.077	0.231	HOMO-14	LUMO	$d_{Cu}, \pi_{Ph} \rightarrow \pi_{neo}^*$
19	36056.3	277.3	0.063	0.161	HOMO-2	LUMO+2	$d_{Cu} \rightarrow \pi_x^*, \pi_{Ph,x}^*$
				0.536	HOMO	LUMO+7	$d_{Cu} \rightarrow \pi_{Ph,x}^*$
20	36153.2	276.6	0.051	0.202	HOMO-15	LUMO	$d_{Cu}, \pi_{Ph} \rightarrow \pi_{neo}^*$
				0.165	HOMO-12	LUMO	$d_{Cu}, \pi_{Ph} \rightarrow \pi_{neo}^*$

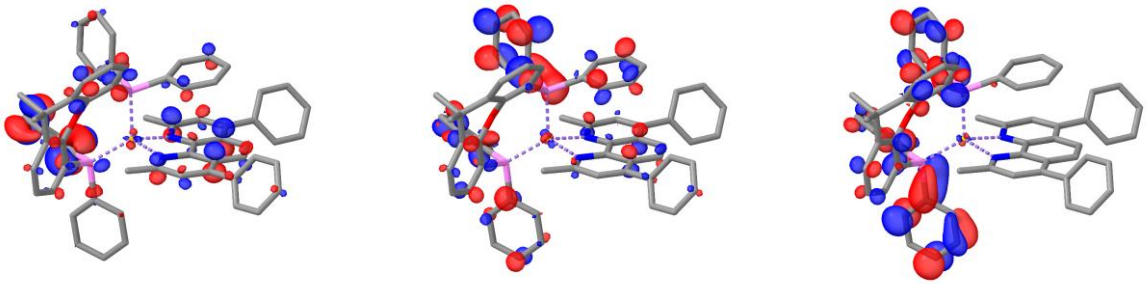

LUMO+5
(-1.07 eV)

LUMO+4
(-1.12 eV)

LUMO+3
(-1.32 eV)

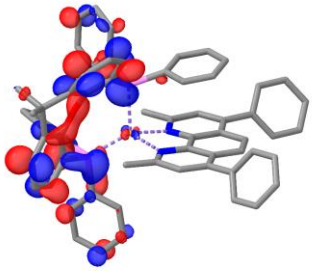

LUMO+2
(-1.42 eV)

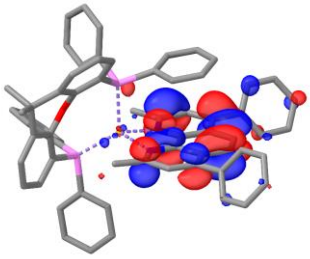

LUMO+1
(-2.07 eV)

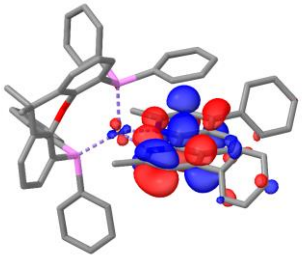

LUMO
(-2.26 eV)

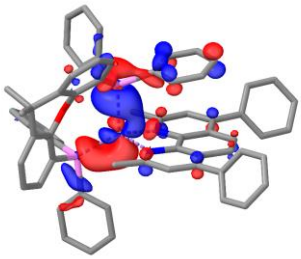

HOMO
(-6.11 eV)

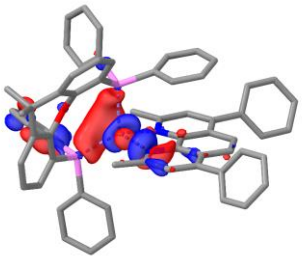

HOMO-1
(-6.67 eV)

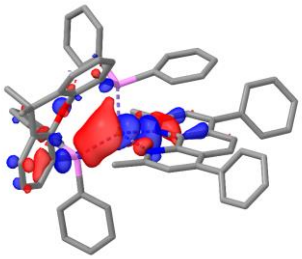

HOMO-2
(-6.78 eV)

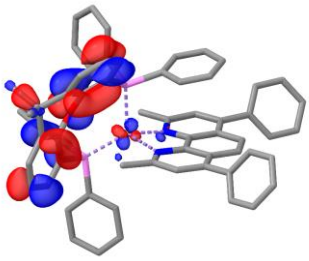

HOMO-3
(-6.92 eV)

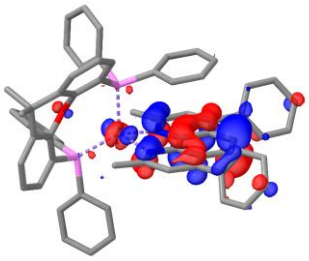

HOMO-4
(-7.02 eV)

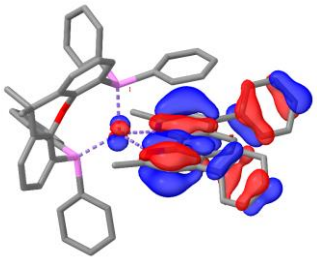

HOMO-5
(-7.36 eV)

Figure S6.14. PBE0/def2-TZVP ground state frontier molecular orbitals of **Cubcp** with respective energies in eV in parentheses. Positive lobes are depicted in red and negative in blue.

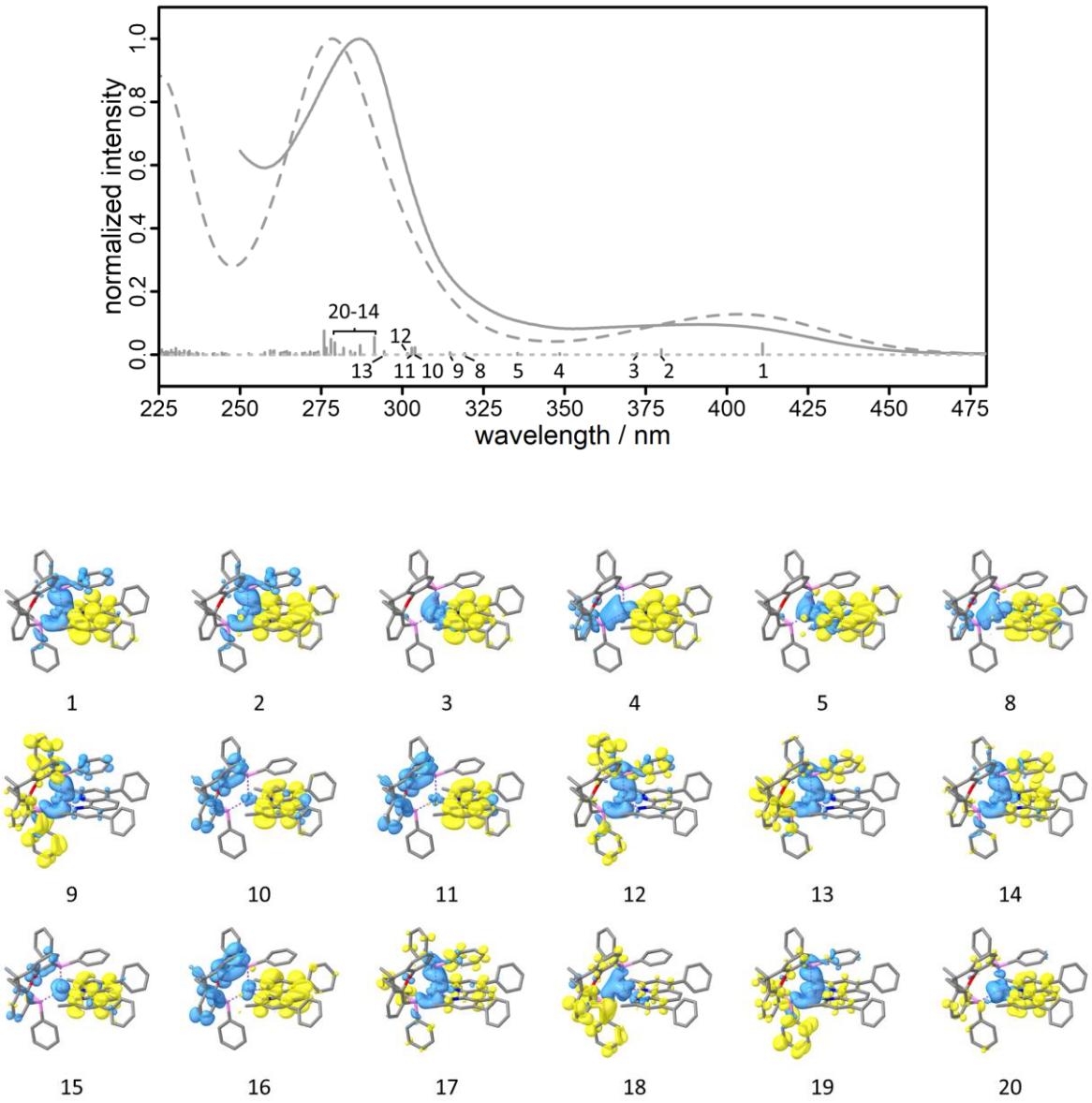

Figure S6.15. Normalized broadened calculated singlet excitation energies (dashed) with PBE0/def2-TZVP compared to the normalized experimental absorption spectrum (solid) of **Cubcp** (top). Sticks have been scaled down by a factor of 0.25. Difference density plots corresponding to the excitation energies visualize the migration of electron density from cyan (-) to yellow (+) during the excitation (bottom).

Table S6.7. Excitation energies, oscillator strengths f_{osc} and corresponding transitions of **Cubcp** obtained from TD-DFT with PBE0/def2-TZVP simulated in dichloromethane. Excitations with an oscillator strength > 0.01 and corresponding orbital contributions with an OC ≥ 0.15 are given. Phenyl rings and xantphos are abbreviated as x and Ph.

State	Exc. energy		f_{osc}	Dominant contribution			Transition
#	cm^{-1}	nm		OC	occ. orb.	virt. orb.	
1	24333.4	411.0	0.140	0.958	HOMO	LUMO	$d_{Cu} \rightarrow \pi_{neo}^*$
2	26331.0	379.8	0.066	0.936	HOMO	LUMO+1	$d_{Cu} \rightarrow \pi_{neo}^*$
3	26858.0	372.3	0.017	0.268	HOMO-2	LUMO	$d_{Cu} \rightarrow \pi_{neo}^*$
				0.650	HOMO-1	LUMO	$d_{Cu} \rightarrow \pi_{neo}^*$
4	28690.4	348.5	0.017	0.598	HOMO-2	LUMO	$d_{Cu} \rightarrow \pi_{neo}^*$
				0.283	HOMO-1	LUMO	$d_{Cu} \rightarrow \pi_{neo}^*$
5	29802.7	335.5	0.020	0.291	HOMO-2	LUMO+1	$d_{Cu} \rightarrow \pi_{neo}^*$
				0.641	HOMO-1	LUMO+1	$d_{Cu} \rightarrow \pi_{neo}^*$
8	31329.1	319.2	0.017	0.290	HOMO-4	LUMO	$\pi_{neo} \rightarrow \pi_{neo}^*$
				0.389	HOMO-2	LUMO+1	$d_{Cu} \rightarrow \pi_{neo}^*$
				0.180	HOMO-1	LUMO+1	$d_{Cu} \rightarrow \pi_{neo}^*$
9	31776.4	314.7	0.027	0.924	HOMO	LUMO+3	$d_{Cu} \rightarrow \pi_x^*, \pi_{Ph,x}^*$
10	32904.2	303.9	0.091	0.419	HOMO-4	LUMO+1	$\pi_{neo} \rightarrow \pi_{neo}^*$
				0.362	HOMO-3	LUMO	$\pi_x \rightarrow \pi_{neo}^*$
11	33012.8	302.9	0.086	0.331	HOMO-4	LUMO+1	$\pi_{neo} \rightarrow \pi_{neo}^*$
				0.492	HOMO-3	LUMO	$\pi_x \rightarrow \pi_{neo}^*$
12	33158.2	301.6	0.017	0.826	HOMO	LUMO+4	$d_{Cu} \rightarrow \pi_x^*, \pi_{Ph,x}^*$
13	33963.0	294.4	0.042	0.642	HOMO	LUMO+5	$d_{Cu} \rightarrow \pi_x^*, \pi_{Ph,x}^*$
				0.198	HOMO	LUMO+6	$d_{Cu} \rightarrow \pi_{neo}^*, \pi_{Ph,x}^*$
14	34321.8	291.4	0.221	0.219	HOMO	LUMO+5	$d_{Cu} \rightarrow \pi_x^*, \pi_{Ph,x}^*$
				0.649	HOMO	LUMO+6	$d_{Cu} \rightarrow \pi_{neo}^*, \pi_{Ph,x}^*$
15	34843.6	287.0	0.119	0.378	HOMO-5	LUMO	$\pi_{neo}, \pi_{Ph,neo} \rightarrow \pi_{neo}^*$
				0.227	HOMO-3	LUMO+1	$\pi_x \rightarrow \pi_{neo}^*$
16	35034.8	285.4	0.023	0.587	HOMO-3	LUMO+1	$\pi_x \rightarrow \pi_{neo}^*$
17	35208.8	284.0	0.045	0.538	HOMO	LUMO+7	$d_{Cu} \rightarrow \pi_{neo}^*, \pi_{Ph,bcp,x}^*$
18	35476.0	281.9	0.085	0.552	HOMO-1	LUMO+2	$d_{Cu} \rightarrow \pi_x^*, \pi_{Ph,x}^*$
19	35798.3	279.3	0.017	0.161	HOMO	LUMO+7	$d_{Cu} \rightarrow \pi_{neo}^*, \pi_{Ph,bcp,x}^*$
				0.270	HOMO	LUMO+8	$d_{Cu} \rightarrow \pi_{neo}^*, \pi_{Ph,bcp,x}^*$
				0.179	HOMO	LUMO+9	$d_{Cu} \rightarrow \pi_{neo}^*, \pi_{Ph,bcp,x}^*$
20	35810.8	279.2	0.153	0.155	HOMO-18	LUMO	$d_{Cu}, \pi_{Ph,x} \rightarrow \pi_{neo}^*$
				0.156	HOMO-2	LUMO+2	$d_{Cu} \rightarrow \pi_x^*, \pi_{Ph,x}^*$

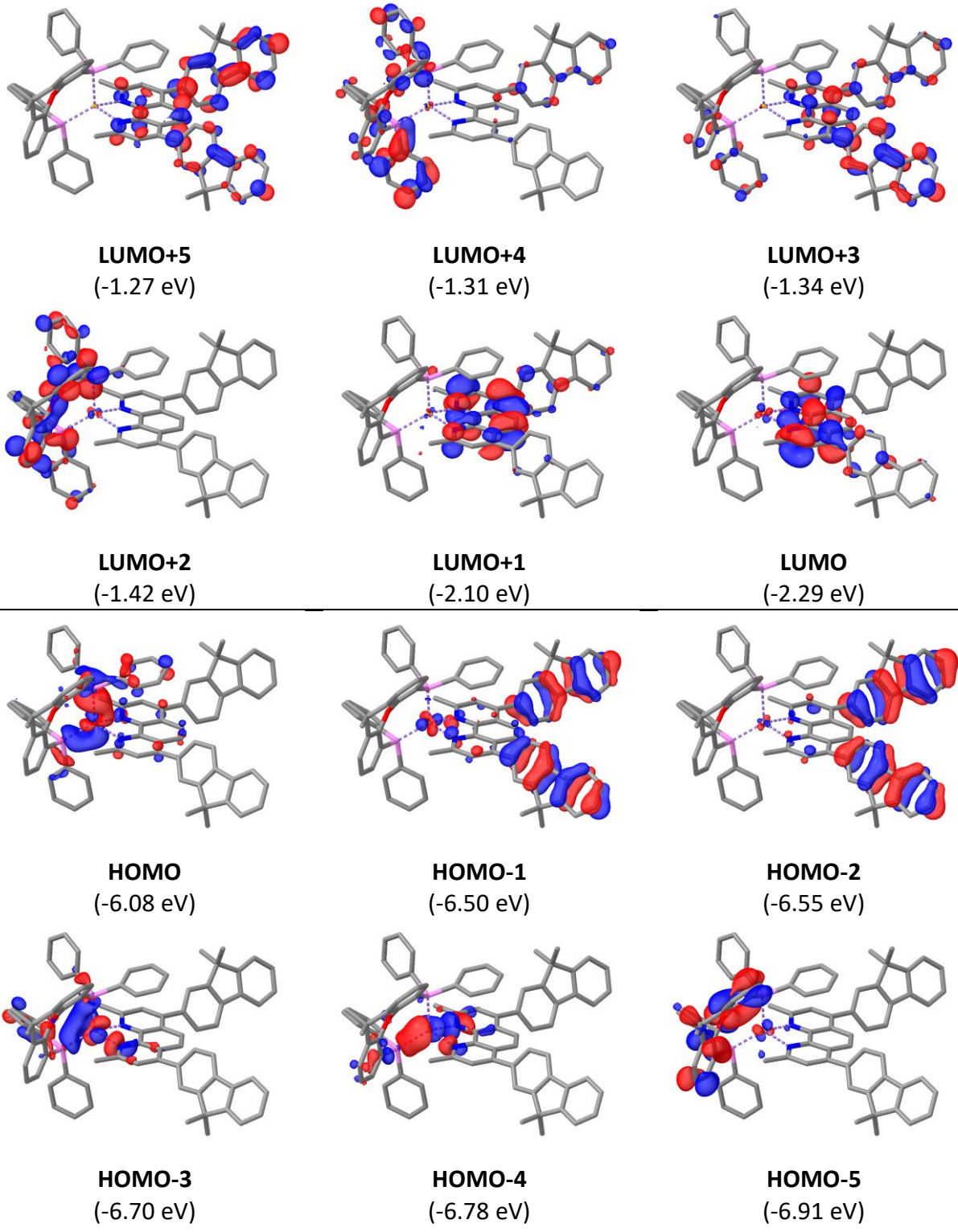

Figure S6.16. PBE0/def2-TZVP ground state frontier molecular orbitals of **CunF** with respective energies in eV in parentheses. Positive lobes are depicted in red and negative in blue.

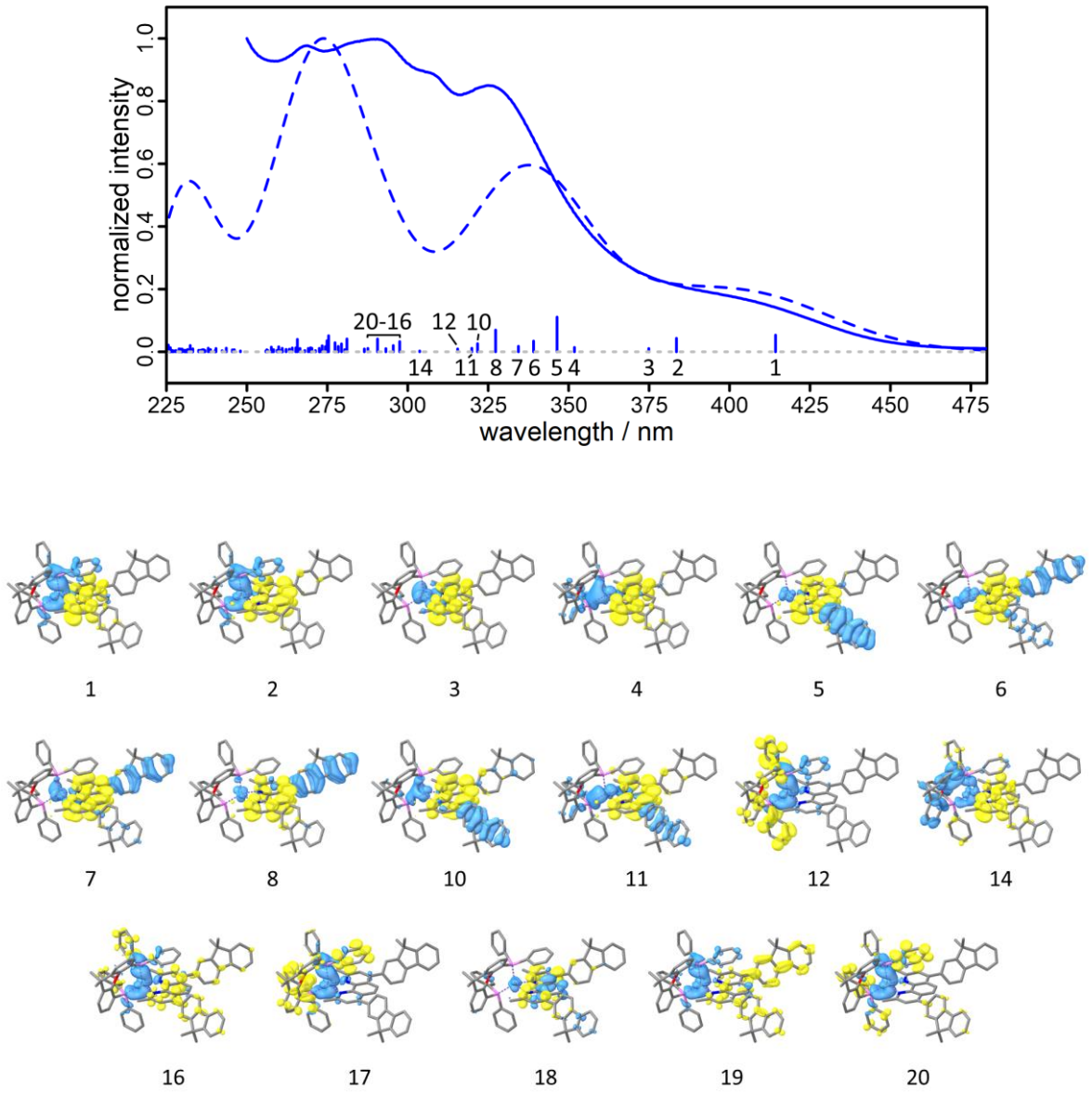

Figure S6.17. Normalized broadened calculated singlet excitation energies (dashed) with PBE0/def2-TZVP compared to the normalized experimental absorption spectrum (solid) of **CunF** (top). Sticks are scaled down by a factor of 0.25. Difference density plots corresponding to the excitation energies visualize the migration of electron density from cyan (-) to yellow (+) during the excitation (bottom).

Table S6.8. Excitation energies, oscillator strengths f_{osc} and corresponding transitions of **CunF** obtained from TD-DFT with PBE0/def2-TZVP simulated in dichloromethane. Excitations with an oscillator strength > 0.01 and corresponding orbital contributions with an OC ≥ 0.15 are given. Phenyl rings and xantphos are abbreviated as x and Ph.

State	Exc. energy		f_{osc}	Dominant contribution			Transition
#	cm^{-1}	nm		OC	occ. orb.	virt. orb.	
1	24139.3	414.3	0.213	0.948	HOMO	LUMO	$d_{Cu} \rightarrow \pi_{neo}^*$
2	26073.9	383.5	0.172	0.910	HOMO	LUMO+1	$d_{Cu} \rightarrow \pi_{neo}^*$
3	26671.4	374.9	0.042	0.381	HOMO-4	LUMO	$d_{Cu} \rightarrow \pi_{neo}^*$
				0.322	HOMO-3	LUMO	$d_{Cu} \rightarrow \pi_{neo}^*$
				0.197	HOMO-1	LUMO	$\pi_F \rightarrow \pi_{neo}^*$
4	28426.6	351.8	0.056	0.216	HOMO-4	LUMO	$d_{Cu} \rightarrow \pi_{neo}^*$
				0.562	HOMO-3	LUMO	$d_{Cu} \rightarrow \pi_{neo}^*$
5	28866.2	346.4	0.443	0.222	HOMO-2	LUMO	$\pi_F \rightarrow \pi_{neo}^*$
				0.241	HOMO-1	LUMO	$\pi_F \rightarrow \pi_{neo}^*$
				0.340	HOMO-1	LUMO+1	$\pi_F \rightarrow \pi_{neo}^*$
6	29491.8	339.1	0.137	0.276	HOMO-4	LUMO	$d_{Cu} \rightarrow \pi_{neo}^*$
				0.362	HOMO-1	LUMO	$\pi_F \rightarrow \pi_{neo}^*$
				0.177	HOMO-1	LUMO+1	$\pi_F \rightarrow \pi_{neo}^*$
7	29900.2	334.4	0.070	0.229	HOMO-4	LUMO+1	$d_{Cu} \rightarrow \pi_{neo}^*$
				0.232	HOMO-3	LUMO+1	$d_{Cu} \rightarrow \pi_{neo}^*$
				0.413	HOMO-2	LUMO	$\pi_F \rightarrow \pi_{neo}^*$
8	30557.0	327.3	0.278	0.192	HOMO-2	LUMO	$\pi_F \rightarrow \pi_{neo}^*$
				0.399	HOMO-2	LUMO+1	$\pi_F \rightarrow \pi_{neo}^*$
10	31080.4	321.7	0.104	0.402	HOMO-3	LUMO+1	$d_{Cu} \rightarrow \pi_{neo}^*$
				0.297	HOMO-2	LUMO+1	$\pi_F \rightarrow \pi_{neo}^*$
11	31260.2	319.9	0.045	0.516	HOMO-4	LUMO+1	$d_{Cu} \rightarrow \pi_{neo}^*$
				0.165	HOMO-1	LUMO+1	$\pi_F \rightarrow \pi_{neo}^*$
12	31699.1	315.5	0.036	0.254	HOMO	LUMO+3	$d_{Cu} \rightarrow \pi_{neo}^*, \pi_F^*$
				0.621	HOMO	LUMO+4	$d_{Cu} \rightarrow \pi_x^*, \pi_{Ph,x}^*$
14	32928.6	303.7	0.011	0.366	HOMO-5	LUMO	$\pi_x \rightarrow \pi_{neo}^*$
16	33615.3	297.5	0.131	0.383	HOMO	LUMO+3	$d_{Cu} \rightarrow \pi_{neo}^*, \pi_F^*$
				0.224	HOMO	LUMO+6	$d_{Cu} \rightarrow \pi_x^*, \pi_{Ph,x}^*$
17	33843.6	295.5	0.080	0.155	HOMO	LUMO+6	$d_{Cu} \rightarrow \pi_x^*, \pi_{Ph,x}^*$
				0.712	HOMO	LUMO+7	$d_{Cu} \rightarrow \pi_x^*, \pi_{Ph,x}^*$
18	34108.5	293.2	0.041	0.267	HOMO-9	LUMO	$\pi_{neo} \rightarrow \pi_{neo}^*$
				0.383	HOMO-6	LUMO+1	$\pi_{neo} \rightarrow \pi_{neo}^*$
19	34410.7	290.6	0.163	0.676	HOMO	LUMO+5	$d_{Cu} \rightarrow \pi_{neo}^*, \pi_F^*$
20	34769.6	287.6	0.043	0.638	HOMO	LUMO+8	$d_{Cu} \rightarrow \pi_x^*, \pi_{Ph,x}^*$

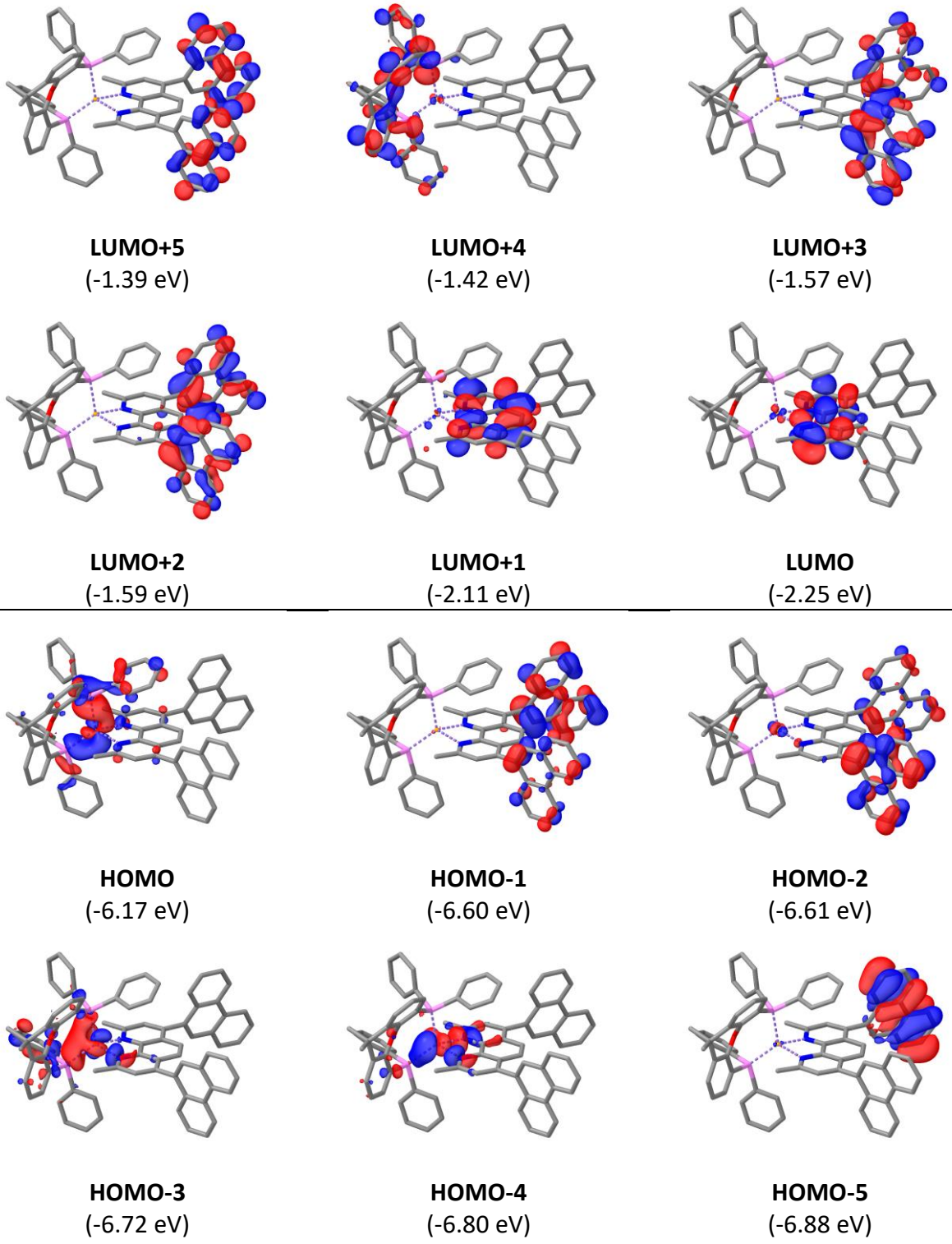

Figure S6.18. PBE0/def2-TZVP ground state frontier molecular orbitals of **CunP** with respective energies in parentheses. Positive lobes are depicted in red and negative in blue.

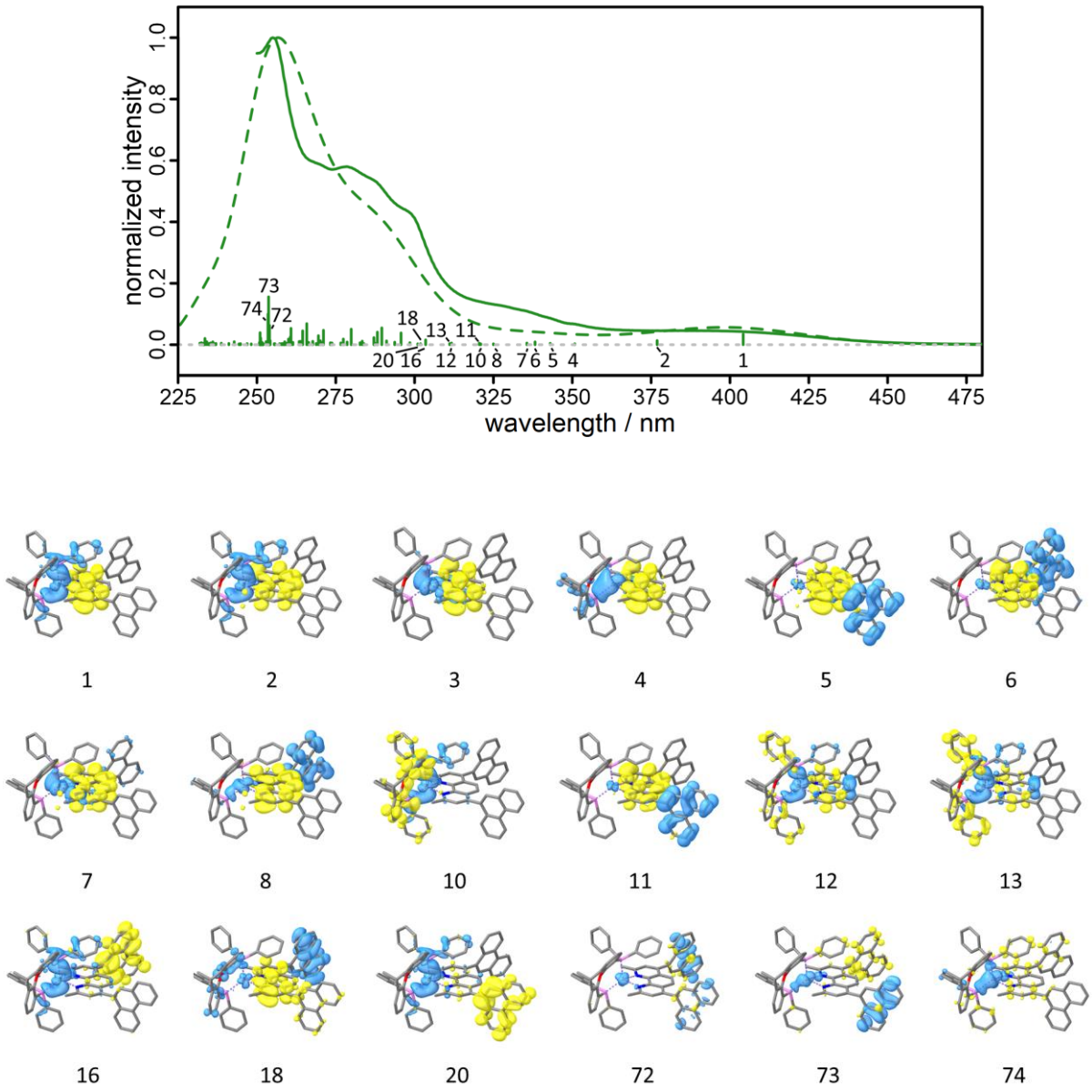

Figure S6.19. Normalized broadened calculated singlet excitation energies (dashed) with PBE0/def2-TZVP compared to the normalized experimental absorption spectrum (solid) of **CunP** (top). Sticks are scaled down by a factor of 0.25. Difference density plots corresponding to the excitation energies visualize the migration of electron density from cyan (-) to yellow (+) during the excitation (bottom).

Table S6.9. Excitation energies, oscillator strengths f_{osc} and corresponding transitions of **CunP** obtained from TD-DFT with PBE0/def2-TZVP simulated in dichloromethane. Excitations with an oscillator strength > 0.01 and corresponding orbital contributions with an OC ≥ 0.15 are given. Phenyl rings and xantphos are abbreviated as x and Ph.

State	Exc. energy		f_{osc}	Dominant contribution			Transition
#	cm^{-1}	nm		OC	occ. orb.	virt. orb.	
1	24741.8	404.2	0.136	0.959	HOMO	LUMO	$d_{Cu} \rightarrow \pi_{neo}^*$
2	26535.0	376.9	0.054	0.937	HOMO	LUMO+1	$d_{Cu} \rightarrow \pi_{neo}^*$
3	27060.3	369.5	0.009	0.587	HOMO-4	LUMO	$d_{Cu} \rightarrow \pi_{neo}^*$
				0.242	HOMO-3	LUMO	$d_{Cu} \rightarrow \pi_{neo}^*$
4	28507.0	350.8	0.012	0.228	HOMO-4	LUMO	$d_{Cu} \rightarrow \pi_{neo}^*$
				0.640	HOMO-3	LUMO	$d_{Cu} \rightarrow \pi_{neo}^*$
5	29150.7	343.0	0.018	0.339	HOMO-2	LUMO	$\pi_P \rightarrow \pi_{neo}^*$
				0.404	HOMO-1	LUMO	$\pi_P \rightarrow \pi_{neo}^*$
6	29569.6	338.2	0.036	0.337	HOMO-2	LUMO	$\pi_P \rightarrow \pi_{neo}^*$
				0.203	HOMO-1	LUMO	$\pi_P \rightarrow \pi_{neo}^*$
				0.260	HOMO-1	LUMO+1	$\pi_P \rightarrow \pi_{neo}^*$
7	29794.8	335.6	0.022	0.538	HOMO-4	LUMO+1	$d_{Cu} \rightarrow \pi_{neo}^*$
				0.206	HOMO-3	LUMO+1	$d_{Cu} \rightarrow \pi_{neo}^*$
8	30765.7	325.0	0.011	0.222	HOMO-3	LUMO+1	$d_{Cu} \rightarrow \pi_{neo}^*$
				0.402	HOMO-1	LUMO+1	$\pi_P \rightarrow \pi_{neo}^*$
10	31150.2	321.0	0.010	0.844	HOMO	LUMO+4	$d_{Cu} \rightarrow \pi_x^*, \pi_{Ph}^*$
11	31202.8	320.5	0.021	0.529	HOMO-2	LUMO+1	$\pi_P \rightarrow \pi_{neo}^*$
12	32082.6	311.7	0.022	0.406	HOMO-8	LUMO	$\pi_{neo} \rightarrow \pi_{neo}^*$
				0.344	HOMO	LUMO+7	$d_{Cu} \rightarrow \pi_x^*, \pi_{Ph}^*$
13	32142.9	311.1	0.014	0.288	HOMO-8	LUMO	$\pi_{neo} \rightarrow \pi_{neo}^*$
				0.529	HOMO	LUMO+7	$d_{Cu} \rightarrow \pi_x^*, \pi_{Ph}^*$
16	32954.4	303.5	0.063	0.612	HOMO	LUMO+2	$d_{Cu} \rightarrow \pi_P^*$
				0.160	HOMO	LUMO+3	$d_{Cu} \rightarrow \pi_P^*$
18	33123.3	301.9	0.013	0.158	HOMO-7	LUMO	$\pi_x \rightarrow \pi_{neo}^*$
				0.362	HOMO-5	LUMO	$\pi_P \rightarrow \pi_{neo}^*$
20	33219.4	301.0	0.011	0.164	HOMO	LUMO+2	$d_{Cu} \rightarrow \pi_P^*$
				0.515	HOMO	LUMO+3	$d_{Cu} \rightarrow \pi_P^*$
72	39364.9	254.0	0.252	0.175	HOMO-5	LUMO+5	$\pi_P \rightarrow \pi_P^*$
73	39424.0	253.7	0.624	<0.15	-	-	-
74	39452.1	253.5	0.398	<0.15	-	-	-

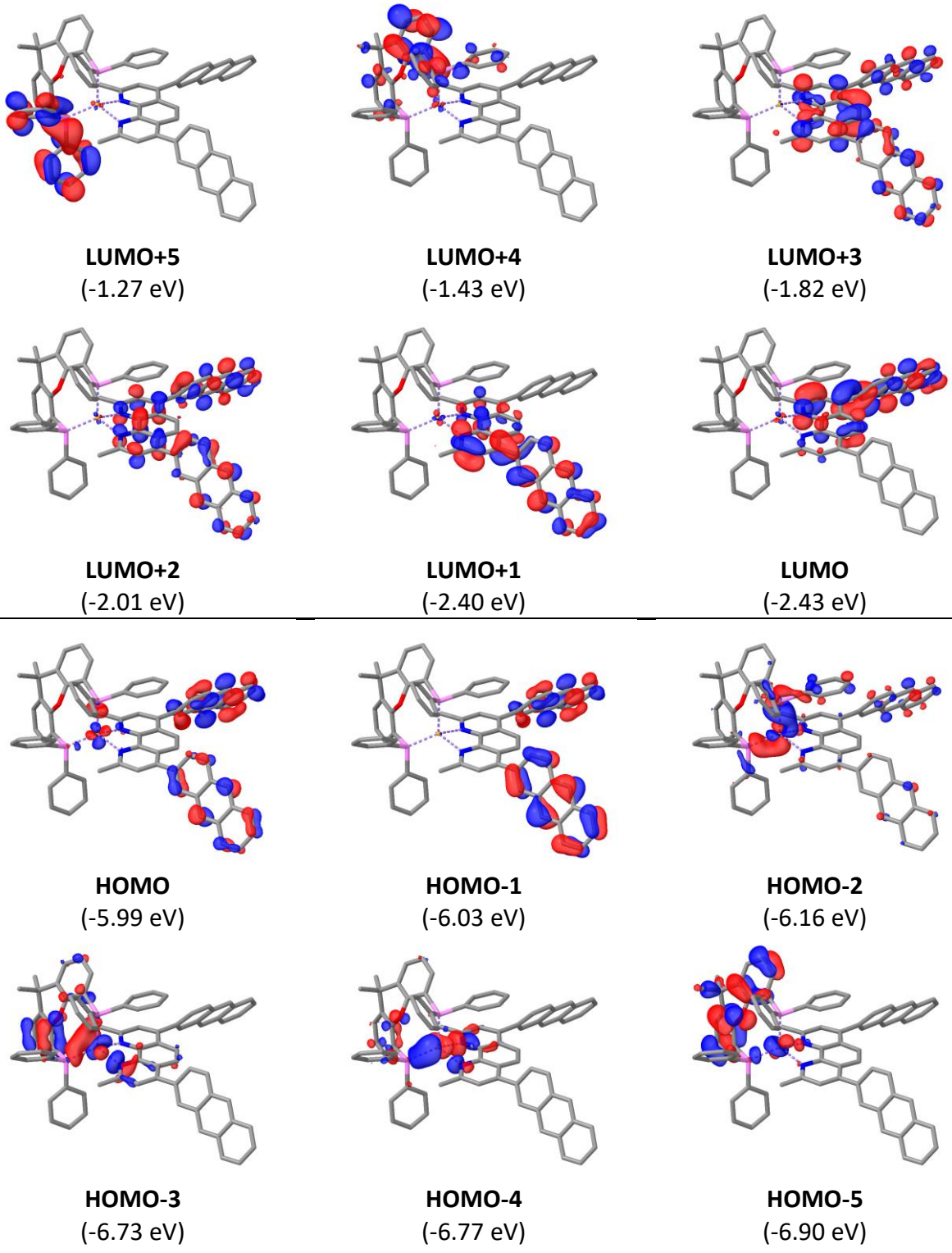

Figure S6.20. PBE0/def2-TZVP ground state frontier molecular orbitals of **CunA** with respective energies in eV in parentheses. Positive lobes are depicted in red and negative in blue.

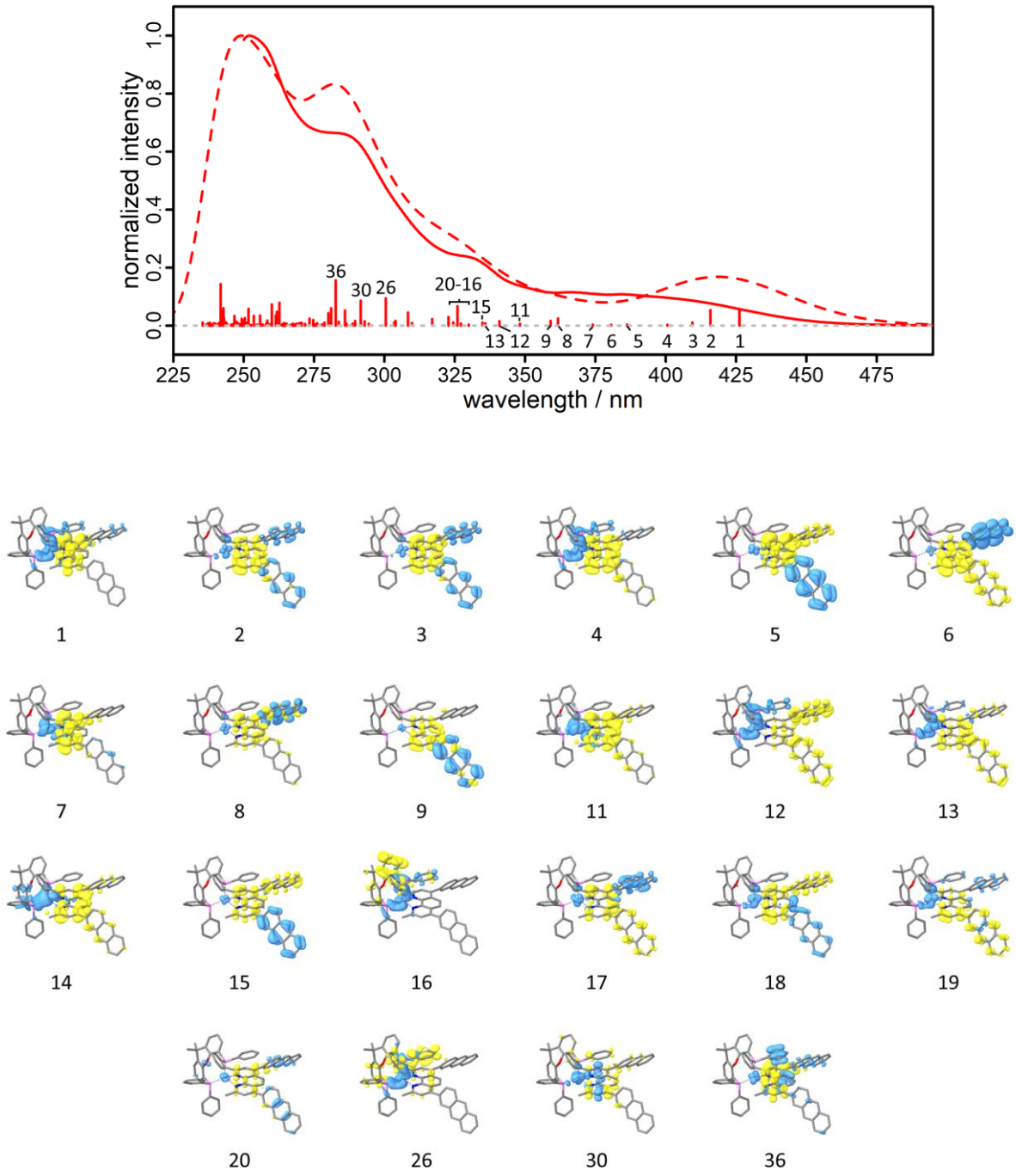

Figure S6.21. Normalized broadened calculated singlet excitation energies (dashed) with PBE0/def2-TZVP compared to the normalized experimental absorption spectrum (solid) of **CunA** (top). Sticks are scaled down by a factor of 0.25. Difference density plots corresponding to the excitation energies visualize the migration of electron density from cyan (-) to yellow (+) during the excitation (bottom).

Table S6.10. Excitation energies, oscillator strengths f_{osc} and corresponding transitions of **CunA** obtained from TD-DFT with PBE0/def2-TZVP simulated in dichloromethane. Excitations with an oscillator strength > 0.01 and corresponding orbital contributions with an OC ≥ 0.15 are given. Phenyl rings and xantphos are abbreviated as x and Ph.

State	Exc. energy		f_{osc}	Dominant contribution			Transition
#	cm^{-1}	nm		OC	occ. orb.	virt. orb.	
1	23461.6	426.2	0.212	0.428	HOMO	LUMO	π_A, $d_{Cu} \rightarrow \pi_A^*$, π_{neo}^*
				0.156	HOMO	LUMO+1	π_A, $d_{Cu} \rightarrow \pi_A^*$, π_{neo}^*
2	24042.8	415.9	0.215	0.212	HOMO-1	LUMO+1	$\pi_A \rightarrow \pi_A^*$, π_{neo}^*
				0.267	HOMO	LUMO	π_A, $d_{Cu} \rightarrow \pi_A^*$, π_{neo}^*
				0.352	HOMO	LUMO+1	π_A, $d_{Cu} \rightarrow \pi_A^*$, π_{neo}^*
3	24422.0	409.5	0.043	0.191	HOMO-2	LUMO	$d_{Cu} \rightarrow \pi_A^*$, π_{neo}^*
				0.285	HOMO-1	LUMO	$\pi_A \rightarrow \pi_A^*$, π_{neo}^*
				0.245	HOMO-1	LUMO+1	$\pi_A \rightarrow \pi_A^*$, π_{neo}^*
4	24963.8	400.6	0.012	0.331	HOMO-2	LUMO	$d_{Cu} \rightarrow \pi_A^*$, π_{neo}^*
				0.258	HOMO-2	LUMO+1	$d_{Cu} \rightarrow \pi_A^*$, π_{neo}^*
				0.197	HOMO-1	LUMO+1	$\pi_A \rightarrow \pi_A^*$, π_{neo}^*
5	25889.3	386.3	0.016	0.176	HOMO-2	LUMO	$d_{Cu} \rightarrow \pi_A^*$, π_{neo}^*
				0.462	HOMO-1	LUMO	$\pi_A \rightarrow \pi_A^*$, π_{neo}^*
				0.201	HOMO	LUMO	π_A, $d_{Cu} \rightarrow \pi_A^*$, π_{neo}^*
6	26276.2	380.6	0.012	0.322	HOMO-2	LUMO+1	$d_{Cu} \rightarrow \pi_A^*$, π_{neo}^*
				0.296	HOMO-1	LUMO+1	$\pi_A \rightarrow \pi_A^*$, π_{neo}^*
				0.303	HOMO	LUMO+1	π_A, $d_{Cu} \rightarrow \pi_A^*$, π_{neo}^*
7	26731.5	374.1	0.014	0.206	HOMO-4	LUMO	$d_{Cu} \rightarrow \pi_A^*$, π_{neo}^*
				0.253	HOMO-4	LUMO+1	$d_{Cu} \rightarrow \pi_A^*$, π_{neo}^*
				0.177	HOMO-3	LUMO+1	$d_{Cu} \rightarrow \pi_A^*$, π_{neo}^*
8	27644.8	361.7	0.099	0.680	HOMO	LUMO+2	π_A, $d_{Cu} \rightarrow \pi_{neo}^*$, π_A^*
9	27847	359.1	0.066	0.597	HOMO-1	LUMO+2	$\pi_A \rightarrow \pi_{neo}^*$, π_A^*
				0.207	HOMO	LUMO+3	π_A, $d_{Cu} \rightarrow \pi_{neo}^*$, π_A^*
11	28717.3	348.2	0.026	0.263	HOMO-4	LUMO+1	$d_{Cu} \rightarrow \pi_A^*$, π_{neo}^*
				0.372	HOMO-3	LUMO	$d_{Cu} \rightarrow \pi_A^*$, π_{neo}^*
12	29335.0	340.9	0.062	0.710	HOMO-2	LUMO+2	$d_{Cu} \rightarrow \pi_{neo}^*$, π_A^*
13	29773.4	335.9	0.031	0.152	HOMO-1	LUMO+2	$\pi_A \rightarrow \pi_{neo}^*$, π_A^*
				0.451	HOMO	LUMO+3	π_A, $d_{Cu} \rightarrow \pi_{neo}^*$, π_A^*
14	29863.3	334.9	0.043	0.201	HOMO-3	LUMO	$d_{Cu} \rightarrow \pi_A^*$, π_{neo}^*
				0.165	HOMO-3	LUMO+1	$d_{Cu} \rightarrow \pi_A^*$, π_{neo}^*
15	30303.8	330.0	0.014	0.455	HOMO-1	LUMO+3	$\pi_A \rightarrow \pi_{neo}^*$, π_A^*
16	30558.9	327.2	0.030	0.570	HOMO-2	LUMO+4	$d_{Cu} \rightarrow \pi_x^*$
				0.315	HOMO	LUMO+4	π_A, $d_{Cu} \rightarrow \pi_x^*$
17	30674.6	326.0	0.269	0.362	HOMO-6	LUMO	π_{neo}, $\pi_A \rightarrow \pi_A^*$, π_{neo}^*
				0.157	HOMO-2	LUMO+3	$d_{Cu} \rightarrow \pi_{neo}^*$, π_A^*
18	30815.2	324.5	0.044	0.257	HOMO-6	LUMO+1	π_{neo}, $\pi_A \rightarrow \pi_A^*$, π_{neo}^*
				0.254	HOMO-2	LUMO+3	$d_{Cu} \rightarrow \pi_{neo}^*$, π_A^*
19	30978.9	322.8	0.119	0.253	HOMO-6	LUMO+1	π_{neo}, $\pi_A \rightarrow \pi_A^*$, π_{neo}^*
				0.326	HOMO-2	LUMO+3	$d_{Cu} \rightarrow \pi_{neo}^*$, π_A^*
20	31546.3	317.0	0.091	0.207	HOMO-7	LUMO	π_A, $\pi_{neo} \rightarrow \pi_A^*$, π_{neo}^*
26	33275.1	300.5	0.377	0.429	HOMO-2	LUMO+7	π_A, $d_{Cu} \rightarrow \pi_{neo}^*$, π_A^*, π_x^*
				0.377	HOMO	LUMO+7	π_A, $d_{Cu} \rightarrow \pi_{neo}^*$, π_A^*, π_x^*
36	35372.5	282.7	0.625	0.257	HOMO-9	LUMO	π_{neo}, $\pi^*_{Ph} \rightarrow \pi_A^*$, π_{neo}^*

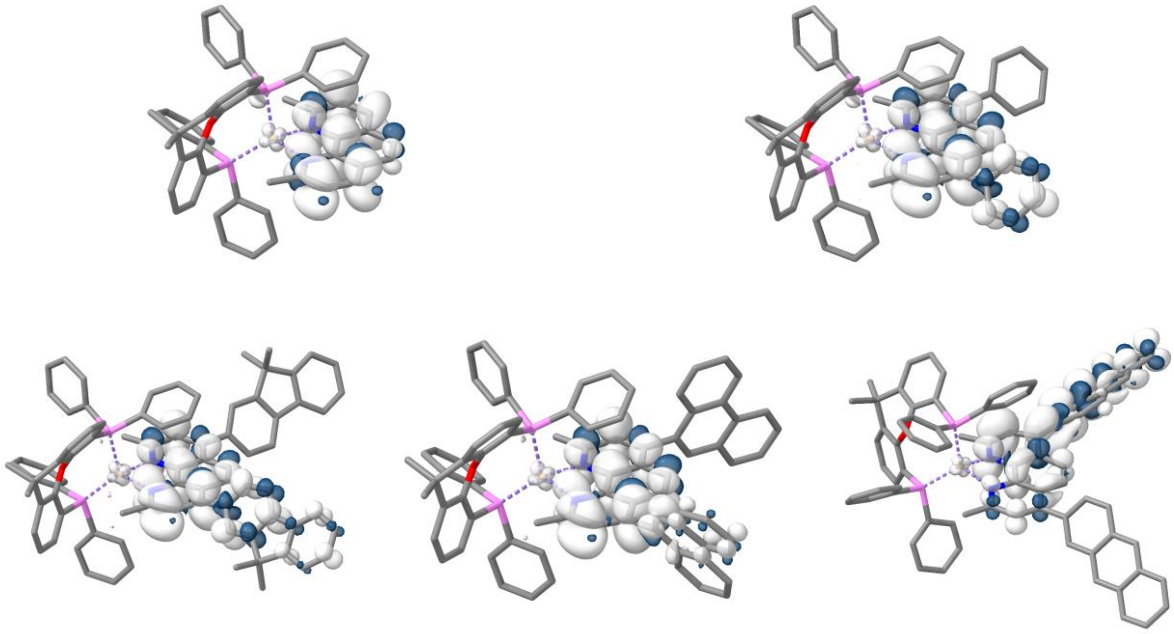

Figure S6.22. PBE0/def2-TZVP spin densities of the optimized reduced doublet state in vacuum in order from left to right: **Cuneo**, **Cubcp**, **CunF**, **CunP** and **CunA**.

Table S6.11. PBE0/def2-TZVP Gibbs free energy differences ΔG in kJ/mol, redox potential E° in V and redox reactions. ΔG^{g}_{redox} is the Gibbs free energy difference of the oxidized and reduced gas-phase structures (negative electron affinity or negative ionization potential for Fc/Fc^{+}), ΔG^{s}_{red} is the Gibbs free energy difference of the reduced gas-phase and solvated structure and ΔG^{s}_{ox} is that of the oxidized species. ΔG^{s}_{redox} is then obtained through the Born-Haber cycle as described in the experimental section. Numbers specified here have been converted to kJ/mol and rounded but have not been converted nor rounded for the calculation of $E°_{redox}$. The amount of electrons involved is n=1, the Faraday constant F equals 96.5 kJ/(mol·V) and the reference absolute potential chosen is the computed Fc/Fc^{+} oxidation potential.

Redox Reaction	ΔG^{g}_{redox}	ΔG^{s}_{red}	ΔG^{s}_{ox}	ΔG^{s}_{redox}	$E°_{redox}$(abs)	$E°_{redox}$(*vs.* ref)
	/ kJ/mol				/ V	
$Fc^{+\bullet} + e^{-} \rightarrow Fc$	-613.19	-33.46	-224.69	-421.96	4.37	-
$Cuneo^{+} + e^{-} \rightarrow Cuneo^{\bullet}$	-343.06	-121.19	-216.51	-247.74	2.57	-1.80
$Cubcp^{+} + e^{-} \rightarrow Cubcp^{\bullet}$	-340.23	-145.63	-231.64	-254.23	2.63	-1.74
$CunF^{+} + e^{-} \rightarrow CunF^{\bullet}$	-336.55	-182.32	-263.06	-255.81	2.65	-1.72
$CunP^{+} + e^{-} \rightarrow CunP^{\bullet}$	-337.85	-179.35	-265.41	-251.79	2.61	-1.76
$CunA^{+} + e^{-} \rightarrow CunA^{\bullet}$	-350.47	-188.50	-269.07	-269.90	2.80	-1.57

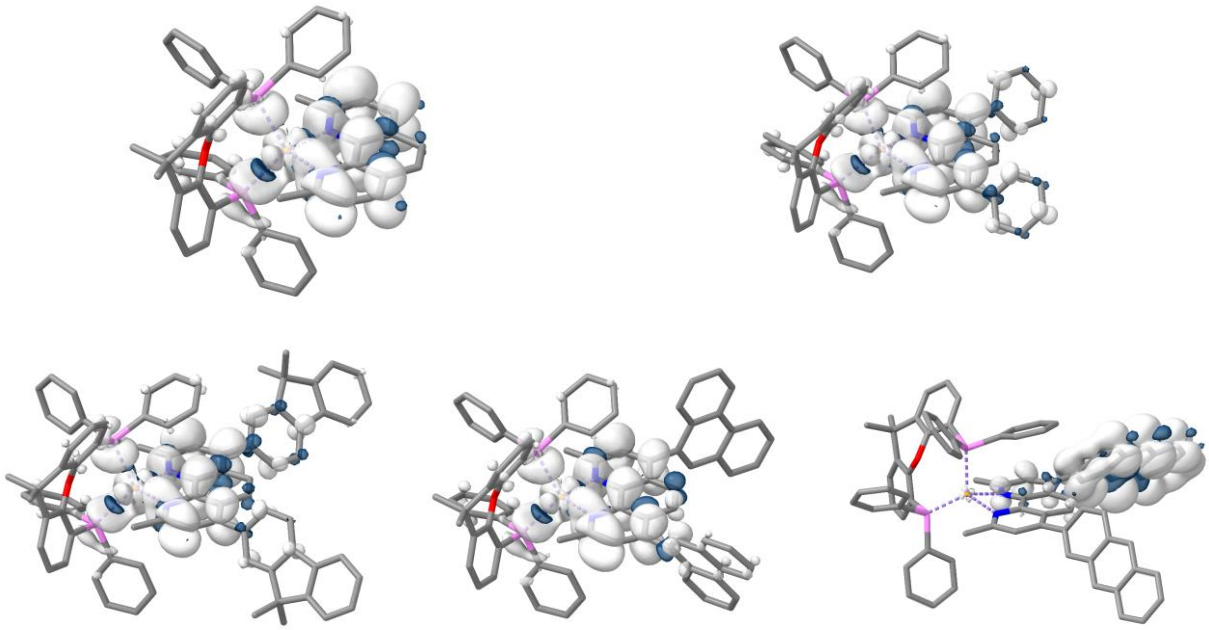

Figure S6.23. PBE0/def2-TZVP spin densities of the optimized triplet state in order from left to right: **Cuneo**, **Cubcp**, **CunF**, **CunP** and **CunA**.

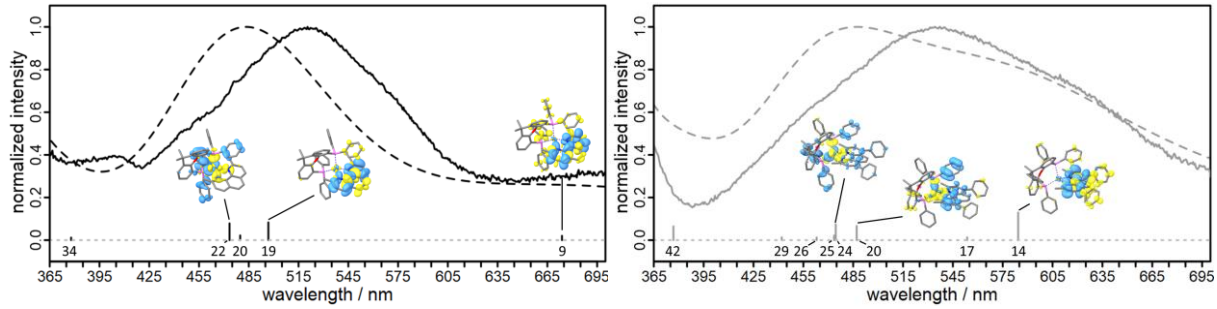

Figure S6.24. Computed triplet-triplet absorption spectra (dashed) of **Cuneo** (left) and **Cubcp** (right) in dichloromethane and selected difference density plots (yellow ← blue). The transient spectrum 10 ns after excitation recorded for 3 µs is overlaid (solid). The numbers associated with each excitation represents the transition $T_n \leftarrow T_1$. Sticks are unscaled.

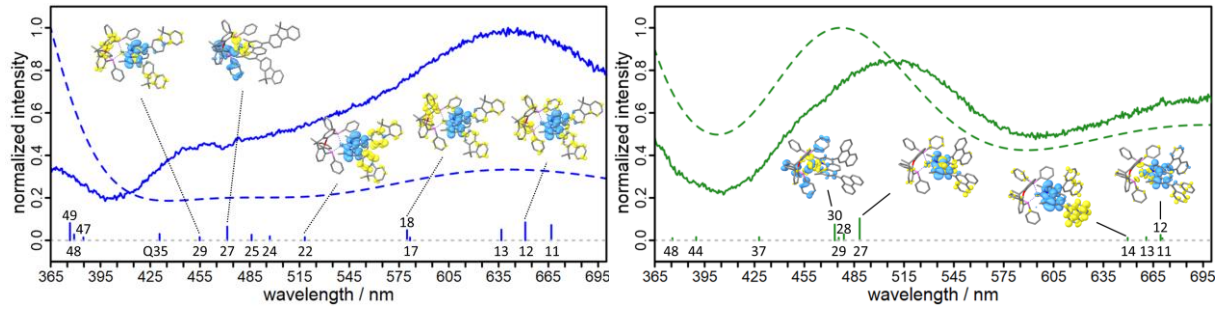

Figure S6.25. Computed triplet-triplet absorption spectra (dashed) of **CunF** (left) and **CunP** (right) in dichloromethane and selected difference density plots (yellow ← blue). The transient spectrum 10 ns after excitation recorded for 3 µs is overlaid (solid). The numbers associated with each excitation represents the transition $T_n \leftarrow T_1$. Q indicates a triplet to quartet excitation (S**2 = 3.75). Sticks are unscaled.

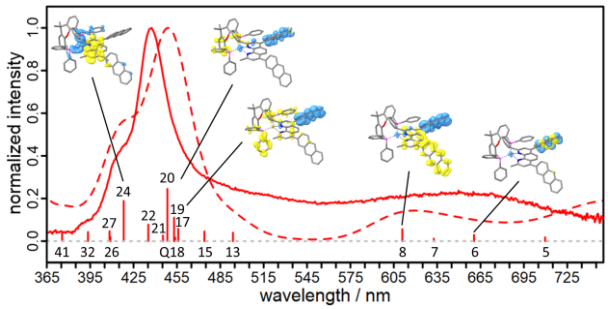

Figure S6.26. Computed triplet-triplet absorption spectra (dashed) of **CunA** in dichloromethane and selected difference density plots (yellow ← blue). The transient spectrum 10 ns after excitation recorded for 3 µs is overlaid (solid). The numbers associated with each excitation represents the transition $T_n \leftarrow T_1$. Q indicates a triplet to quartet excitation (S**2 = 3.75). Sticks are unscaled.

Table 6.12. Calculated state energies (final single point energies) of the complexes. The ground state (GS) energy is calculated on the electronic ground state with the relaxed electronic ground state structure (DFT). The S_1 energy is calculated the relaxed excited-state structure on the excited electronic state (TDDFT). The T_1 energy is calculated on the relaxed triplet state structure (DFT). The $S_0 - T_1$ energy is the energy of the relaxed triplet structure calculated on the electronic ground state (DFT).

Molecule	GS Energy /hartree	S_1 Energy /hartree	T_1 Energy /hartree	$S_0 - T_1$ Energy /hartree
Cuneo	-4551.9910	-4551.8951	-4551.9094	-4551.9708
Cubcp	-5013.7440	-5013.6484	-5013.6632	-5013.7235
CunF	-5708.8183	-5708.7228	-5708.7370	-5708.7981
CunP	-5627.8540	-5627.7593	-5627.7734	-5627.8339
CunA	-5627.8331	-5627.7423^{S1} -5627.7307^{S2}	-5627.7688	-5627.8214

7 Electrochemical Data

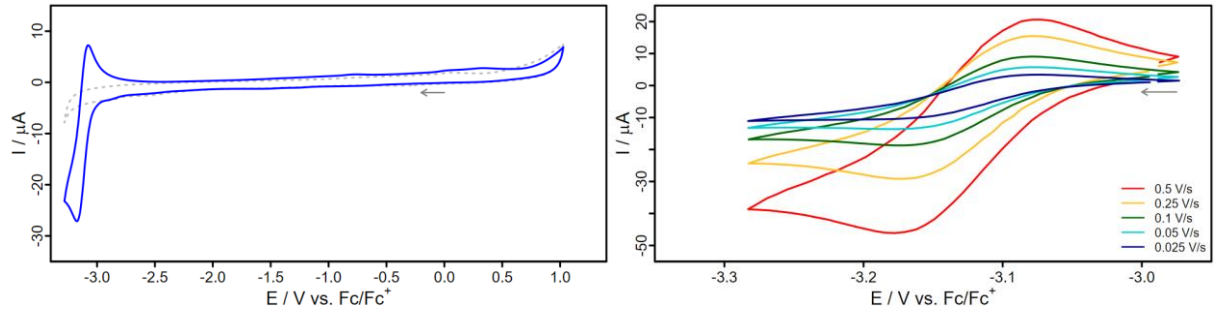

Figure S7.1. Cyclic voltammograms of **F** (1 mM) in dimethylformamide solution referenced against the ferrocene/ferrocenium couple (Fc/Fc^+). Cyclic voltammogram of the solvent is given for comparison (grey, dashed line). Conditions: scan rate of 100 mVs^{-1}, $[Bu_4N][PF_6]$ (0.1 M) as supporting electrolyte.

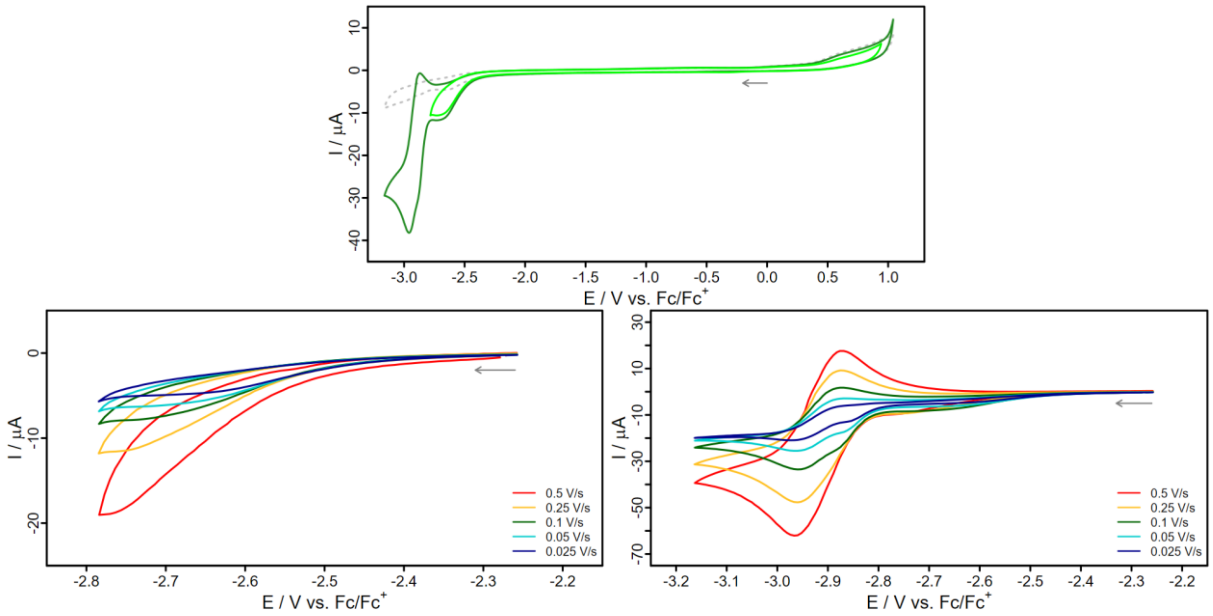

Figure S7.2. Cyclic voltammograms of **P** (1 mM) in dimethylformamide solution referenced against the ferrocene/ferrocenium couple (Fc/Fc^+). Cyclic voltammogram of the solvent is given for comparison (grey, dashed line). Conditions: scan rate of 100 mVs^{-1}, $[Bu_4N][PF_6]$ (0.1 M) as supporting electrolyte.

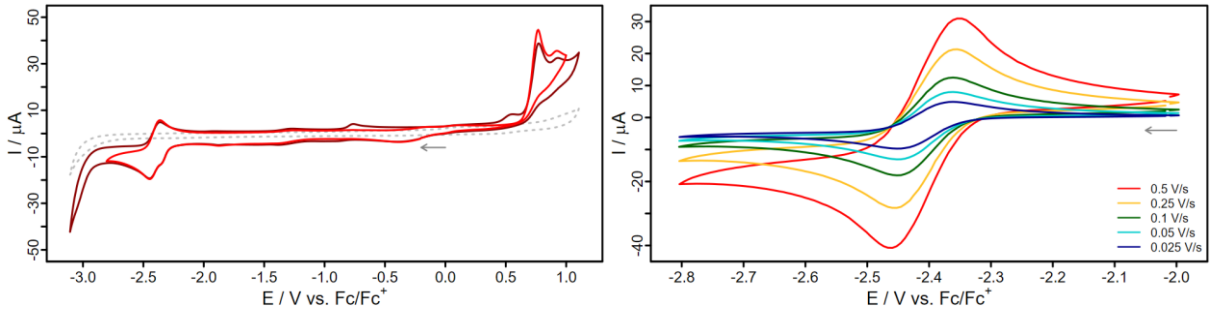

Figure S7.3. Cyclic voltammograms of **A** (1 mM) in dimethylformamide solution referenced against the ferrocene/ferrocenium couple (Fc/Fc^+). Cyclic voltammogram of the solvent is given for comparison (grey, dashed line). Conditions: scan rate of 100 mVs^{-1}, $[Bu_4N][PF_6]$ (0.1 M) as supporting electrolyte.

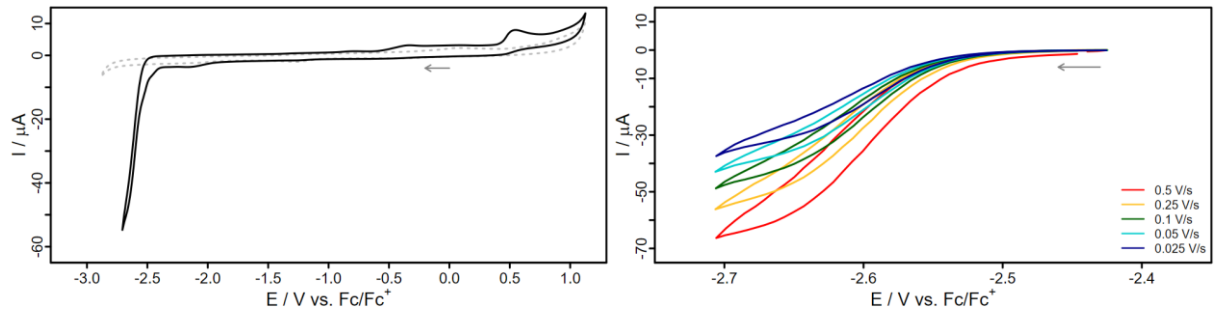

Figure S7.4. Cyclic voltammograms of **neo** (1 mM) in dimethylformamide solution referenced against the ferrocene/ferrocenium couple (Fc/Fc^+). Cyclic voltammogram of the solvent is given for comparison (grey, dashed line). Conditions: scan rate of 100 mVs^{-1}, $[Bu_4N][PF_6]$ (0.1 M) as supporting electrolyte.

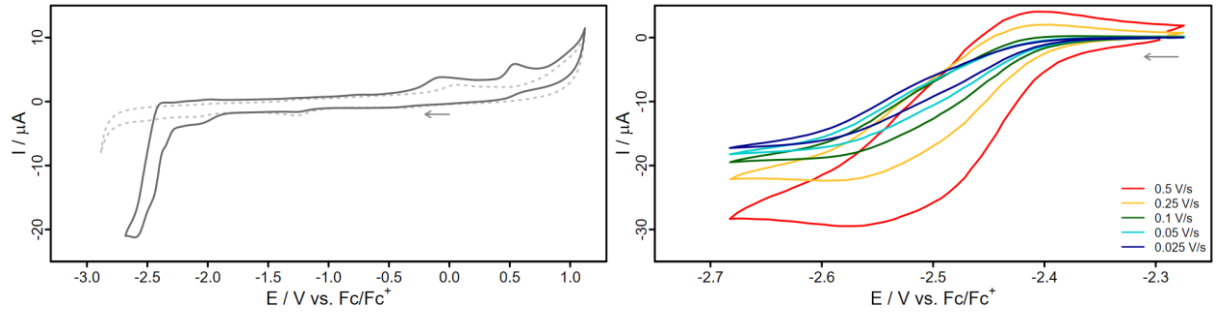

Figure S7.5. Cyclic voltammograms of **bcp** (1 mM) in dimethylformamide solution referenced against the ferrocene/ferrocenium couple (Fc/Fc^+). Cyclic voltammogram of the solvent is given for comparison (grey, dashed line). Conditions: scan rate of 100 mVs^{-1}, $[Bu_4N][PF_6]$ (0.1 M) as supporting electrolyte.

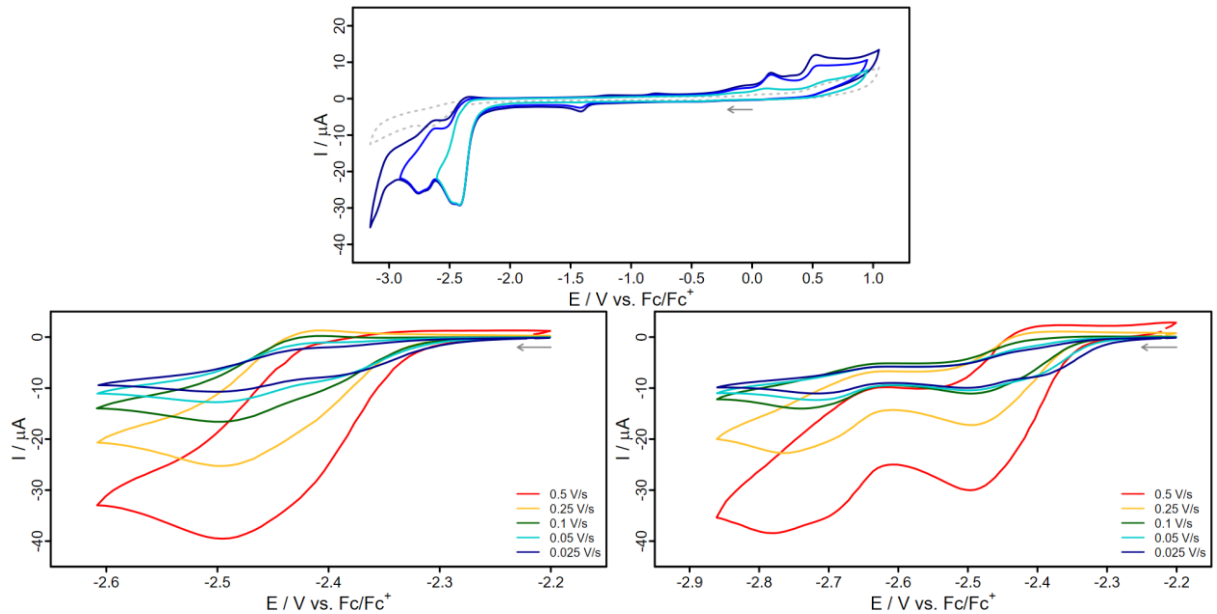

Figure S7.6. Cyclic voltammograms of **nF** (1 mM) in dimethylformamide solution referenced against the ferrocene/ferrocenium couple (Fc/Fc^+). Cyclic voltammogram of the solvent is given for comparison (grey, dashed line). Conditions: scan rate of 100 mVs^{-1}, $[Bu_4N][PF_6]$ (0.1 M) as supporting electrolyte.

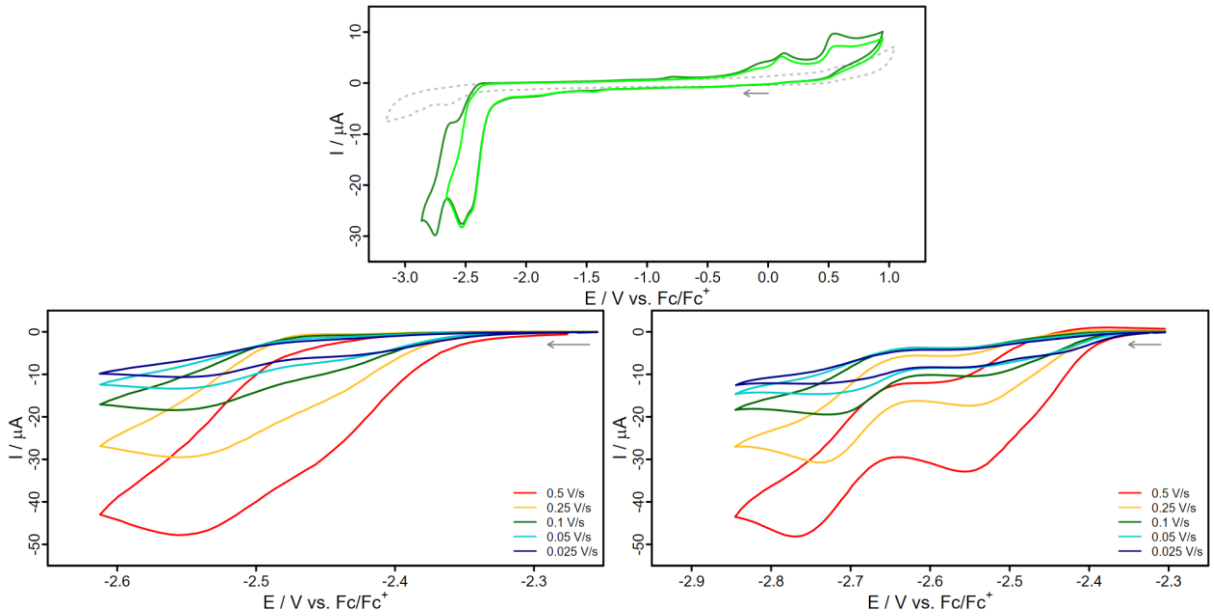

Figure S7.7. Cyclic voltammograms of **nP** (1 mM) in dimethylformamide solution referenced against the ferrocene/ferrocenium couple (Fc/Fc^+). Cyclic voltammogram of the solvent is given for comparison (grey, dashed line). Conditions: scan rate of 100 mVs^{-1}, $[Bu_4N][PF_6]$ (0.1 M) as supporting electrolyte.

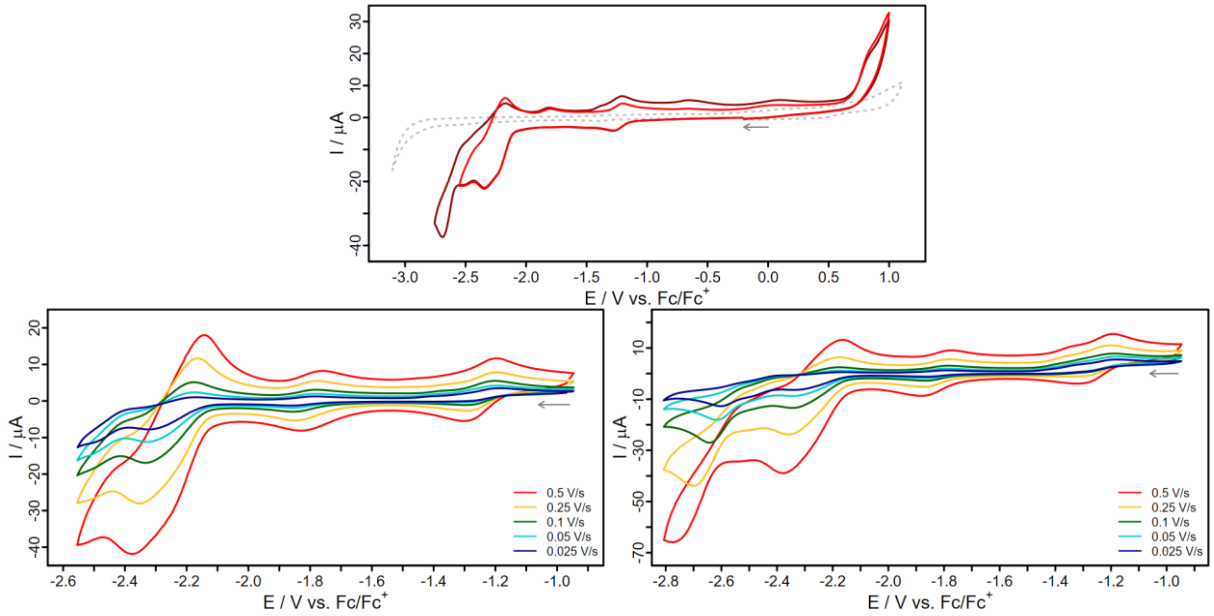

Figure S7.8. Cyclic voltammograms of **nA** (1 mM) in dimethylformamide solution referenced against the ferrocene/ferrocenium couple (Fc/Fc^+). Cyclic voltammogram of the solvent is given for comparison (grey, dashed line). Conditions: scan rate of 100 mVs^{-1}, $[Bu_4N][PF_6]$ (0.1 M) as supporting electrolyte.

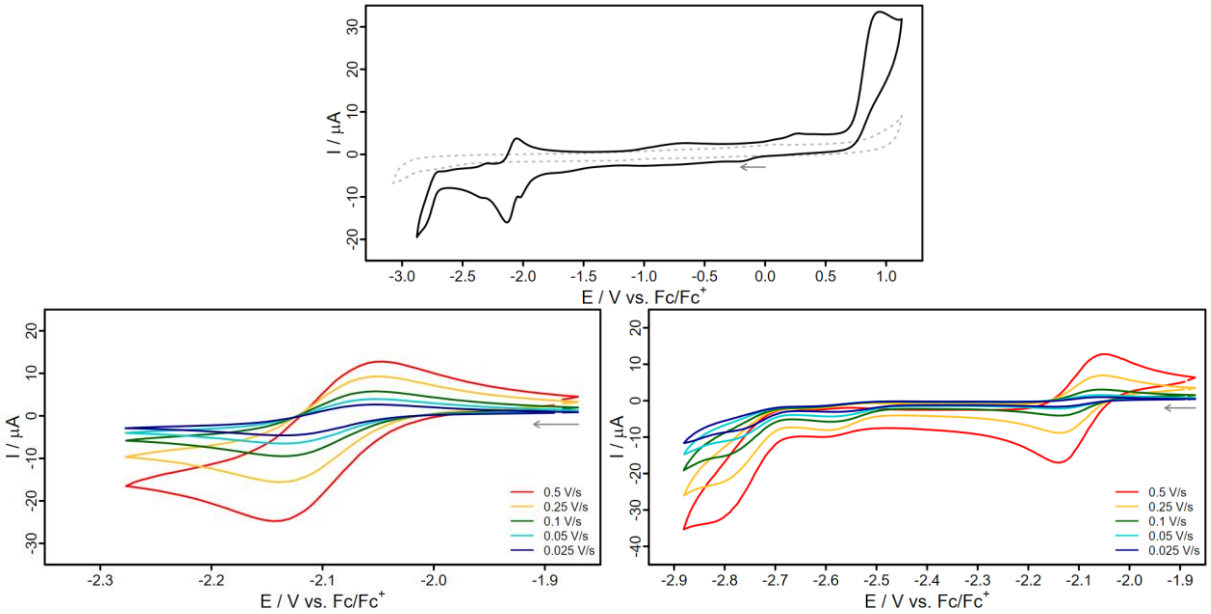

Figure S7.9. Cyclic voltammograms of **Cuneo** (1 mM) in dimethylformamide solution referenced against the ferrocene/ferrocenium couple (Fc/Fc^+). Cyclic voltammogram of the solvent is given for comparison (grey, dashed line). Conditions: scan rate of 100 mVs^{-1}, $[Bu_4N][PF_6]$ (0.1 M) as supporting electrolyte.

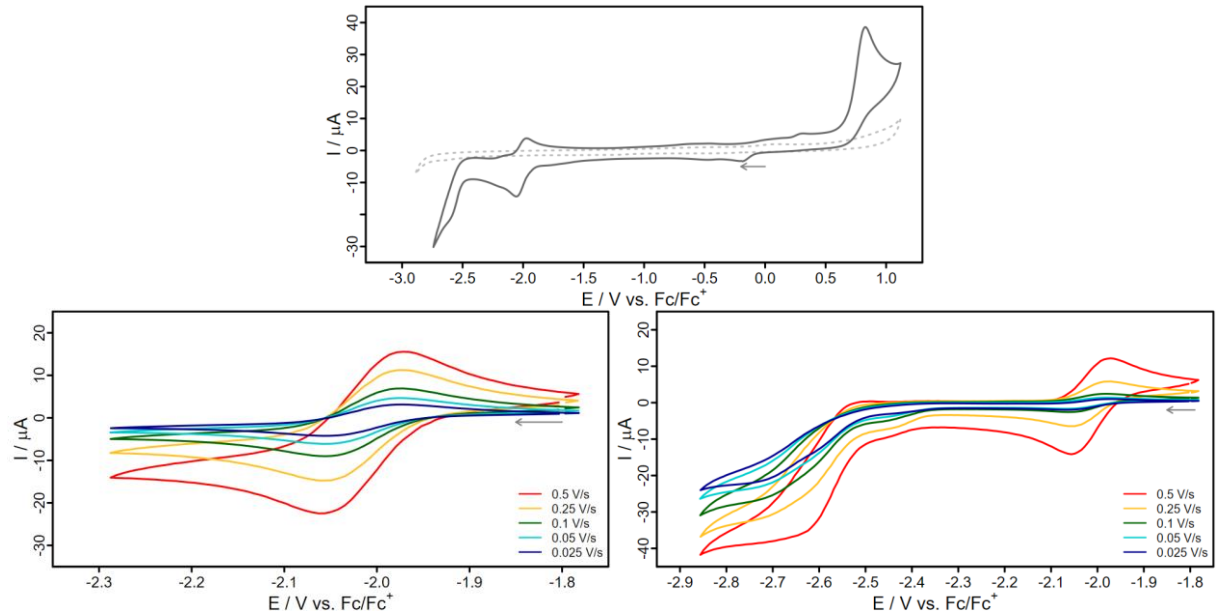

Figure S7.10. Cyclic voltammograms of **Cubcp** (1 mM) in dimethylformamide solution referenced against the ferrocene/ferrocenium couple (Fc/Fc^+). Cyclic voltammogram of the solvent is given for comparison (grey, dashed line). Conditions: scan rate of 100 mVs^{-1}, $[Bu_4N][PF_6]$ (0.1 M) as supporting electrolyte.

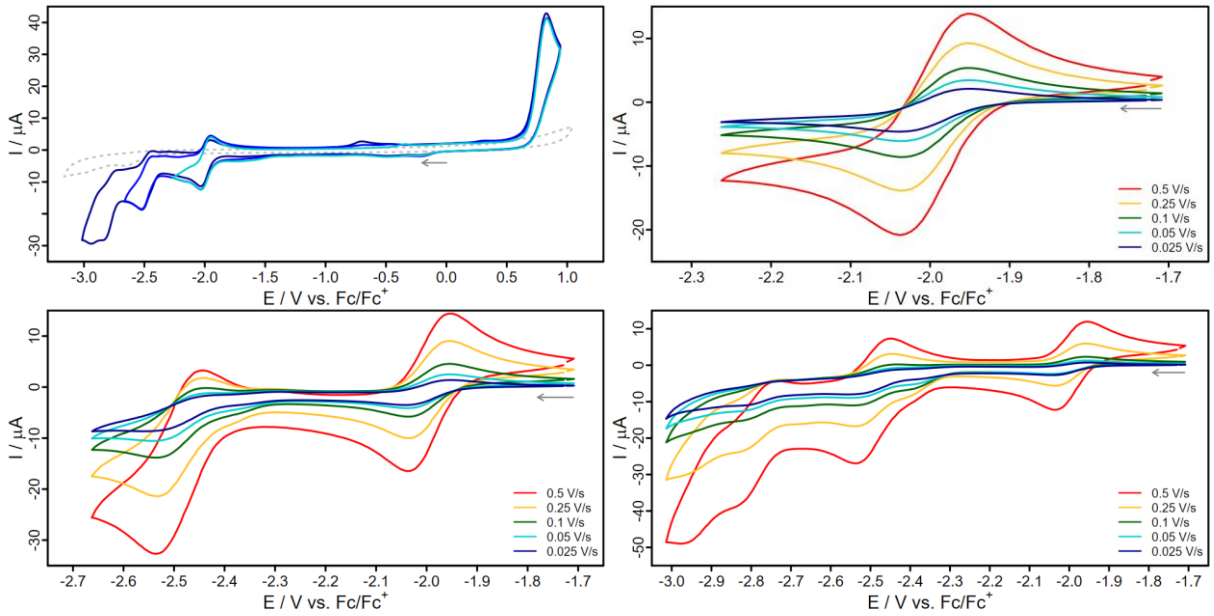

Figure S7.11. Cyclic voltammograms of **CunF** (1 mM) in dimethylformamide solution referenced against the ferrocene/ferrocenium couple (Fc/Fc^+). Cyclic voltammogram of the solvent is given for comparison (grey, dashed line). Conditions: scan rate of 100 mVs^{-1}, $[Bu_4N][PF_6]$ (0.1 M) as supporting electrolyte.

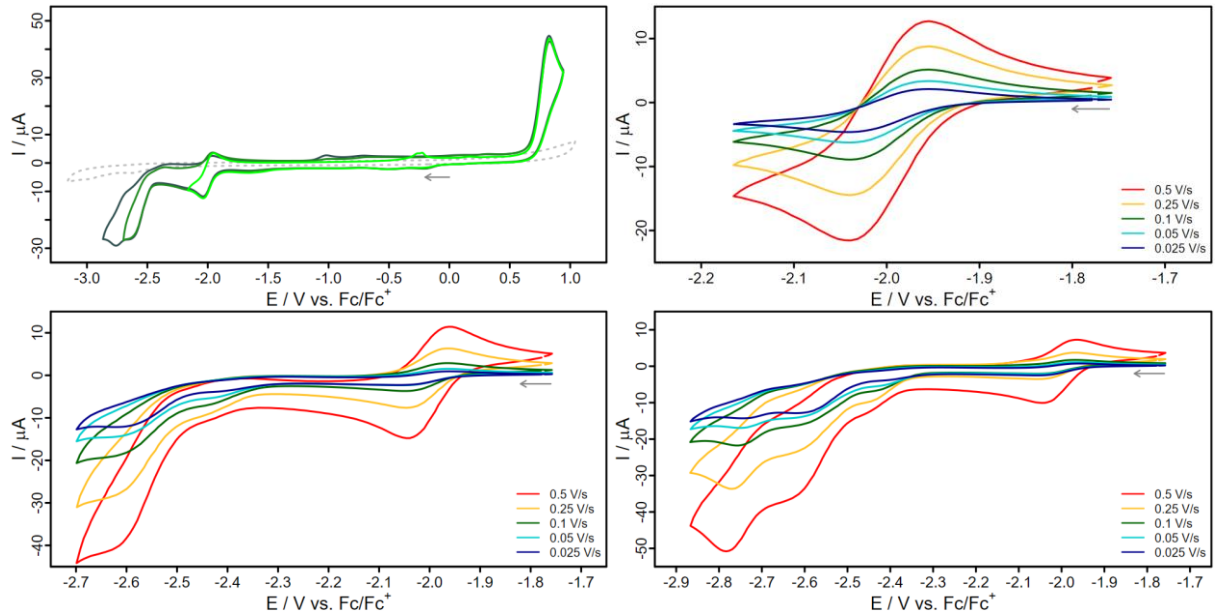

Figure S7.12. Cyclic voltammograms of **CunP** (1 mM) in dimethylformamide solution referenced against the ferrocene/ferrocenium couple (Fc/Fc^+). Cyclic voltammogram of the solvent is given for comparison (grey, dashed line). Conditions: scan rate of 100 mVs^{-1}, $[Bu_4N][PF_6]$ (0.1 M) as supporting electrolyte.

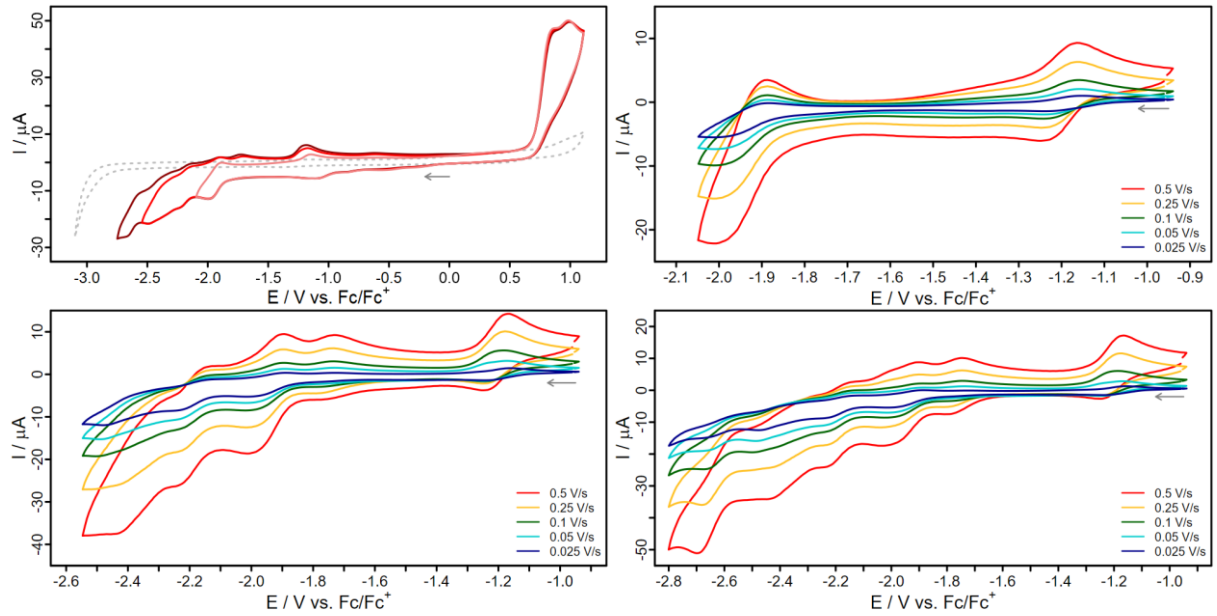

Figure S7.13. Cyclic voltammograms of **CunA** (1 mM) in dimethylformamide solution referenced against the ferrocene/ferrocenium couple (Fc/Fc^+). Cyclic voltammogram of the solvent is given for comparison (grey, dashed line). Conditions: scan rate of 100 mVs^{-1}, $[Bu_4N][PF_6]$ (0.1 M) as supporting electrolyte.

8 Steady-State Absorption Spectra

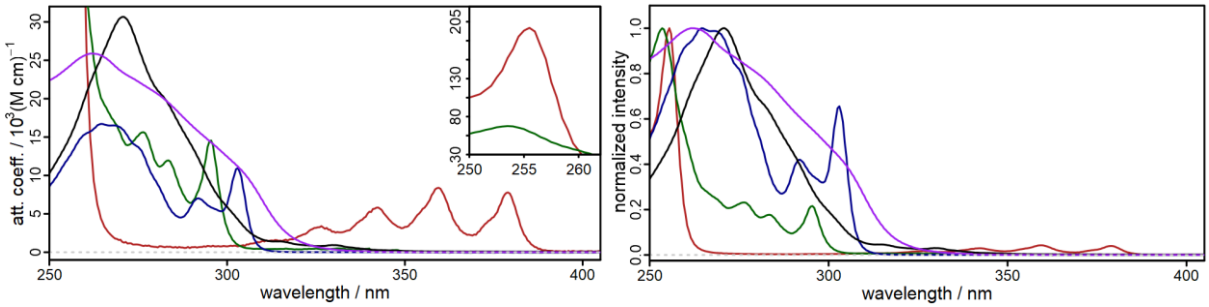

Figure S8.1. Attenuation coefficients (left) of **A** (red), **P** (green), **F** (blue), xantphos (violet), **neo** (black) and normalized absorption spectra (right).

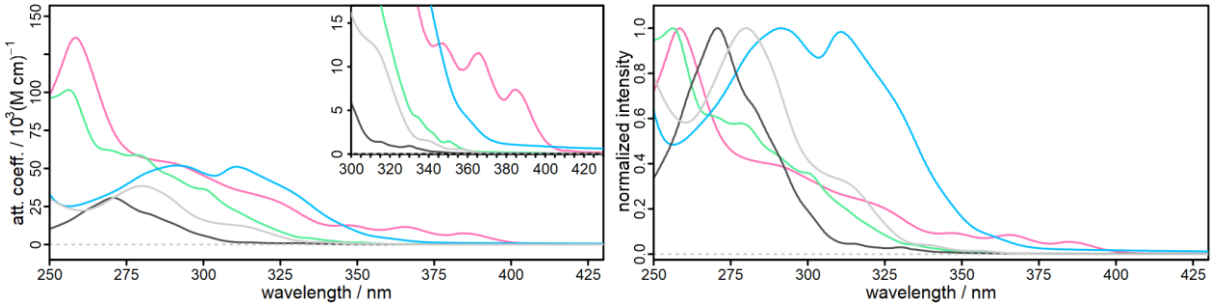

Figure S8.2. Attenuation coefficients (left) of **neo** (dark gray), **bcp** (light gray), **nA** (pink), **nP** (light green), **nF** (light blue) and normalized absorption spectra (right).

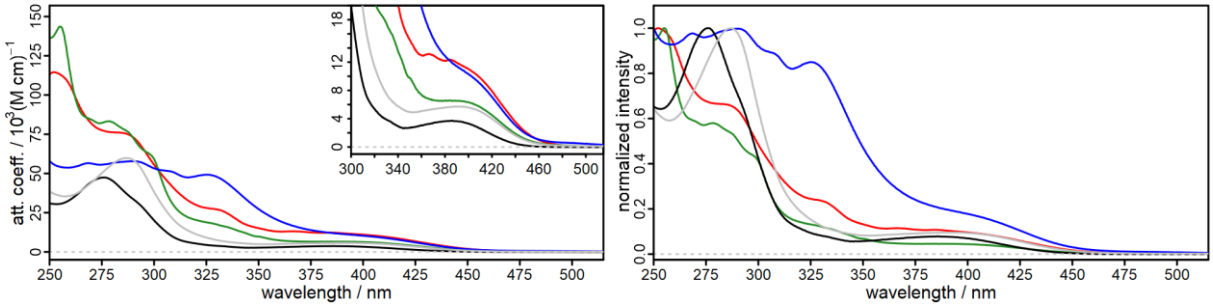

Figure S8.3. Attenuation coefficients (left) of **Cuneo** (black), **Cubcp** (gray), **CunF** (blue), **CunP** (green), **CunA** (red) and normalized absorption spectra (right).

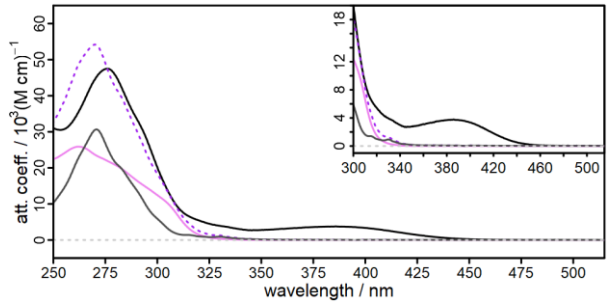

Figure S8.4. Attenuation coefficients of **neo** (gray), xantphos (violet), **Cuneo** (black) and the sum of **neo** + xantphos (dotted purple).

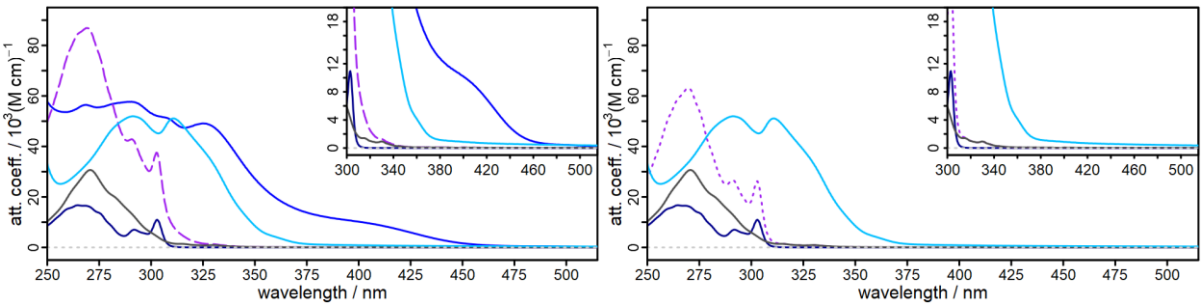

Figure S8.5. Attenuation coefficient sums of **CunF** (left) and **nF** (right). **CunF** (blue) is compared to the **nF** ligand (light blue), **neo** (dark gray), **F** (dark blue) and the sum of **neo** + 2**F** + xantphos (purple dashed). In the case of **nF** (right) the sum is given by **neo** + 2**F** (purple dotted).

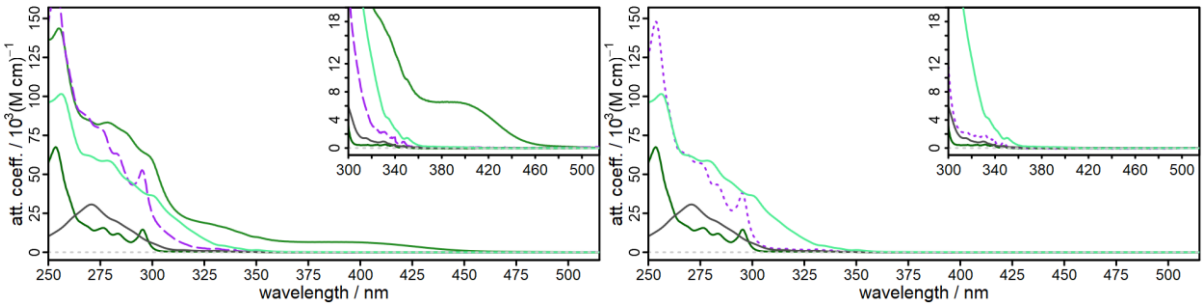

Figure S8.6. Attenuation coefficient sums of **CunP** (left) and **nP** (right). **CunP** (green) is compared to the **nP** ligand (light green), **neo** (dark gray), **P** (dark green) and the sum of **neo** + 2**P** + xantphos (purple dashed). In the case of **nP** (right) the sum is given by **neo** + 2**P** (purple dotted).

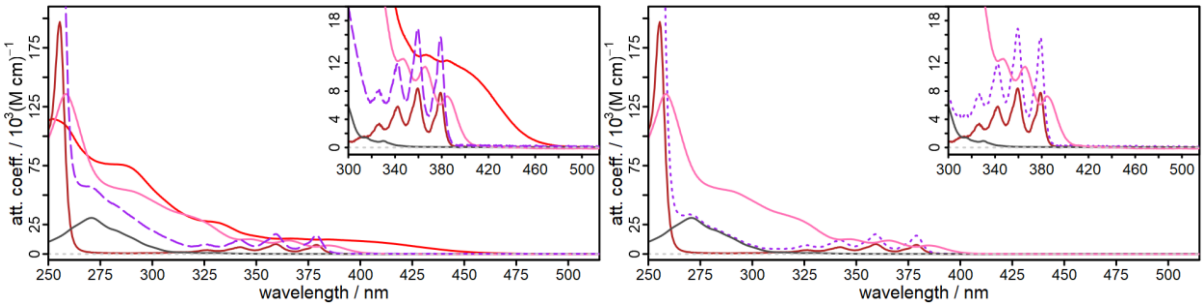

Figure S8.7. Attenuation coefficient sums of **CunA** (left) and **nA** (right). **CunA** (red) is compared to the **nA** ligand (light red), **neo** (dark gray), **A** (dark red) and the sum of **neo** + 2**A** + xantphos (purple dashed). In the case of **nA** (right) the sum is given by **neo** + 2**A** (purple dotted).

9 Steady-State Emission Spectra

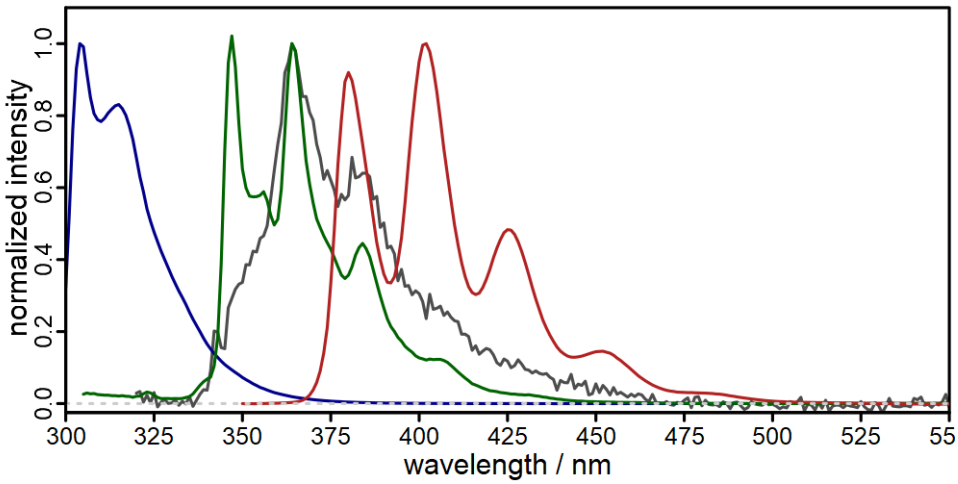

Figure S9.1. Normalized steady-state emission spectra of **neo** (black), **F** (blue), **P** (green) and **A** (red). Excitation at 310 nm (**neo**), 292 nm (**F**), 295 nm (**P**) and 340 nm (**A**) at optical densities of 0.1. All compounds display structured emission in aerated dichloromethane: **neo** (347 nm, 364 nm, 384 nm); **F** (304 nm, 315 nm); **P** (347 nm, 364 nm, 384 nm); **A** (380 nm, 402 nm, 425 nm, 452 nm).

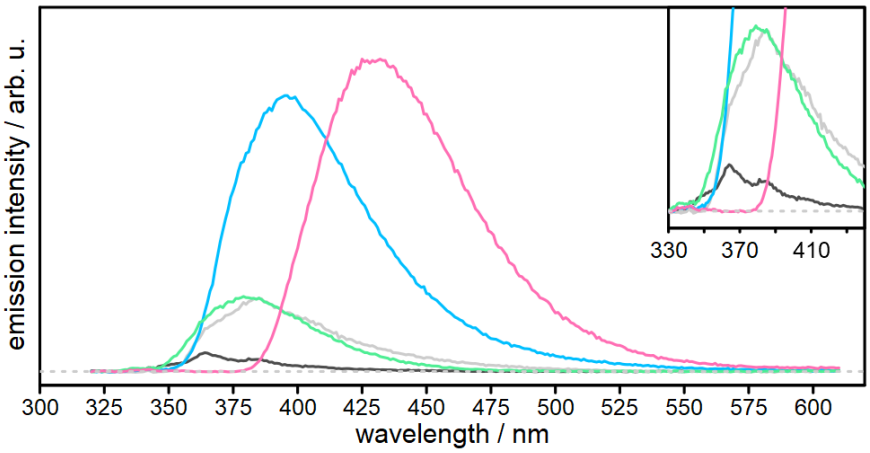

Figure S9.2. Steady-state emission spectra of **neo** (black), **bcp** (gray), **nF** (blue), **nP** (green) and **nA** (red) in degassed dichloromethane. λ_{exc} = 310 nm and $OD_{310\ nm} \approx 0.1$ has been chosen for all samples. Emission maxima/quantum yields are: 364 nm/<1 % (**neo**), 385 nm/4.6 % (**bcp**), 396 nm/29.6 % (**nF**), 379 nm/6.2 % (**nP**), 428 nm/46.4 % (**nA**).

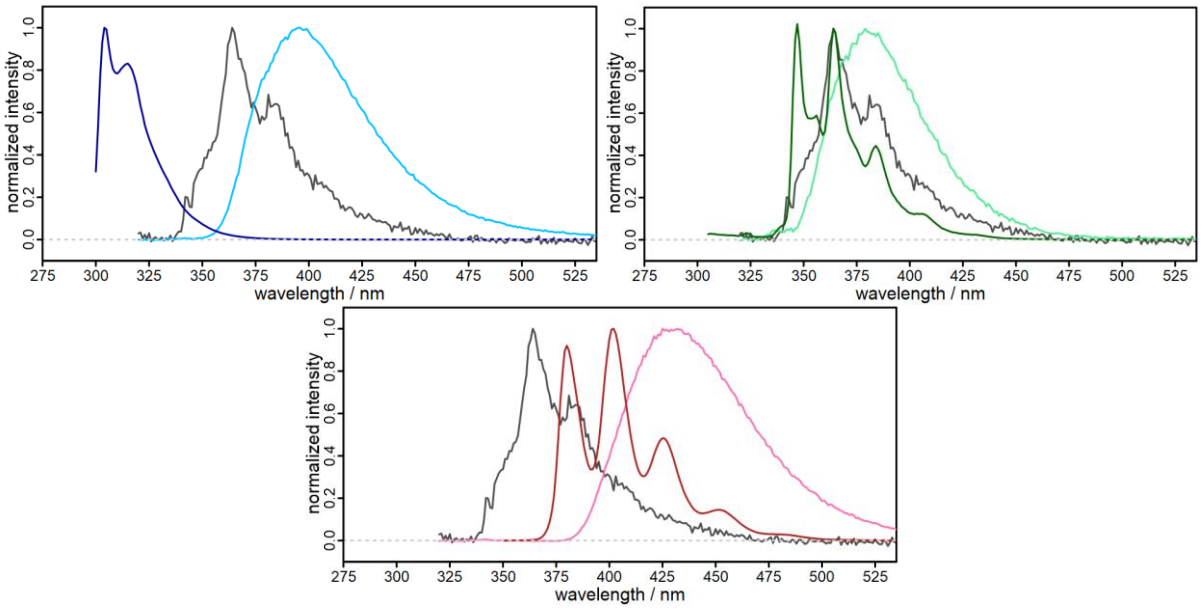

Figure S9.3. Overlaid normalized steady-state emission spectra of **neo** (black) with **F** and **nF** (dark and light blue, top left), **P** and **nP** (dark and light green, top right) and **A** and **nA** (dark and light red, bottom middle). For settings see previous spectra.

10 Time-resolved Emission Spectra

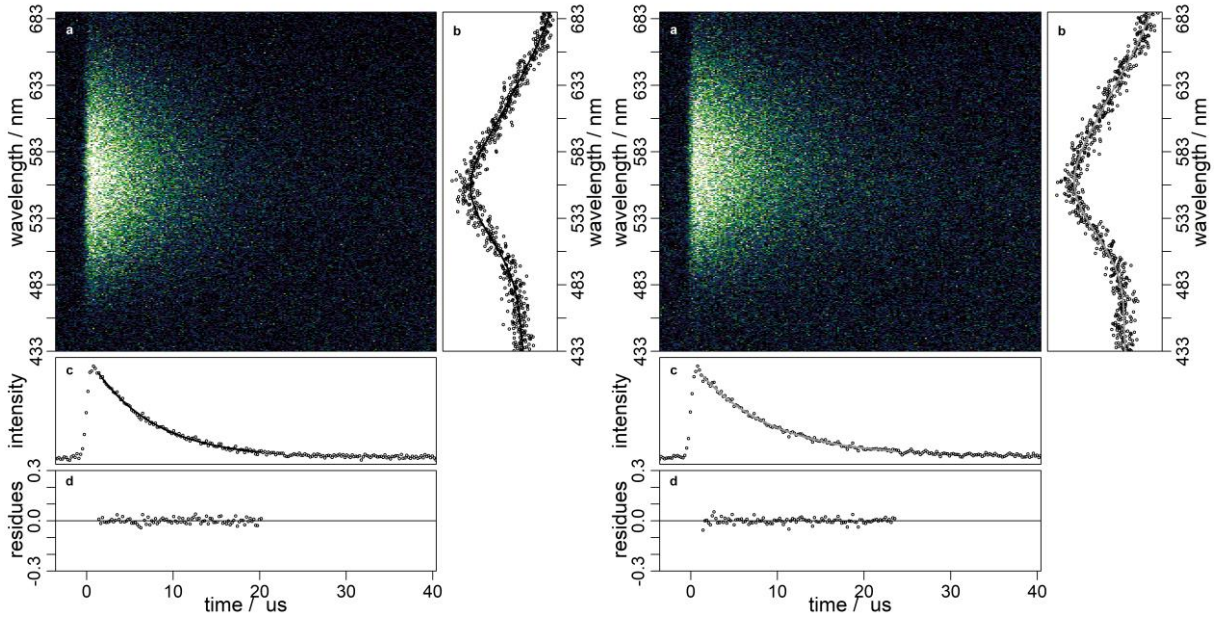

Figure S10.1. Time resolved emission of **Cuneo** (left) and **Cubcp** (right). a) shows the streak image, b) the summed emission spectrum, c) the summed fitted kinetics and d) shows the residuals of the fit. The excited state lifetimes were calculated via a single exponential fit to 7.08 µs and 8.40 µs respectively.

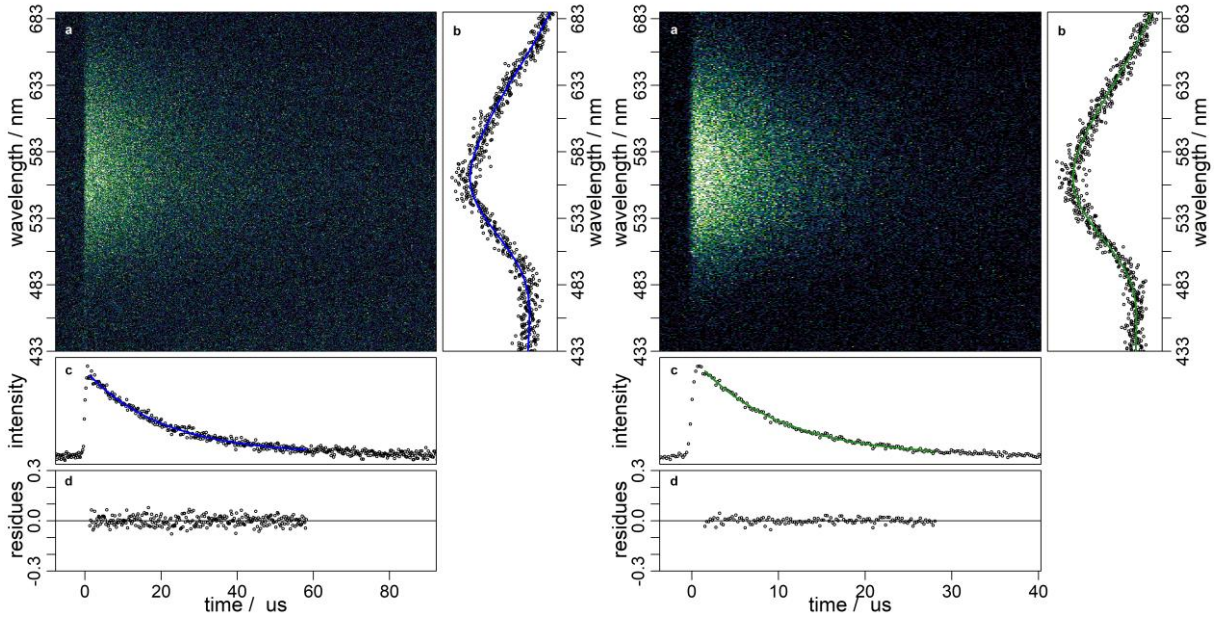

Figure S10.2. Time resolved emission spectra of **CunF** (left) and **CunP** (right). a) shows the streak image, b) the summed emission spectrum, c) the summed fitted kinetics and d) shows the residuals of the fit. The excited state lifetimes were calculated via single exponential fit to 20.22 µs and 9.70 µs respectively.

11 Transient Absorption Spectroscopy

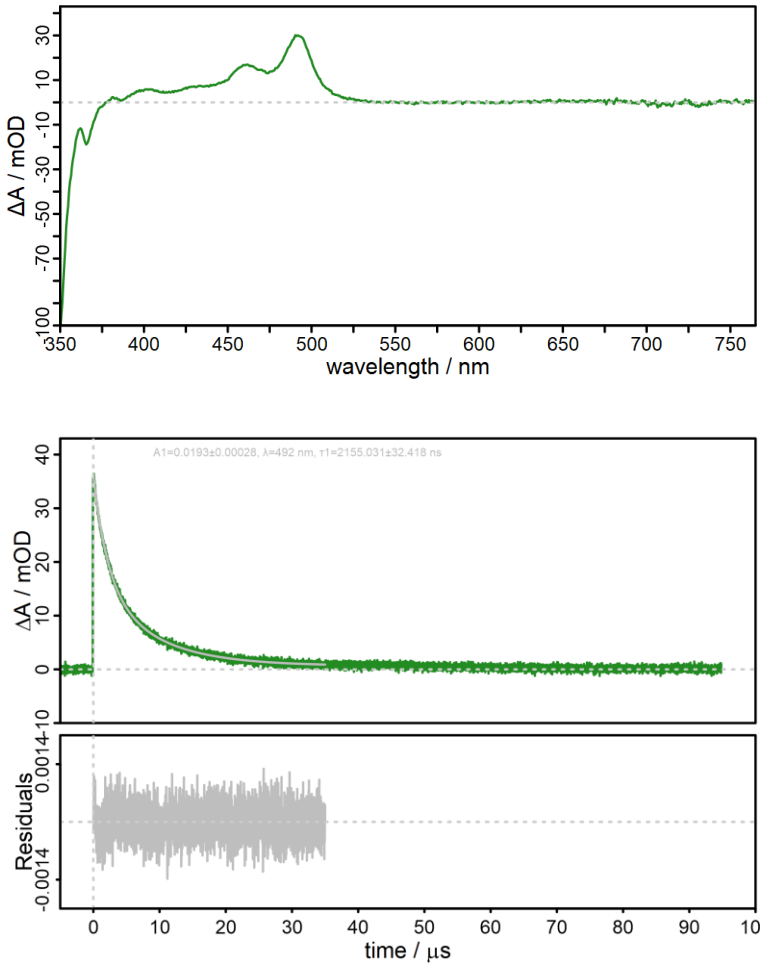

Figure S11.1. Nanosecond-transient absorption spectrum (top) recorded 10 ns after excitation for 3 µs and kinetic at 492 nm (bottom) of **P** in inert dichloromethane. The biexponential fit of 492 nm (middle) has the lifetimes τ_1 = 8.35±0.13 µs (76.5 %) and τ_2 = 2.16±0.03 µs (23.5 %). The residuals of the fit are given below the fit. **P** has a structured triplet-triplet absorption band with peaks at 432 nm, 460 nm and 492 nm.

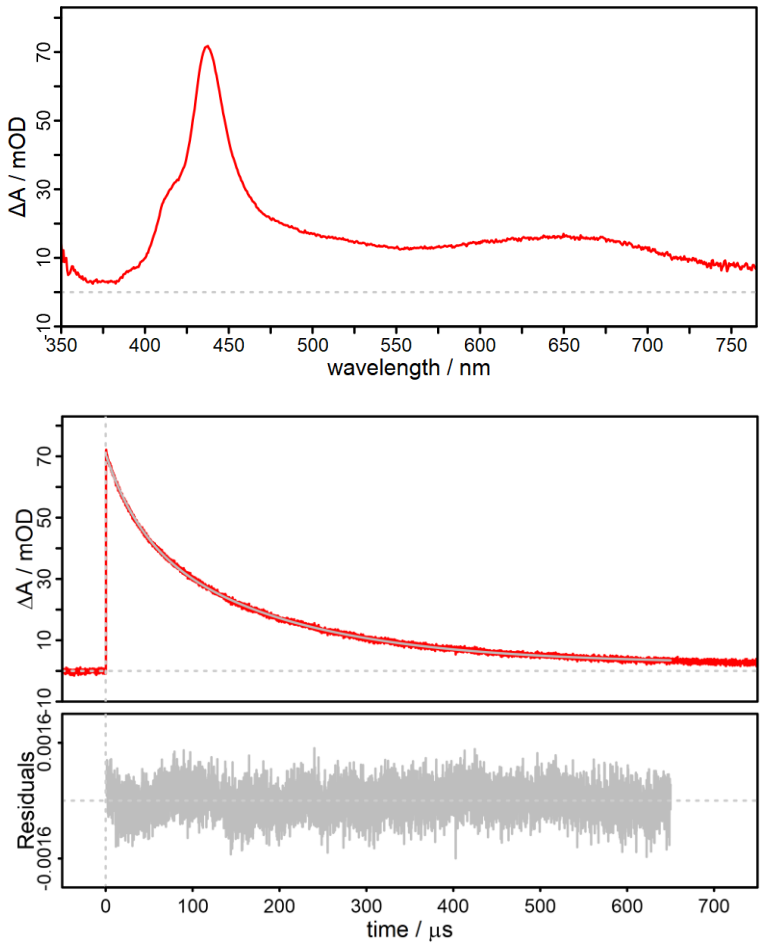

Figure S11.2. Nanosecond-transient absorption spectrum recorded 10 ns after excitation for 3 µs (top) and kinetic at 436 nm (middle) of **CunA** in inert dichloromethane. The biexponential fit has the lifetimes τ_1 = 37.28 ± 0.36 µs (9.1 %) and τ_2 = 174.36 ± 0.70 µs (90.8 %). The residuals of the fit are given below the fit. **CunA** possesses a sharp triplet-triplet absorption band centered at 437 nm with a shoulder at 415 nm. The bottom spectra compare the absorbance before (red) and after (purple) transient absorption measurements.

12 Photostability Measurements

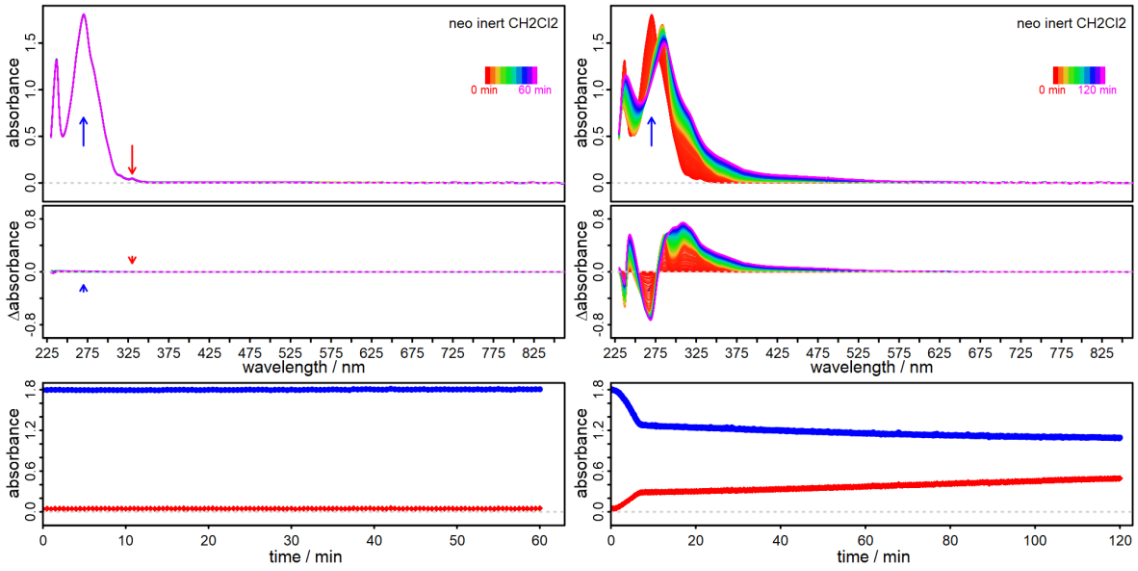

Figure S12.1. Photostability measurement of **neo** without (left) and with irradiation (right). The spectra (top) are recorded for 1 h for the blank measurement and for 2 h with a 150 W Xe arc lamp. The difference spectra (middle) outline the difference in absorbance. The kinetics (bottom) present the decay at 270 nm (blue) and the increase at 330 nm (red). The decomposition completes in roughly 5 minutes. A photoproduct with a weak green fluorescence (488 nm) remains.

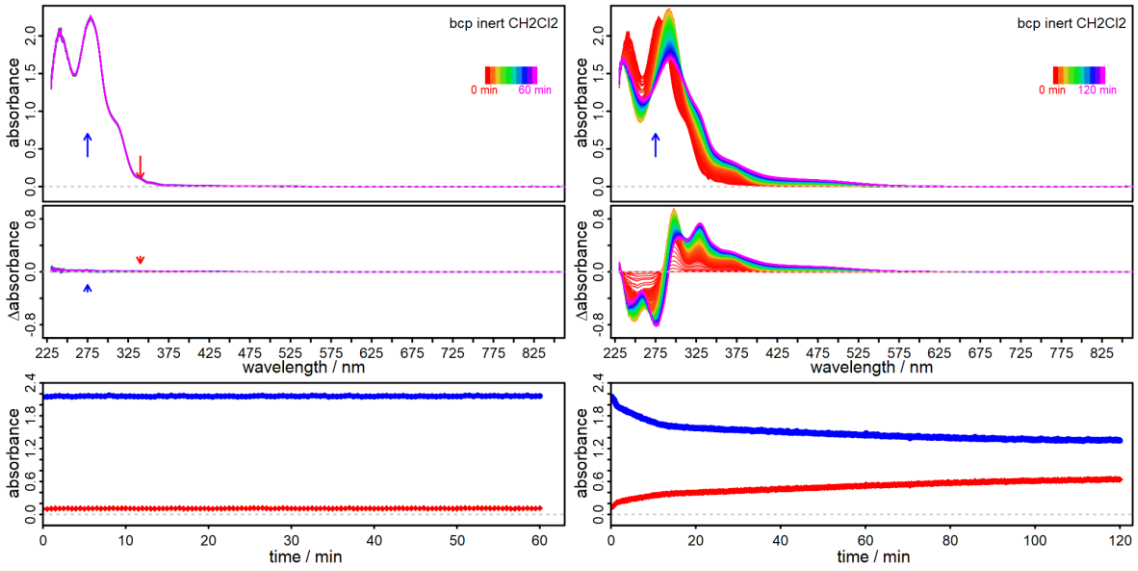

Figure S12.2. Photostability measurement of **bcp** without (left) and with irradiation (right). The spectra (top) are recorded for 1 h for the blank measurement and for 2 h with a 150 W Xe arc lamp. The difference spectra (middle) outline the difference in absorbance. The kinetics (bottom) present the decay at 275 nm (blue) and the increase at 340 nm (red). The decomposition slows down after roughly 10 minutes. A photoproduct with a predominantly blue fluorescence (444 nm) remains.

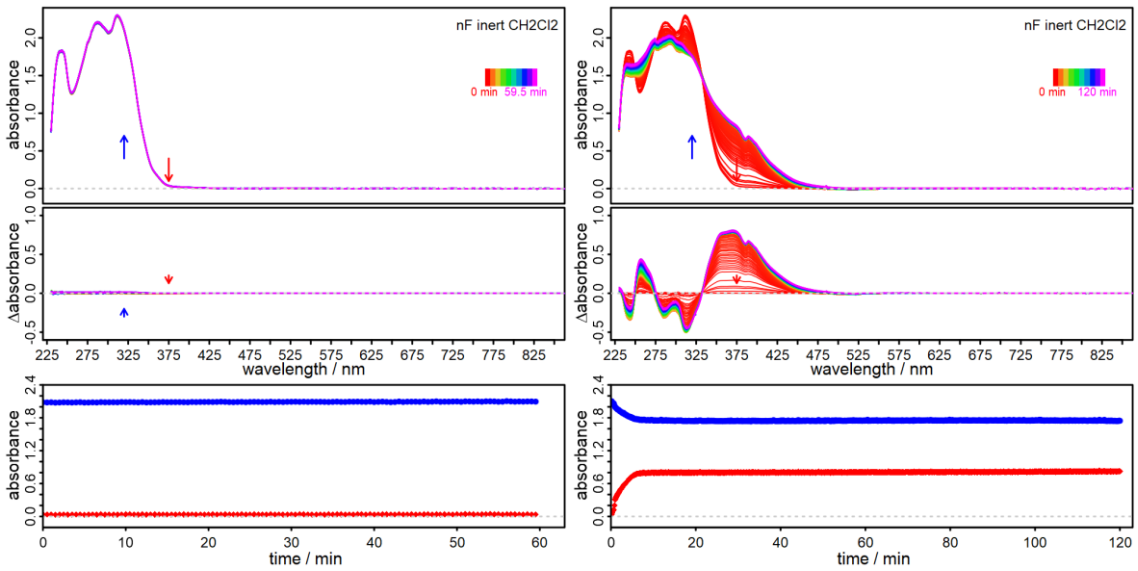

Figure S12.3. Photostability measurement of **nF** without (left) and with irradiation (right). The spectra (top) are recorded for 1 h for the blank measurement and for 2 h with a 150 W Xe arc lamp. The difference spectra (middle) outline the difference in absorbance. The kinetics (bottom) present the decay at 320 nm (blue) and the increase at 375 nm (red). The decomposition completes in roughly 5 minutes. A photoproduct with a green fluorescence (508 nm) remains.

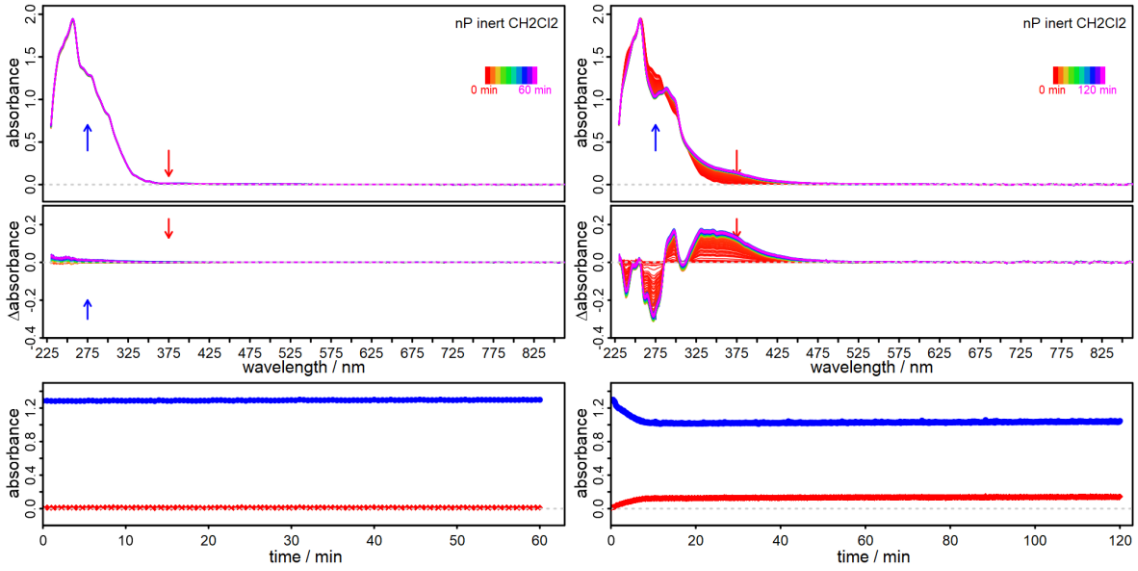

Figure S12.4. Photostability measurement of **nP** without (left) and with irradiation (right). The spectra (top) are recorded for 1 h for the blank measurement and for 2 h with a 150 W Xe arc lamp. The difference spectra (middle) outline the difference in absorbance. The kinetics (bottom) present the decay at 275 nm (blue) and the increase at 375 nm (red). The decomposition completes in roughly 5 minutes. A photoproduct with a green fluorescence (520 nm) remains.

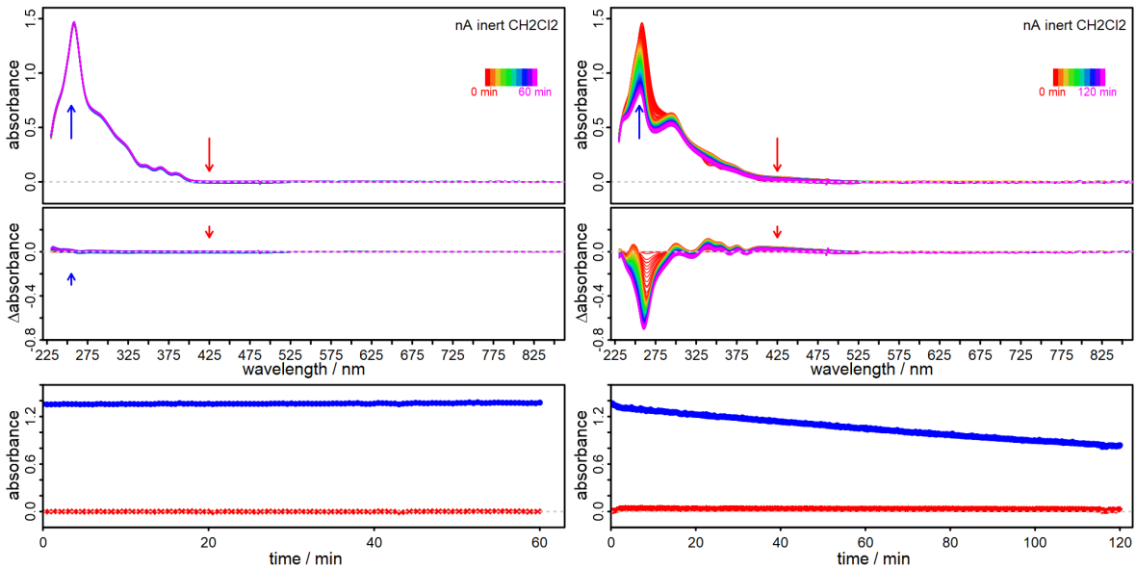

Figure S12.5. Photostability measurement of **nA** without (left) and with irradiation (right). The spectra (top) are recorded for 1 h for the blank measurement and for 2 h with a 150 W Xe arc lamp. The difference spectra (middle) outline the difference in absorbance. The kinetics (bottom) present the decay at 255 nm (blue) and the increase at 425 nm (red). A photoproduct with a faint orange fluorescence (617 nm) remains.

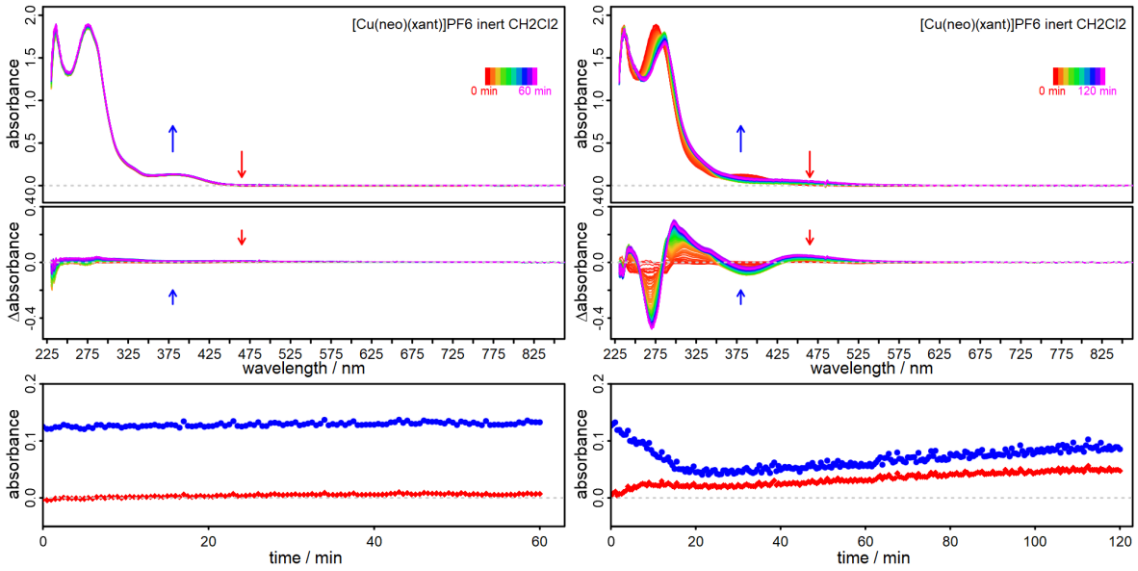

Figure S12.6. Photostability measurement of **Cuneo** without (left) and with irradiation (right). The spectra (top) are recorded for 1 h for the blank measurement and for 2 h with a 150 W Xe arc lamp. The difference spectra (middle) outline the difference in absorbance. The kinetics (bottom) present the decay at 380 nm (blue) and the increase at 465 nm (red). A photoproduct with a faint green fluorescence (488 nm) remains.

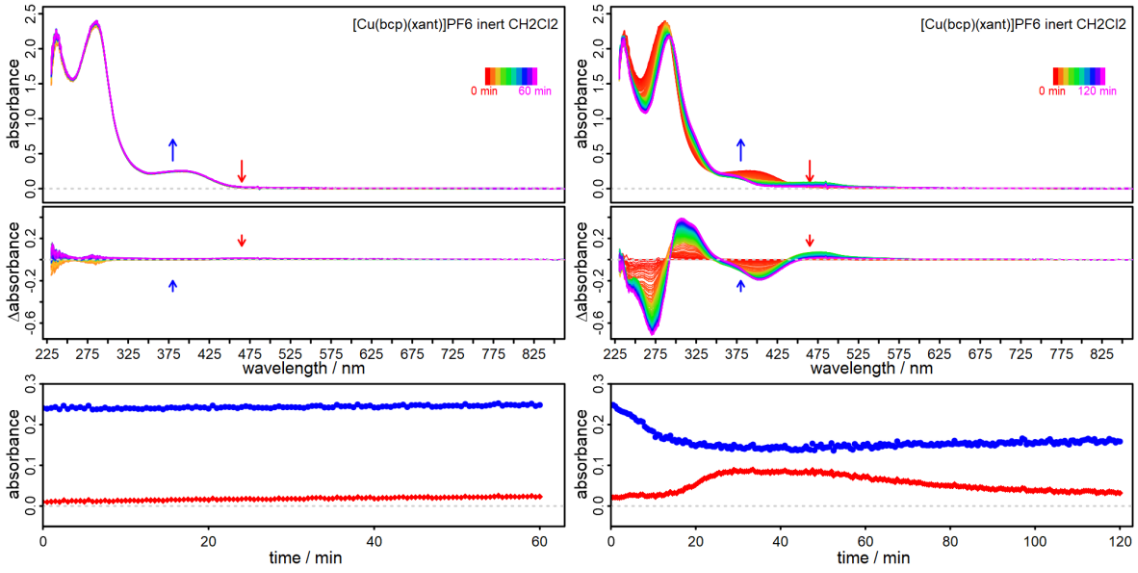

Figure S12.7. Photostability measurement of **Cubcp** without (left) and with irradiation (right). The spectra (top) are recorded for 1 h for the blank measurement and for 2 h with a 150 W Xe arc lamp. The difference spectra (middle) outline the difference in absorbance. The kinetics (bottom) present the decay at 380 nm (blue) and the increase at 465 nm (red). A photoproduct with a blue fluorescence (444 nm) remains.

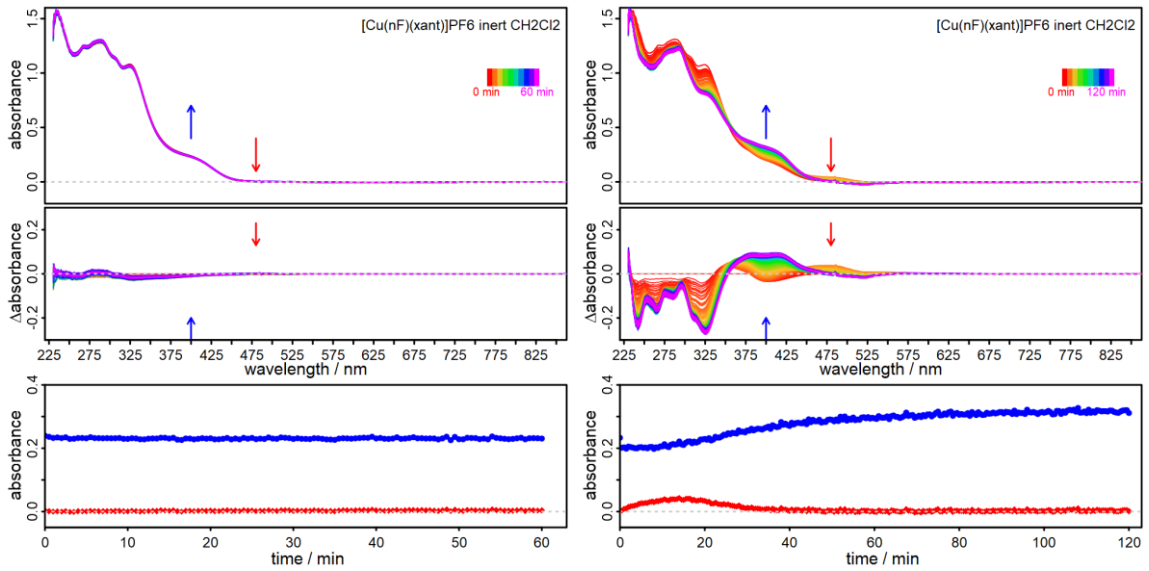

Figure S12.8. Photostability measurement of **CunF** without (left) and with irradiation (right). The spectra (top) are recorded for 1 hour for the blank measurement and for 2 h with a 150 W Xe arc lamp. The difference spectra (middle) outline the difference in absorbance. The kinetics (bottom) present the decay at 400 nm (blue) and the increase at 480 nm (red). A photoproduct with a green fluorescence (508 nm) remains.

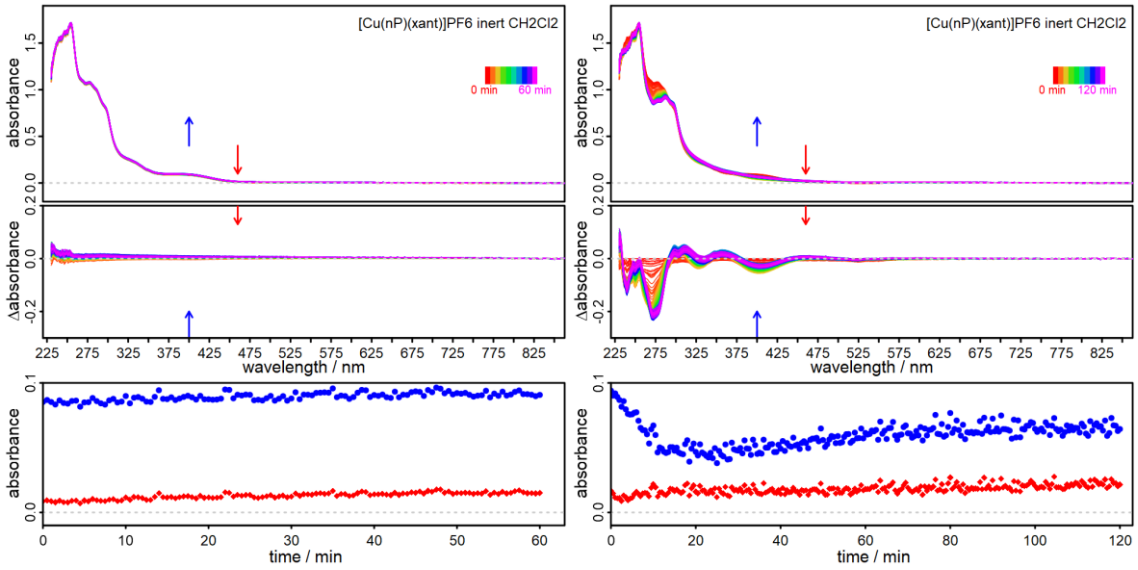

Figure S12.9. Photostability measurement of **CunP** without (left) and with irradiation (right). The spectra (top) are recorded for 1 h for the blank measurement and for 2 h with a 150 W Xe arc lamp. The difference spectra (middle) outline the difference in absorbance. The kinetics (bottom) present the decay at 400nm (blue) and the increase at 460 nm (red). A photoproduct with a green fluorescence (520nm) remains.

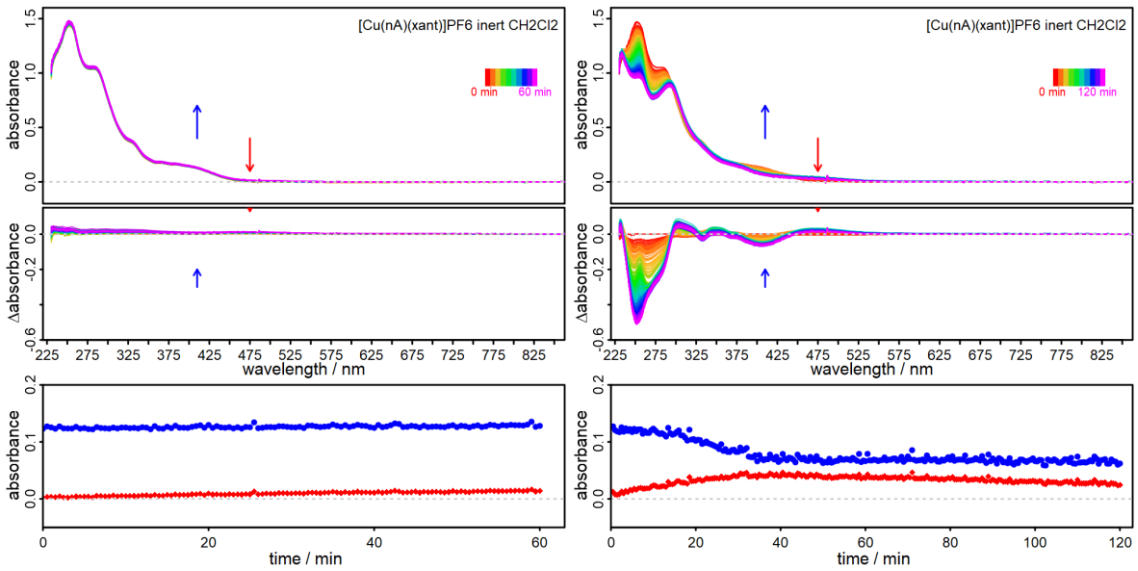

Figure S12.10. Photostability measurement of **CunA** without (left) and with irradiation (right). The spectra (top) are recorded for 1 h for the blank measurement and for 2 h with a 150 W Xe arc lamp. The difference spectra (middle) outline the difference in absorbance. The kinetics (bottom) present the decay at 410 nm (blue) and the increase at 475 nm (red). A photoproduct with a weak orange fluorescence (617 nm) remains.

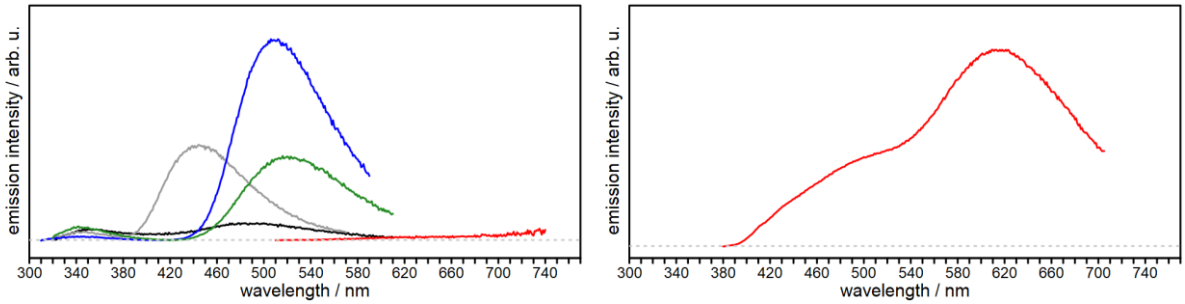

Figure S12.11. Emission spectra of the obtained photoproducts in unknown concentrations (left). The photoproducts emit at 488 nm (**Cuneo**, black), 444 nm (**Cubcp**, gray), 508 nm (**CunF**, blue), 520 nm (**CunP**, green) and 617 nm (**CunA**, red). Excitation and emission bandwidths were fixed at 1.2 nm each and excitation was carried out at 310 nm (**Cuneo, CunP**), 300 nm (**Cubcp**, **CunF**) and 250 nm (**CunA**). On the right, the spectrum of the **CunA** photoproduct was recorded with 3 nm bandwidths and excited at 365 nm.

13 Visualization

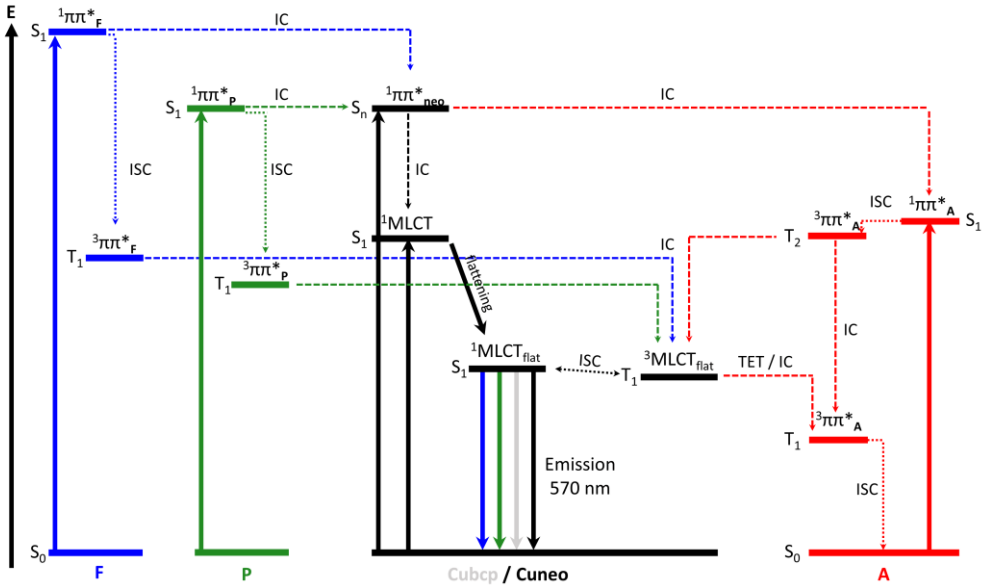

Figure S13.1: Proposed simplified energy level diagram of **Cuneo/Cubcp** (middle), with relevant singlet and triplet metal-to-ligand charge transfer states (^{1}MLCT & ^{3}MLCT). The singlet ^{1}ππ*$_{neo}$ is further added for understanding. On the lefthand side are one **F** and **P** substituent with their lowest singlet and triplet ππ* states. Energy levels of the relevant ππ* states of one **A** substituent are shown on the right. Solid arrows represent steady-state absorption and emission. Dashed and dotted arrows correspond to internal conversion (IC) and intersystem crossing (ISC). Decay pathways (colored dashed) are only drawn in for the lowest excited states to prevent clutter. Triplet energies were estimated from references 16.

14 References

1 D. Stalke, *Chem. Soc. Rev.*, 1998, **27**, 171-178.
2 CrysAlisPro, Rigaku Oxford Diffraction, Versions 1.171.42.69a and 1.171.43.100a 2022/2023.
3 a) G. M. Sheldrick, *Acta Crystallogr. A,* 2015, **71,** 3-8.
b) G. M. Sheldrick, Acta Cryst. 2008, A64, 112-122.
c) G. M. Sheldrick, *Acta Crystallogr. C,* 2015, **71,** 3-8.
4 a) O. V. Dolomanov, L. J. Bourhis, R. J. Gildea, J. A. K. Howard and H. Puschmann, *J. Appl. Crystallogr.,* 2009, **42,** 339-341.
b) A. L. Spek, *Acta Crystallogr. D.,* 2009, **65,** 148-155.
c) C. F. Macrae, I. Sovago, S. J. Cottrell, P. T. A. Galek, P. McCabe, E. Pidcock, M. Platings, G. P. Shields, J. S. Stevens, M. Towler and P. A. Wood, *J. Appl. Crystallogr.,* 2020, **53,** 226-235.
5 D. S. Karpovich and G. J. Blanchard, *J. Phys. Chem.,* 1995, **99,** 3951-3958.
6 P. A. Forero-Cortés, M. Marx, N. G. Moustakas, F. Brunner, C. E. Housecroft, E. C. Constable, H. Junge, M. Beller and J. Strunk, *Green Chem.,* 2020, **22,** 4541-4549.
7 a) F. Neese, *WIREs Comput. Mol. Sci.,* 2012, **2,** 73-78.
b) F. Neese, *WIREs Comput. Mol. Sci.,* 2018, **8,** e1327.
c) F. Neese, F. Wennmohs, U. Becker and C. Riplinger, *J. Chem. Phys.,* 2020, **152**, 224108.
d) F. Neese, *WIREs Comput. Mol. Sci.,* 2022, **12,** e1606.
8 a) C. Adamo and V. Barone, *J. Chem. Phys.,* 1999, **110,** 6158-6170.
b) M. Ernzerhof and G. E. Scuseria, *J. Chem. Phys.,* 1999, **110,** 5029-5036.
c) F. Weigend and R. Ahlrichs, *Phys. Chem. Chem. Phys.,* 2005, **7,** 3297-3305.
d) S. Grimme, J. Antony, S. Ehrlich and H. Krieg, *J. Chem. Phys.*, 2010, **132**, 154104.
e) S. Grimme, S. Ehrlich and L. Goerigk, *J. Comput. Chem.,* 2011, **32,** 1456-1465.
9 a) F. Neese, *J. Comput. Chem.,* 2003, **24,** 1740-1747.
b) F. Neese, F. Wennmohs, A. Hansen and U. Becker, *Chem. Phys.,* 2009, **356,** 98-109.
c) R. Izsák and F. Neese, *J. Chem. Phys.,* 2011, **135**, 144105.
10 M. Garcia-Ratés and F. Neese, *J. Comput. Chem.,* 2020, **41,** 922-939.
11 a) F. Neese and G. Olbrich, *Chem. Phys. Lett.,* 2002, **362,** 170-178.
b) T. Petrenko, S. Kossmann and F. Neese, *J. Chem. Phys.,* 2011, **134**, 054116.
12 a) M.-H. Baik and R. A. Friesner, *J. Phys. Chem. A*, 2002, **106**, 7407-7412.
b) L. E. Roy, E. Jakubikova, M. G. Guthrie and E. R. Batista, *J. Phys. Chem. A,* 2009, **113,** 6745-6750.
c) D. Wang, S. Huang, C. Wang, Y. Yue and Q. Zhang, *Org. Electron.,* 2019, **64,** 216-222.
13 a) T. D. Goddard, C. C. Huang, E. C. Meng, E. F. Pettersen, G. S. Couch, J. H. Morris and T. E. Ferrin, *Protein Sci.,* 2018, **27,** 14-25.
b) E. F. Pettersen, T. D. Goddard, C. C. Huang, E. C. Meng, G. S. Couch, T. I. Croll, J. H. Morris and T. E. Ferrin, *Protein Sci.,* 2021, **30,** 70-82.
c) E. C. Meng, T. D. Goddard, E. F. Pettersen, G. S. Couch, Z. J. Pearson, J. H. Morris and T. E. Ferrin, *Protein Sci.,* 2023, **32,** e4792.
14 a) A. J. Schaefer, V. M. Ingman and S. E. Wheeler, *J. Comput. Chem.,* 2021, **42,** 1750-1754.
b) V. M. Ingman, A. J. Schaefer, L. R. Andreola and S. E. Wheeler, *WIREs Comput. Mol. Sci.,* 2021, **11,** e1510.
15 P. van der Sluis and A. L. Spek, *Acta Crystallogr. A,* 1990, **46,** 194-201.
16 a) McClure1949 D. S. McClure, *J. Chem. Phys.,* 1949, **17,** 905-913.
b) Langelaar1971 J. Langelaar, R. P. H. Rettschnick and G. J. Hoijtink, *J. Chem. Phys.,* 1971, **54,** 1-7.
c) Scypinski1984 S. Scypinski and L. J. C. Love, *Anal. Chem.,* 1984, **56,** 322-327.
d) Carmichael1986 I. Carmichael and G. L. Hug, *J. Phys. Chem. Ref. Data,* 1986, **15,** 1-250.